

# Estimation of the Vibration Decrement of an Offshore Wind Turbine Support Structure Caused by its Interaction with Soil

July 15<sup>th</sup>, 2011

Willem Geert Versteijlen

MSc thesis



# Estimation of the Vibration Decrement of an Offshore Wind Turbine Support Structure Caused by its Interaction with Soil

Master of Science Thesis

**Author:** Willem Geert Versteijlen

**Committee:** Prof. Dr. A.V. Metrikine TU Delft - Chairman  
Ir. J.S. Hoving TU Delft  
Ir. G. Tol TU Delft  
Ir. W.E. de Vries TU Delft  
Ir. E. Smid Siemens Wind Power  
Ir. S.N. Voormeeren Siemens Wind Power

July 15<sup>th</sup>, 2011

---

*Compared with the other components of the total damping, the characterization and modelling of soils damping is more complex and less well established.  
...the soils damping estimate is the least certain.*

M.F. Cook - 1982

Shift Happens..

# Summary

In today's cutting costs environment in the offshore wind industry, significant achievements can be made with a better assessment of dynamic soil-pile interaction. More knowledge regarding the contribution of the dynamic soil-pile interaction to damping of an offshore wind turbine structure (OWT) could perceptibly reduce the fabrication costs of an OWT.

Currently, not much is known about the contribution of soil to the total damping of the vibration of an OWT which consists of five main damping mechanisms: aerodynamic-, hydrodynamic-, structural-, soil- and a passive sloshing damper in the nacelle.

The values for this contribution applied in the industry today - mostly calculated analogously to a study performed in 1980 by M.F. Cook - can be expected to be on the low side (conservative), and it is acknowledged that it might be higher. More research on the topic is recommended.

Increased damping of the vibrations of an OWT decreases the occurring stresses in the structure which in turn results in lower (often design driving) fatigue damage accumulation. Presence of more damping than currently assumed would justify either designing more light-weight structures using less construction steel, or allowing for longer (insured) OWT lifetimes than the currently applied 20 years. Both measures significantly reduce costs of offshore generated wind power.

This research evaluates measured signals of twelve 'rotor stop' - tests on an offshore wind turbine at the Dong Energy owned - Burbo Bank wind farm in the Irish Sea. The recorded data comprises the vibration decay of the structure, measured with an accelerometer and strain gauges along the tower.

An analytical model has been developed enabling analyses of the origin of the measured signals.

Two main frequencies were identified in the measurements and, using the different measurement locations and the model, the corresponding modal shapes were identified.

A crucial distinction between the two modal shapes is the difference in motion of the lower part of the structure. The amplitudes of displacement and velocity at this location are much smaller for the second observed modal shape than for the first.

A large difference in damping ratio between the two frequencies was identified.

The difference in damping is attributed to the different effect the soil can have on the damping of these two frequencies. This can be explained by the varying amplitudes of their modes in the soil embedded part of the structure.

The measured total damping (19 % logarithmic decrement which is 3 % ratio of critical) for the first natural bending frequency of the tower, and the possible order of magnitude of the found contribution of soil on this damping ( $\sim 9.5$  % log. decr. or 1.5 % ratio) of this particular OWT is significantly larger than the order of magnitude used in the industry today (respectively  $\sim 2.5$  % log. decr. and  $\sim 0.44$  %).

# Acknowledgement

I owe many people thanks for helping me to, amongst others, deliver this booklet and its content.

First of all I want to thank my professor, Andrei Metrikine. After having been totally intimidated by the content of his lectures, he did somehow become my professor. All his patience, the amount of his time he gave me, the endured disappointments, and the level he finally made me reach are admirable.

I owe thanks also to the rest of my 'TU-committee'; Jeroen Hoving for his knowledge and battle-experience with computational software, Wybren de Vries for his thorough corrections of and feedback on my written work and his constructive thesis-progress advice, and finally Gerrit Tol, for his support in different ways throughout the MSc years.

Doing my thesis at the Offshore Center of Competence of Siemens Wind in The Hague was not only the condition for being able to do the type of thesis I did, the atmosphere in this office really gave all those months a very pleasant extra tinge.

At Siemens I firstly want to thank David-Pieter Molenaar for first of all accepting me and delivering me a challenging subject for which I got all the freedom and resources to finally master it. The time he takes to stay up to date and give you in-depth advice, challenging you to involve other people of the department in your focus area, hereby pushing yourself forward in different ways, *while* managing the entire CoC, is inspiring.

I want to thank Erik Smid who, also besides his demanding load-engineering job, guided me, gave feedback on deliverables and made the offshore experiments possible. Sven Voormeeren and Paul van der Valk were my 'dynamic'

admiration guys at Siemens who more than once turned out to have some useful tricks and insights in the mysterious world of structural dynamics.

Overall I want to thank all of these people for the fun times, coffee's, beers and diners we had, and in that respect I musn't forget to mention Philip, Rad, Chris, Jan-Bart, Piet, Niels en Maxim.

The permittal and hospitality of DONG Energy for letting us perform rotor stops on their 'BB16' turbine, was of course also a clear condition for the success of this thesis.

Well, Mom and Dad, it sure looks like I'll start being somewhat more independent soon...I'll miss it, thanks so far.

Thank you all!

Pim Versteijlen

*June 2011*

# Nomenclature

## Abbreviations

API	American Petroleum Institute
Au	Text included by the author (used when quoting)
BB	Burbo Bank wind farm
BB16	Test turbine for this research in Burbo Bank wind farm
BC	Boundary Condition
DFT	Discrete Fourier Transform
EOM	Equation of Motion
FFT	Fast Fourier Transform
FR	Frequency Response
IEA	International Energy Association
IC	Interface Condition
log. decr.	Logarithmic Decrement
MP	monopile
NIMBY	Not In My Backyard
OWT	Offshore Wind Turbine support structure
Q-factor	Quality-factor
RNA	Rotor Nacelle Assembly
SDOF	Single Degree Of Freedom
SPI	Soil-Pile Interaction
SSI	Soil-Structure Interaction
TP	Transition Piece

# Contents

<b>Abstract</b>	<b>i</b>
<b>Acknowledgement</b>	<b>iii</b>
<b>Nomenclature</b>	<b>v</b>
<b>Contents</b>	<b>v</b>
<b>1 Introduction</b>	<b>1</b>
1.1 The Offshore wind industry . . . . .	1
1.1.1 Sustainable Consensus . . . . .	1
1.1.2 Renewable Energy Sources . . . . .	2
1.1.3 Wind Power . . . . .	3
1.1.4 Offshore Wind Power . . . . .	4
1.2 Research & Development in Offshore Wind Power . . . . .	6
1.2.1 Cutting Life Cycle Costs . . . . .	6
1.2.2 Siemens Wind . . . . .	7
1.2.3 Motivation for this Research . . . . .	10
1.3 Thesis Objective, Scope & Approach . . . . .	12
1.3.1 Objective . . . . .	12
1.3.2 Scope & Approach . . . . .	12
1.4 Thesis Outline . . . . .	13
<b>2 Literature on Damping in Soil-Pile Interaction &amp; State of the Art in the Offshore Wind Industry</b>	<b>15</b>
2.1 Types of Damping . . . . .	15
2.2 Measuring Damping . . . . .	20
2.3 Developed models for Soil-Pile interaction . . . . .	26
2.4 Current Design Practice and Damping Determination in the Offshore Wind Industry . . . . .	33

2.5	Summary & Discussion . . . . .	35
<b>3</b>	<b>Offshore Measurements</b>	<b>36</b>
3.1	Performed Experiment . . . . .	36
3.2	Obtained Data . . . . .	40
3.3	Data Analyses . . . . .	43
3.3.1	Power Spectra . . . . .	43
3.3.2	Damping Assessment . . . . .	46
3.4	Patterns in Signal Output . . . . .	55
3.5	Summary & Discussion . . . . .	57
3.5.1	Summary . . . . .	57
3.5.2	Discussion . . . . .	58
<b>4</b>	<b>Modeling the Support Structure</b>	<b>62</b>
4.1	Constrained Beam Model . . . . .	63
4.1.1	Aspects of the Model . . . . .	65
4.1.2	The Governing Equations . . . . .	67
4.1.3	Solving the Problem in the Frequency domain . . . . .	71
4.2	Model Implementation . . . . .	77
4.2.1	Model Variables . . . . .	77
4.2.2	Software . . . . .	82
4.3	Model Results . . . . .	82
4.3.1	Frequency Equation . . . . .	82
4.3.2	Modal Shapes . . . . .	84
4.3.3	Power Spectra . . . . .	88
4.3.4	Timedomain comparison . . . . .	91
4.4	Summary & Discussion . . . . .	93
4.4.1	Summary . . . . .	93
4.4.2	Discussion . . . . .	94
<b>5</b>	<b>Conclusions and Recommendations</b>	<b>96</b>
5.1	Conclusions . . . . .	96
5.2	Recommendations . . . . .	98
	<b>Appendices</b>	<b>101</b>
<b>A</b>	<b>An Introduction to Damping in System Dynamics</b>	<b>102</b>

<b>B</b>	<b>Measuring Soil Damping</b>	<b>108</b>
B.1	In situ measurements . . . . .	109
B.2	Laboratory experiments . . . . .	111
<b>C</b>	<b>BB16 Rotor Stop Measurement Specification Documents</b>	<b>113</b>
C.1	Overview Morning Tests . . . . .	114
C.2	Location and Orientation of Strain Gauges BB16 . . . . .	115
C.3	Soil Profile at BB16 OWT . . . . .	119
<b>D</b>	<b>The Fourier Transform and Signal Processing Basics</b>	<b>122</b>
<b>E</b>	<b>Damping Assessment Results</b>	<b>129</b>
<b>F</b>	<b>Test Opportunities and Roadmap</b>	<b>135</b>
<b>G</b>	<b>Pinned Beam Model</b>	<b>143</b>
<b>H</b>	<b>Applied Values for Model Parameters</b>	<b>157</b>
<b>I</b>	<b>Finding the sign of terms in the Equation of Motion</b>	<b>160</b>

# 1

## Introduction

*This first chapter starts with a description of the background of this thesis; the offshore wind industry. The incentive for this research is given in the second section, and a formulation of the objective, the scope and approach are described in the third section. The chapter is finalized with an outline of the structure of this report.*

### **1.1 The Offshore wind industry**

The offshore wind industry is the background of this research. This section describes this setting.

#### **1.1.1 Sustainable Consensus**

It has become a well known topic; we are running out of easily accessible fossil fuels, accelerated global warming probably has something to do with our increased  $CO_2$  emission, while at the same time energy demand grows exponentially because of increased population and economic wealth. Sustainability - in all its forms - is the word on the streets.

As popular as this motto might be, its relevance is quite eminent. Mankind has now acquired the technology and moral awareness that can let him attain his needs in a more responsible and challenging way, in the mean time maybe benefiting the environment while doing so.

Fortunately world wide politics and policy are reaching consensus on stimulating sustainable developments. The EU's '20-20-20'-initiative is an example of such a policy. By the year 2020, EU-countries want to reduce  $CO_2$  emission with 20% (taking the year 1990 as reference), reduce energy consumption with 20% and 20% of all the energy has to originate from renewable sources. Each member-state has its own way of reaching this goal, but overall this aim significantly stimulates the development of renewable energy industries [12].

### 1.1.2 Renewable Energy Sources

In the pursuit towards inexhaustible<sup>1</sup> energy supply for society, various paths lead to victory. Solar-, nuclear- (both fission and fusion), wind-energy, bio fuels and hydropower are some of the realistic ones.

Nuclear fusion is a very promising form of energy generation, but expected to become economically interesting after 2050. Hydropower is clean and efficient but besides geographic requirements and impacts, its growth potential is limited to three times the current globally installed power. Large scale production of bio-fuels needs vast surface areas competing with agricultural land usage. These are some of the reasons that governments tend to focus on nuclear- (fission, with its danger and waste disadvantage taken for granted), solar and wind power. These last two are seen as very promising on the relatively short term [1]. Figure 1.1 depicts a scenario of future global usage of energy sources, developed by the International Energy Agency (IEA) [21]. The IEA included a prospective called the '450-scenario' which will mitigate the effects of climate change due to greenhouse gas concentrations in the atmosphere; no more than 450 greenhouse gas parts per million in the atmosphere. In this scenario, the use of carbon-rich energy sources is limited.

---

<sup>1</sup>Inexhaustibility in this context is disputable - each renewable source needs their own materials and chemicals, which are in turn exhaustible. But the distinction of these sources with respect to most conventional sources, or rather techniques, is that they do not convert scarce carbon-rich fossil fuels into energy. It has to be mentioned that also the scarcity of these fossil fuels is subject to discussion.

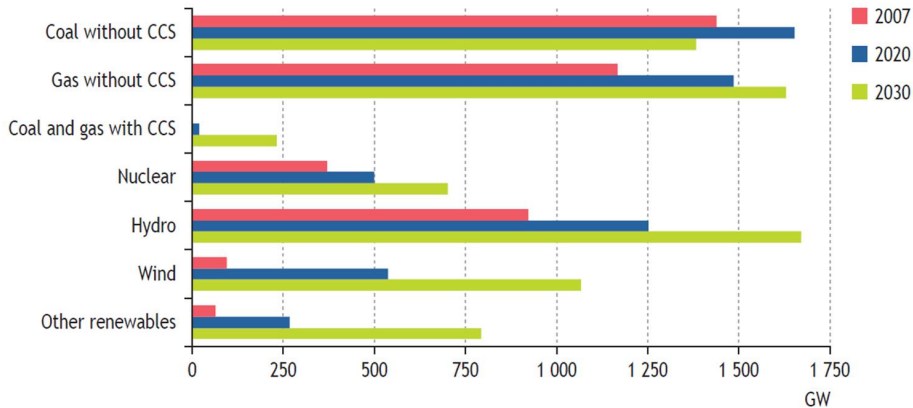


**Figure 1.1:** Current and future sources of global energy use according to the '450-scenario': 450 greenhouse gas parts per million in the atmosphere. CCS= $CO_2$  Capture & Storage. Source: International Energy Agency (IEA) - [21].

### 1.1.3 Wind Power

Energy capture from wind is an old proven art. The Persians introduced the first documented windmills in the tenth century A.D. Today global wind power comprises around 198 GW and an energy delivery<sup>2</sup> of 435 TWh in the year 2010.

To put this number in perspective; a proper coal-powered power plant has on average power of 1000 MW (1 GW) and a Boeing 747 powers up to 250 MW during take off. In 2008 the world was consuming energy at a rate of 15 TW (15000 GW) of which about 2.2 TW was electric power.

Figure 1.2 gives figures for different scenarios of future wind power developments. The Reference scenario is developed by the International Energy Agency (IEA) based on current policies. But including the latest developments, this scenario has already been proven to be too conservative with respect to the expected wind power growth.

<sup>2</sup>Attention should be paid to the fact that talking about a power capacity (in Watts=energy/time [J/sec]) has a limited information yield. This is the power a powerplant *could* produce. The actual energy that *is* produced or consumed is usually expressed in KWh; a thousand Joules times 60 minutes times 60 seconds (one hour).

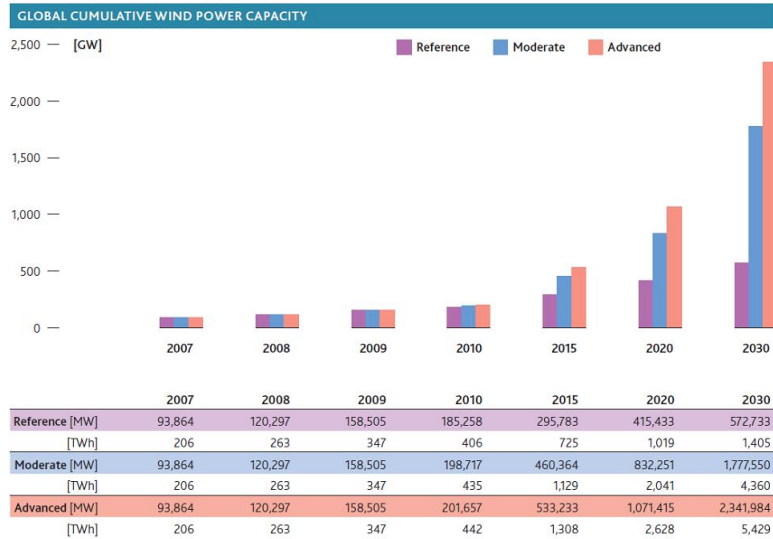


**Figure 1.2:** Projection of globally installed wind power. Source: Global Wind Energy Council (GWEC) - [7].

An extensive number of locations and amount of surface area is available for more wind turbines, especially in remote windy areas such as deserts. In more crowded regions available space is running out, and despite of being absolutely in favor of 'green' energy, most people will raise their NIMBY (Not In My BackYard) billboard when threatened to experience close encounters with these green giants.

Where to go? To sea! Besides space, this environment is characterised by stronger and more frequent winds.

#### 1.1.4 Offshore Wind Power

Europe is pioneer and leader in offshore wind farm development, and lately enthusiastically followed by China. By July 2010 Europe's offshore wind power capacity mounted up to 2396 MW with a total of 948 turbines in 43 wind farms. Denmark's Vindeby wind farm was the World's first offshore wind farm to be

built in 1991. Needless to state the fresh pioneering atmosphere in this industry; new technology is constantly being developed and new ideas are quickly implemented. Political ambitions on this front are strong; by the year 2020, 12-14% of Europe's electricity has to be generated by wind, and 25-29% of this will be generated offshore, which comes down to 3-4% of Europe's total electricity generation [13]. For the Netherlands this was translated to 6000 MW of offshore installed power. With currently 228 MW installed, the Dutch have given themselves a fair challenge.

To give some more feel of the current relative capacity of offshore wind power in the Netherlands: over the years 2008, 2009 and 2010, the two offshore wind farms in the Netherlands (Prinses Amalia and Egmond aan Zee) have produced an average of 670 GWh per year. As a ballpark figure, it is said that an average household uses 3500 kWh per year. So the two Dutch offshore farms have generated electricity for about 191.000 households each year. The potential of offshore wind energy in the Dutch North Sea is estimated to be able to provide twice the required electricity in the Netherlands [4].

Costs for offshore wind generated electricity in Europe currently (December 2010) runs about 6-8 € cents/kWh compared to 5.3-6.1 €/kWh for onshore wind. Most European countries still have a subsidy system guaranteeing a fixed buying price to the wind-generated electricity. In the Netherlands this so called 'feed-in' tariff is 11.8 for onshore and 18.6 €/kWh for offshore wind. Domestic consumers pay 24.1 € c/kWh for their electricity [20]. Installing wind energy onshore currently costs around 1.23 million €/MW and 2.1 million €/MW offshore. As every new industry, governmental stimulation results in rapid technological development and decreasing costs because of industry investments and research studies. Expectations for future wind energy prices and competitiveness with conventional sources are rosy.

Figure 1.3 depicts a cost-comparison histogram, comparing the cost of energy of wind power with that of conventional fossil sources. The extra costs of carbon-capture for the conventional sources are depicted with purple (extra) bars.

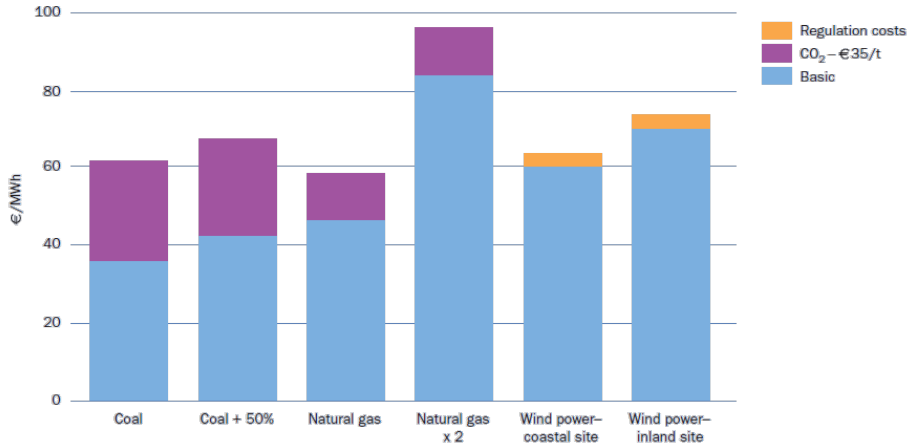


**Figure 1.3:** Comparison of total life cycle energy costs with increasing coal and gas prices included. A European inland and coastal onshore case is taken as reference. Offshore generated electricity also runs between 60 to 80 €/MWh depending mainly on depth, distance to shore and investment costs. Regulation costs are the costs of integrating the variable wind energy into the grid. Source: European Wind Energy Association (EWEA) - [13].

## 1.2 Research & Development in Offshore Wind Power

The main motivation for most research in the offshore wind industry is to reduce the overall costs. The young character of this industry allows for many opportunities to do so. This section is devoted to briefly describe these developments, and to report the motivation for the research presented in this thesis.

### 1.2.1 Cutting Life Cycle Costs

Wind power can become as cheap as electricity generated from coal, but in order to do so, some major costs have to be reduced. Fortunately there are enough components in the life cycle of an offshore wind turbine structure (OWT) where

money can be saved. Most costs are made during construction and maintenance during the lifetime of the OWT.

To decrease maintenance costs, the industry is looking into the development of turbines with significantly less components. ‘Direct Drive’ turbines are an example of this; lacking a gearbox, these turbines have up to 50% less parts than conventional turbines.

Another maintenance cost driver is the limited accessibility of OWTs. The conventional way of accessing an OWT is by use of a vessel. Such a way of accessing requires calm sea states, and this requirement seriously narrows the time-window of possible access in rough seas like the North Sea. Long turbine down-times are the result. Increasing the accessibility of the OWTs by access systems that can still be used in rougher seas is another way of decreasing service costs.

In the construction phase, there is room for applying less construction steel. The foundation of the tower and nacelle mounts up to about 20% of the total capital costs [32]. During the 20-year lifetime of the structure, the on average 80m long tower and nowadays 120m rotor diameter are constantly exposed to wind and wave forces. All these forces have to be transferred to the ground by the foundation. Various foundation solutions exist, but the most popular one for shallow water (up to 30m deep) is the monopile (MP). A MP is a long tubular cylinder with typical dimensions of 45m length, 5m diameter and 60mm wall thickness. An impression of the cross-section of such a MP is given in figure 1.4.

### **1.2.2 Siemens Wind**

Siemens is a considerable participant in this growing industry. In 2004 Siemens bought the Danish wind turbine manufacturer Bonus Energy. Now Siemens has a 6000 employee-strong wind department with its head office in Brande, Denmark. Siemens designs and constructs the complete turbine and tower. In its attempt to improve its product and to cut costs, Siemens has a sizeable R&D department providing also MSc and PhD students the opportunity to dedicate their thesis on various of these improvement-focused subjects. The next paragraph gives a brief description of some topics that have been studied by students at the Siemens offshore Center of Competence in The Hague.



**Figure 1.4:** The author standing inside a monopile which is ready to be shipped out and installed at Sheringham Shoal wind farm. The cross section of this particular monopile has a diameter of 5.5m and a wall thickness of 6.5cm.

A promising production cost reducing area, is construction steel mass-reduction by integral and optimized design ([15] & [17]).

Loads-reduction on the entire structure can be achieved by System Identification (SI). SI is a tool for better control design, that can reduce loads on the structure. SI can yield more accurate dynamic (sub-)models that allow for enhanced model-based System Control. Examples of control variables are for instance the blade pitch angle and the generator speed. By for example varying the pitch angle with accordance to the wind speed, loads on the blades and thus overall loads on the structure can be reduced. ([29] , [31] , [2] and [34]).

Another research field is that of Dynamic Substructuring. As opposed to global dynamic approaches, in these studies the local dynamics of components is considered. Global dynamic analyses can lead to underestimation of the loads on

a local scale. In these approaches, Model Reduction techniques are studied and incorporated in order to reduce the computation time needed to model and integrate all sub-systems ([38], [36] and [8]).

Besides studies on more efficient maintenance [35] and production & installation [24] strategies, lately a focus is also laid upon the soil-pile interaction (SPI) phenomena that occur at the embedded monopile foundations. A MSc thesis has been dedicated on the static initial stiffness of soil, where a critical assessment was made on the currently used p-y curves of the American Petroleum Institute (API), which are extrapolated onto the large diameter piles of the MP foundations of OWTs. Underestimating the initial stiffness can lead to too conservative designs dictating too large dimensions for the piles. [39]

Where this latest study focused on the stiffness of soil, this thesis focuses on another dynamic property of soil; the damping effect caused by soil in the soil-pile interaction process.



**Figure 1.5:** The construction of an offshore wind farm; the towers are placed on top of the transition pieces, they are connected at the platform at interface level.

### 1.2.3 Motivation for this Research

Offshore wind turbine support structures are currently designed to survive at least twenty years of environmental 'assaults'. In most cases, the fatigue lifetime of the structures is design driving. Steel fatigue damage is determined by the number of cycles at a particular stress range during the lifetime of the structure. These stress ranges are caused by the wind and waves hitting the structure, causing overturning moments and oscillating back- and forth movement of the tower. The structure loses this dynamic energy via 5 different *damping* mechanisms. These are from top to bottom of the structure:

- Aerodynamic damping of the rotor and tower moving through the air
- A calibrated sloshing damper in the nacelle, a passive counter-moving mass.
- Structural damping; heat generation because of stress cycles in the construction materials
- Hydrodynamic damping of the foundation moving in the water
- Damping caused by the interaction of the soil and the foundation

The aerodynamic damping of the turning rotor during production is one of the largest of these influences. The blades turn fast enough to behave as if a large disc (120m diameter) is moved forth and aft through the air (wind). This generates large damping forces. A similar example of this which might be easier to imagine, is the force you feel when you move your flat hand (rotor disk) through the water. This force might be smaller if you spread your fingers (rotor disc standing still) and perform the same movement.

The installation of the sloshing damper in the nacelle is a more recent development, which has not always been applied in the past. A sloshing damper is a tuned counter moving mass, in this case a large bucket with water. Tuned mass dampers (in the form of large moveable steel spheres) are also often placed in the top of high-rise buildings to counter-act the displacements at that location.

The more damping the structure is subjected to, the smaller the amplitudes of the oscillations, thus the lower the fatigue damage accumulation. In the design and modeling of offshore wind turbines, the magnitude of these five mechanisms of damping is an important influential factor to determine the dimensions of the structure.

Of these mechanisms, least is known about the magnitude of the effect that soil has on the damping of the OWT.

The offshore wind industry mostly refers to a paper of M.F. Cook from 1982 [37] who performed measurements on a single pile platform with a pile diameter of 1.22m. Chapter 2 elaborates on Cook's paper and explains dynamic damping in more detail.

The assessment of the magnitude of the damping influence of the soil that is presently performed analogously to Cook's paper, yields conservative values; a low percentage for soil damping<sup>3</sup> is incorporated in the design. Both Cook and the designers acknowledge that the real soil damping ratio is probably higher, but scientific proof of this is still absent. "The characterization of soils damping is more complex - *than the other damping mechanisms* [Au] - and less well established....This technique - *Cook's technique to determine soil damping* [Au] - is approximate and research leading to the development of new techniques is warranted."

To shortly summarize the above: higher proven damping ratios justify more slender designs or longer lifetimes of OWTs because of lower fatigue damage accumulation, resulting in cost reduction because of steel savings or longer lifetimes of the OWTs. There is a belief in the industry that a large gain in proven damping can be found due to effect of the soil.

---

<sup>3</sup>Strictly speaking, one should use the term of 'the effect of soil on the vibration decrement of an oscillating pile' instead of soil damping. Soil damping actually refers to energy dissipation within a specific soil specimen, and not what is meant in this context; the damping in soil-pile interaction. For reasons of simplicity, the term 'soil damping' will be used to indicate this phenomenon in this thesis.

## 1.3 Thesis Objective, Scope & Approach

### 1.3.1 Objective

The scientific basis of this research is the data collected from an offshore ‘rotor stop’ experiment. During these tests the decaying for-aft movement of the nacelle was measured. Naturally, the results found for this test only apply to the specific soil conditions at the location of the used turbine. The vibrations of the structure itself were measured via strain gauges and an accelerometer. The soil’s reaction was not measured. This is further explained in chapter 3. Because of these reasons, this thesis is focused on stating the magnitude of soil damping which the considered test turbine receives of the complete soil profile at its location. The objective (like the title of this thesis) is stated as

*The estimation of the vibration decrement of an offshore wind turbine support structure, caused by its interaction with soil.*

This research is a first phase of a larger damping assessment project. A respectable ultimate objective for this damping assessment project that Siemens has initiated would be

*The ability to predict the amount of damping experienced by an offshore wind turbine-supporting structure due to interaction with a certain type of soil present at a certain location.*

To reach such an objective, extensive in situ experiments have to be performed. Appendix F elaborates on the setup of such experiments, and reports on the used selection procedure for choosing the proper experiment for this thesis. In this appendix, also a roadmap is suggested towards reaching the stated ultimate objective.

### 1.3.2 Scope & Approach

As stated in the previous paragraph, time signals of in total twelve rotor stops will be evaluated. These time series are recorded with strain gauges at different

vertical levels on the tower, and with an accelerometer in the nacelle.

Different techniques exist to distill information from measured time series. In this thesis most analyses of the measured response of the turbine will be performed in the frequency domain. The collected time signals are hence Fourier-transformed to the frequency domain. Applying the Fourier transform on a time signal, renders the occurring frequencies with their energy. Performing this analysis on strain gauges at different heights can show the difference in energy-level of certain frequencies between these locations, yielding (some) information about the corresponding modal shapes of these frequencies. This will be further explained in chapter 3.

The total damping (composed of the five damping mechanisms named in §1.2.3) on the occurring frequencies in the measurements will be determined using the Quality factor technique in the frequency domain.

A simplistic analytical model is developed to be able to analyze the measured responses and possibly reveal the occurring phenomena that cause these responses.

With both the measurements and the model, it is investigated if an opportunity exists to assess the contribution of soil to the total damping of the structure. If it is found to be possible, this effect will be quantified.

## 1.4 Thesis Outline

This report has roughly the same structure as the approach, which is as follows:

This **Introduction** chapter serves to make the reader, possibly a layman, acquainted with some facets of the offshore wind industry, in order to explain the motivation of this research. It also states what will be studied, and thus implicitly, equally important, what not. Finally, the structure of this report is given, which is in line with the approach.

The second chapter, **Literature on Damping in Soil-Pile Interaction & State of the Art in the Offshore Wind Industry**, relates a part of the literature study that was performed prior to performing the experiments. This chapter describes different types of damping, it reports the damping identification technique used

in this research and it names some other techniques for measuring damping. The third section describes two models for soil-pile interaction from literature, followed by a section on the currently applied practice in the offshore wind industry for estimating the amount of soil damping. Each chapter is closed with a section giving a summary and discussion. Appendices A, ?? and B serve as supporting material to this chapter

In the succeeding chapter, **Offshore Measurements**, the performed experiment, the acquired data and analyses of this data are reported. Damping values and motion patterns in the structure are listed in sections 3.3 and 3.4. Background information on matters discussed in this chapter are given in appendices D and F.

In the fourth chapter, **Modeling the Support Structure**, the next step in the analyses of the measurements is performed: a simplistic analytical Euler-Bernoulli beam model is developed, serving better insight in the physics behind the measured phenomena. The aspects and parameters are reported and the results of the simulation of the measured response are depicted in the third section.

Chapter **Conclusions & Recommendations** closes this report. Here the main found trends and results are connected with the possible physical phenomena causing these responses. Conclusions are drawn on the opportunity to determine the effect of soil on the vibration decrement of the measured structure , and a possible magnitude of this effect is stated. The report ends with recommendations for further research on this topic.

# 2

## Literature on Damping in Soil-Pile Interaction & State of the Art in the Offshore Wind Industry

*This chapter starts with a brief description of the main types of damping in structural dynamics and how these occur in the soil-pile interaction (SPI) of a monopile support structure of an offshore wind turbine. In the second section different damping measurement techniques are discussed. The third section elaborates on damping in dynamic soil-pile interaction as described in literature. The last section gives a rendition of the way the amount of soil damping is assessed in the offshore wind industry today. Appendices A and B serve as supporting material to the topics of this chapter.*

### **2.1 Types of Damping**

The field of structural dynamics studies the oscillatory behavior of structures (buildings, but also cars, aeroplanes etc.) subjected to dynamic loading. Dynamic in the sense of change of magnitude and direction in time. Some first

basic terms of structural dynamics are explained in appendix A.

In this context, *damping* is the dissipation of energy from the system (structure) to its environment. There are numerous ways in which a system can lose its (vibrational) energy to its surroundings. The main damping *mechanisms* present in the soil-pile interaction of OWT's are explained in the next paragraphs.

### **Viscous damping**

The magnitude of a viscous damping force is proportional to velocity. It is generally symbolized with a dashpot in dynamic model depictions. As it is velocity dependent, it is also dependent on the combination of amplitude and frequency.

A well-known viscous damper is the shock-absorber within the spring attached to each wheel in a car-suspension, as shown in figure 2.1. This damper absorbs shock energy every time the wheel hits a bump in the road, and causes the vertical vibrations of the car to decrease in time.

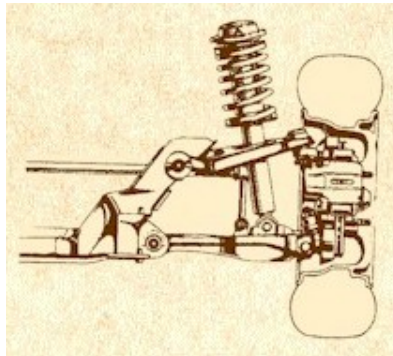


**Figure 2.1:** The suspension of a car; a viscous dashpot is installed within the spring to absorb the shock-energy. This parallel combination of a spring and dashpot is called a Kelvin-Voigt configuration.

### Viscous damping in SPI of an OWT

The water trapped in the saturated granular soil structure in which a monopile of an OWT is imbedded, could cause viscous damping forces on the monopile when excited at a certain speed (and forced to flow within the granular structure) by the oscillatory motion of the monopile. So viscous damping could very well play a role in the soil-pile interaction of an OWT.

### **Hysteretic damping**

A type of damping which is not frequency dependent, is called hysteretic or material damping. Hysteretic (or intrinsic) damping is the dissipation of energy caused by friction of the system with its surroundings. Hysteretic damping is in phase with the velocity and proportional to the displacement of the system.

The stress-strain curve of an hysteretic material during unloading is not the same as the one during loading. This is called a *hysteresis loop*. The area enclosed by the two curves (loading and unloading) is equal to the amount of energy lost during one loading cycle. Figure 2.2 gives an impression of such a loop and the area between the curves.

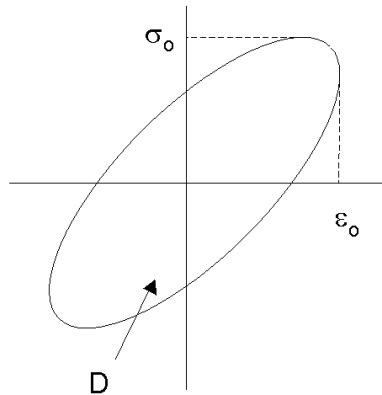


**Figure 2.2:** A Hysteresis loop, where  $\sigma$  is the loading (stress),  $\epsilon$  the extension (strain) and D is the energy lost during one loading cycle.

### Hysteretic damping in SPI of an OWT

A monopile of an OWT dissipates energy through hysteretic damping caused by the friction in the granular structure of the soil (a hysteretic loss), dependent on the strain (displacement) and in phase with velocity of the pile. Hysteretic or material damping is always present at these soil-pile interactions.

### **Radiational damping**

Besides friction and viscosity, a system can also lose its energy to *geometric* damping. Geometric damping is the spreading of local energy over the geometry of a system and its environment.

A well-known example clarifies this description; when throwing a stone onto the water surface (a point source): the waves travel from this point in all directions (x-,y- and z-axis). The energy released in the point source is distributed over an increasing geometric space with time, resulting in lowering wave amplitudes with further distance from the point source. Figure 2.3 clarifies this example.

So geometric damping is the phenomenon of energy distribution over an ever growing volume of the environment by the transmitting, radiating waves. That is why it is sometimes referred to as ‘wave-making’ or ‘radiational’ damping. The magnitude of this type of damping is, amongst others, dependent on the amount of energy that waves can obtain in the surrounding medium of the system: an oscillating mass loses less energy to waves when surrounded by air than when surrounded by water.



**Figure 2.3:** The energy of a point source is spread via radiational damping

### Radiational damping in SPI of an OWT

A monopile dissipates energy into the ground in a radiational way by the transmittal of elastic waves. As the energy of these waves in most media depend on frequency, this radiational damping is usually frequency dependent.

The (horizontal) *cut off* frequency of the surrounding soil layer can be approximated with [18]

$$f_H = \frac{V_s}{4H} \quad (2.1)$$

In which  $H$  is the soil layer thickness, and  $V_s$  is the *shear wave velocity*.<sup>1</sup>

Radiation damping can be of a large magnitude, but it only becomes significant above a certain threshold frequency value of the vibration. Only when the frequency of the pile vibration comes close or is larger than the cut off frequency of the surrounding soil layer (given by equation 2.1), radiation damping becomes significant and dominant. This is however not the case for the low frequencies

<sup>1</sup>A list of used symbols of the model developed in this thesis is printed in appendix H. All the other variables and symbols in this report will be explained and named when they are mentioned in the text.

of oscillations of OWT's. For OWT's material damping is seen as dominant, and radiational damping as insignificant [37]. In figure 2.4 a graphical indication is depicted for the radiational and material damping components in soil-pile interaction and their dependency on frequency of the pile.

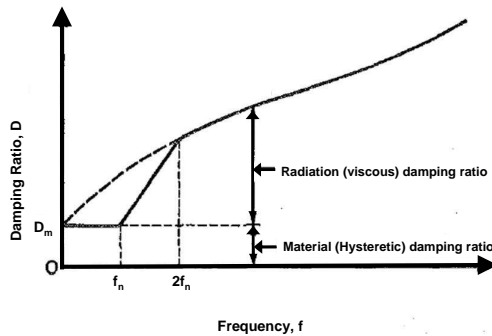


**Figure 2.4:** Soil damping components and frequency-dependency.  $D_m$  is the material damping,  $f_n$  the natural frequency of the surrounding soil layer. [9]

## 2.2 Measuring Damping

The magnitude of a certain damping mechanism can be identified from measured responses of systems. These experiments or measurements can be performed on full-scale structures that are given a certain excitation (a force is applied, or an initial displacement is given to the structure) or on scale models in a laboratory. The vibration decrement can subsequently be recorded with, for instance, the use of accelerometers or strain gauges that measure the response of the structure in time.

The identification of damping is not a straightforward and unambiguous exertion. Each identification technique has its limitations and subjective aspects. Stating a certain range of magnitude of the present damping is usually the best achievable result.

Some damping identification techniques can be used directly on the acquired time-signals (time-domain), and other techniques are applicable in the frequency domain of the measured signal. For the latter techniques, the time domain signal is transformed to the frequency domain by applying for instance a Fourier or Laplace transform on the original measured time-series. A brief explanation of the Fourier and Laplace Transforms is given in respectively appendix D and section 4.1.3.

One can also measure the magnitude of damping in a certain material (rather than in a system or process as soil-pile interaction), such as for instance soil. Different in situ and laboratory tests exist yielding mainly the material damping potential of the soil. These tests are described in appendix B.

In this research, most damping assessments on the measured data were done using the Quality factor (Q-factor) technique in the frequency domain. This technique is sometimes also called the Half-power Bandwidth method. A brief explanation of time-domain techniques and the frequency-domain Q-factor technique is given here.

### Time-domain Techniques

In these paragraphs, three time-domain techniques will be discussed without going into (mathematical) detail.

A way of quantifying viscous damping in an under-damped system is by calculating the *logarithmic damping decrement* usually denoted as  $\delta$ . This is a frequently used technique to determine the damping of a system from a measured response in the time domain. In figure 2.5 the dotted line through the peaks of the curve is the exponential relation between these peaks. One takes the natural logarithm of the ratio of subsequent 'peaks' or amplitudes ( $x_0$  and  $x_n$  in the figure) and divides it over the amount of periods 'n'. In formula form;

$$\delta = \frac{1}{n} \ln \frac{x_0}{x_n} \quad (2.2)$$

The relation between the damping *ratio* and the logarithmic damping *decrement* is as follows:

$$\zeta = \frac{1}{\sqrt{1 + \left(\frac{2\pi}{\delta}\right)^2}} \quad (2.3)$$

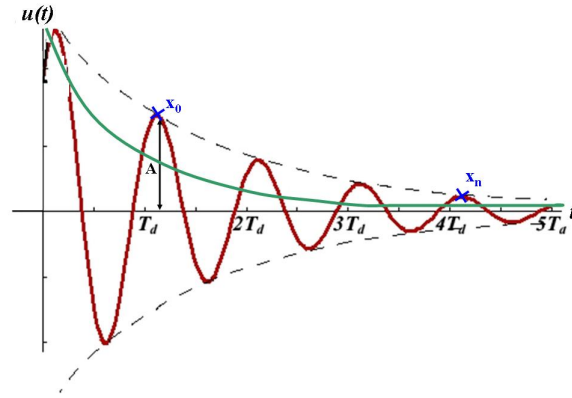


**Figure 2.5:** Typical displacement-time relation of an under-damped (red) and a super-critically damped (green) system after an initial excitation. The amplitude peaks are used for logarithmic decrement determination.

Looking at this relation, one could say that as an approximation  $\zeta \approx \frac{\delta}{2\pi}$  if  $\delta \ll 4\pi^2$  which is usually the case for wind turbines.

The dotted decrement line in figure 2.5 can be described with

$$u(t) = Ae^{-\zeta\omega t} \quad (2.4)$$

with  $\omega$  the frequency (in radians per second) of the oscillations of the red line in the same figure, and  $A$  the initial amplitude of the oscillation. Plotting this decrement line in the measured time response can serve as a check on the found damping ratio  $\zeta$  for the main present frequency in the response. This also reveals a limitation of this technique: it is limited to identifying the damping of the total response, which is usually a summation of numerous harmonics with different frequencies. This technique can only be used if the total response is strongly dominated by a specific frequency, and is thus limited to identifying only the damping of the vibrations of that specific frequency.

Another time domain technique is the *Hilbert damping analysis*. Unlike other damping identification techniques, this technique does not assume viscous damping, and can also identify non-linear damping mechanisms. The Hilbert transform can compute the transient decay envelope of a signal from which the

damping ratio can be derived. The transform is a convolution integral giving the original signal a  $90^\circ$  phase shift. Other products of the Hilbert transform are the *the instantaneous phase angle* and *the instantaneous frequency* which are of benefit when studying non-linear damping [33] .

The final damping identification technique that is discussed here is the *Moving Block damping analysis*. In this approach basically a shifting Fourier Transform is applied; a FFT (Fast Fourier Transform, very similar to the DFT) is performed over a certain block of data, after which the block is moved forward a single point in time. For each block the transient response amplitude is calculated. All these amplitudes are plotted in time. The damping is estimated from the natural logarithm of the slope of the linear least mean square fit through the amplitude peaks. Because of this ‘careful sliding’ (of the time window/block), this technique is especially well suited for distinguishing between closely positioned neighboring natural frequencies [33].

### Frequency-domain Technique

When looking at a response signal in the frequency domain, one can see the occurring frequencies in the signal as peaks with their associated energy and dissipation of this energy. Such a graphical representation is called a *power spectrum*. A power spectrum is found by taking the square of the absolute value of the Fourier-transformed signal.

The skewness (height/width ratio) of such a frequency peak is a measure for the way that frequency is damped; the higher and narrower the peak, the lesser the vibration is damped at this frequency. The Quality factor (Q-factor) technique incorporates this characteristic to determine the magnitude of damping. Physically, Q is  $2\pi$  times the ratio of the stored energy over the dissipated energy in one period.

Figure 2.6 shows how to determine the Q-factor. In this figure, the power spec-

trum of a modeled rotor stop response is taken as an example.

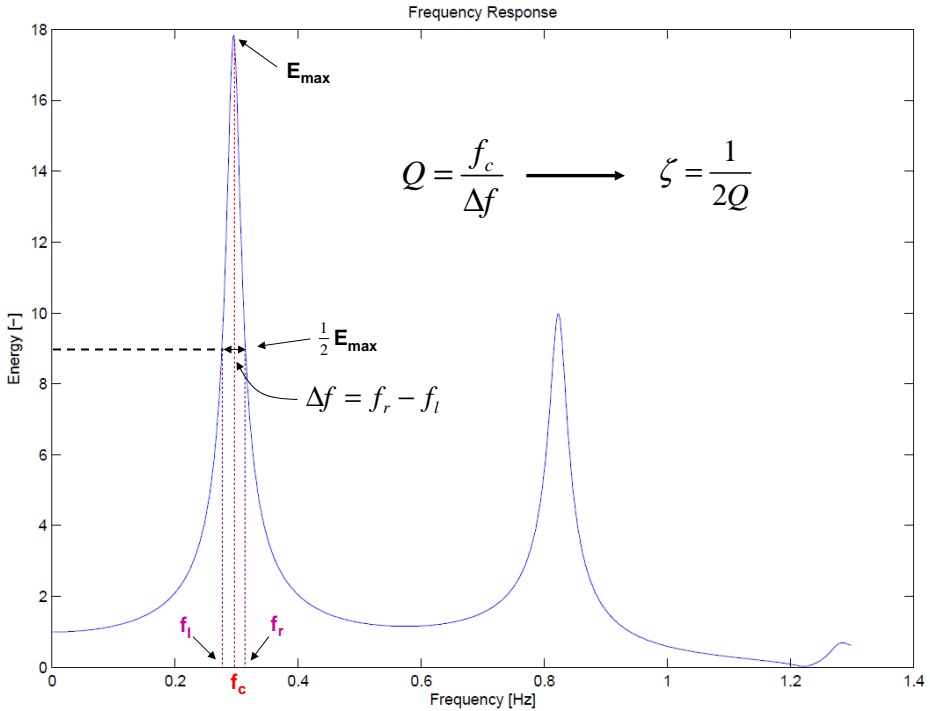


**Figure 2.6:** Determining the Quality factor (Q) and the damping ratio  $\zeta$  in the power spectrum of a signal.

One finds the maximum of the (normalized) peak, and determines the bandwidth between the two frequencies of the peak (left ( $f_l$ ) and right ( $f_r$ )) at the half of this maximum. The *center frequency*,  $f_c$  lies in the middle between these two frequencies.

Note that *normalized* in this context means that the peak under investigation should be normalized so that the left hand side (where frequency = 0 Hz) of the peak equals one (1), as can be seen in figure 2.6. The Q-factor is then simply calculated by;

$$Q = \frac{f_c}{\Delta f} \quad (2.5)$$

from which then the viscous damping ratio (of critical damping) is calculated by

$$\zeta = \frac{1}{2Q} \quad (2.6)$$

If the power spectrum is properly derived and normalized, the Quality factor technique is seen as an accurate and exact technique to determine the equivalent viscous damping ratio for the damping in the measured signal. It is a relatively fast-technique that directly differentiates the damping magnitude per frequency. The time-domain techniques were seen as more cumbersome because this differentiation is not directly applicable as the signal is a summation of frequencies and noise. Also, the previously described last two time-domain techniques involve a significant amount of processing. But more importantly, the Q-factor technique allows to assess damping identification of all frequencies that are present in a response, as opposed to the logarithmic decrement technique which is limited to assessing only a single frequency-dominated signal. Because of these reasons, the Q-factor technique was chosen to identify the damping in the acquired measurements.

It has to be noted that the Q-factor technique is limited to linear systems which are sub-critically damped. Also its reliability is reduced by the presence of white noise and closely spaced modal frequencies. The latter can be understood when looking at figure 2.6: if for instance a third peak (modal frequency) would be present at 3.5 Hz, both peaks of the natural frequencies of  $f_c$  (3 Hz in the figure) and the third peak of 3.5 Hz could be mistaken for being one peak with an averaged center frequency and a wider bandwidth, yielding a larger identified damping for a non-existing frequency.

## 2.3 Developed models for Soil-Pile interaction

In this section the focus is placed more upon the dynamic process, and more specifically on damping of a horizontally vibrating vertical pile in a soil profile - the focus of this thesis. The section is a short survey of part of the literature on SPI. It has to be noted that not much literature was found on the focus of this study, especially damping in soil-pile interaction in *offshore saturated* conditions was scarcely encountered. Two developed ‘beam on Winkler foundation’ models (one by Badoni et al. and one by Gazetas et al.) will be discussed. The models are quite similar, but the way of modeling the soil damping is different.

Various models have been developed to simulate the complex phenomenon of a vibrating pile in a soil profile in order to analyze the processes that play a role. The models vary in complexity and in fundamental way of solving, from simple single degree of freedom (SDOF)-systems to full Finite Element Method (FEM) models. An example of a FEM model of a pile in soil is given in figure 2.7.

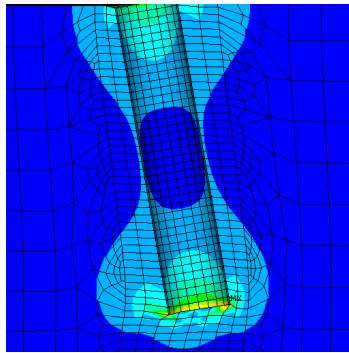


**Figure 2.7:** An example of a FEM model where the *mesh* size (element size) is adjusted according to desired accuracy in specific regions [39].).

A popular model for the soil reaction is the Winkler foundation model, which comprises a beam attached to distributed springs and dashpots. The way the foundation is modeled in figure 2.8 is an example of a Winkler foundation. Often the springs have a stiffness according to the so called *p-y* curves, where *p* stands for the soil reaction force caused by the induced displacement *y* of the specific soil layer at a certain depth which the spring represents [3].

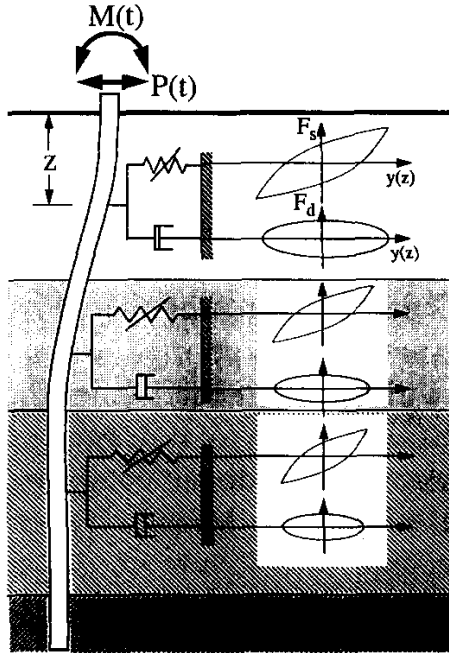


**Figure 2.8:** Soil-pile model with distributed non linear (hysteretic) springs and linear viscous damping (dashpots) [26]

For such a model, one can derive an *equation of motion* (EOM). An EOM is a mathematical description of the dynamic behavior of system, and it is basically a form of Newton's second law:  $F = ma$ . The homogeneous version (the right hand side of the equation equalling zero) of such an EOM of a beam on a Winkler foundation including damping and stiffness from the soil, and axis direction as in figure 2.8 reads

$$E_p I_p \frac{\partial^4 y}{\partial z^4} + m_p \frac{\partial^2 y}{\partial t^2} - F_s(z, t) - F_d(z, t) = 0 \quad (2.7)$$

with  $E_p$ ,  $I_p$  and  $m_p$  respectively the Young's modulus, the moment of inertia and the mass of the pile per unit length.  $F_s$  and  $F_d$  are the spring and damping forces. The first two terms in this equation are respectively the deflection or bending term because of the applied load, and the second term is the inertial reaction force. This equation was developed around 1750 by Daniel Bernoulli

and Leonhard Euler and this model of a beam is thus called the *Euler-Bernoulli beam*. For the derivation of this EOM, reference is made to the relevant literature, for instance [16] or [27].

Now the major question is what formulations one can apply for the dynamic reaction forces of the soil-pile system; how to model the spring stiffness and for this study even more relevant, the damping term of this equation. Methods to do so in literature slightly vary in this respect.

### **Badoni et al.**

In the model of figure 2.8 an attempt is made to simulate the linear response of soil for small amplitudes and the occurring material energy dissipation with hysteretic springs. The coefficients for these springs also incorporate the characteristic transition of linear elastic to more plastic reaction after a certain threshold displacement  $y_0$  of the soil. Via the frequency dependent dashpots the radiation damping is included.

This model turned out to be realistic and gave good correspondence with full scale (in the field) experiments, although it has to be said the solution has two empirical parameters that have to be fitted from experimental data. The model was developed by D. Badoni and N. Makris [26].

It is important to note that the experiments were performed on slender (large embedded length over diameter ratio:  $L/D$ ) piles with diameters smaller than one meter in saturated submerged soil. The phenomena in SPI occurring at piles with diameters in the range of monopiles can not be linearly extrapolated from that of slender piles [39].

In this case, it was found that the non-linear soil stiffness could be represented by

$$F_s(z) = \lambda(z)S(z)d\zeta \quad \text{for cohesive soil} \quad (2.8)$$

$$F_s(z) = \mu\gamma_s d \frac{1 + \sin\phi}{1 - \sin\phi} z\zeta \quad \text{for cohesionless soil} \quad (2.9)$$

where  $\lambda$  is a dimensionless term indicating the roughness of the pile according

to the soil pressure.  $\lambda$  varies between 3 and 9 with the following relation

$$\lambda(z) = 3 + \frac{\sigma_z}{S(z)} + J \frac{z}{d}, \quad \text{for } z < \frac{6d}{\frac{\gamma_s d}{S(z)} + J} \quad (2.10)$$

$$\lambda(z) = 9, \quad \text{for } z \geq \frac{6d}{\frac{\gamma_s d}{S(z)} + J} \quad (2.11)$$

Further,  $S(z)$  is the shear strength of the soil varying with depth ( $z$ ),  $d$  is the pile diameter,  $\gamma_s$  is the specific weight of the soil in question ( $\gamma_s = \rho_s g$ ),  $\phi$  is the internal angle of friction of cohesionless soil and  $\mu$  is an empirical parameter that has to be calibrated. Usually  $\mu = 3$  is assumed.  $J$  is a variable that has to be determined by fitting to experimental data. Finally  $\zeta$  is a dimensionless quantity that gives the hysteretic (damping) character to this spring.  $\zeta$  is determined by the following relation;

$$y_0 \dot{\zeta} + \gamma |\dot{y}| \zeta |\zeta|^{n-1} + \beta \dot{y} |\zeta|^n - A \dot{y} = 0 \quad (2.12)$$

in which  $\beta$ ,  $\gamma$ ,  $n$  and  $A$  are dimensionless quantities that shape the hysteretic loop, and  $y_0$  the threshold displacement where the spring's reaction changes from linear elastic to more plastic behavior. In the above equations  $n$  also has to be determined by fitting to experimental data.

The damping force can be represented by

$$F_d = [Q a_0^{-0.25} \rho_s V_s d] \omega \langle y \rangle \quad (2.13)$$

$$\begin{aligned} & \text{with} \\ \langle y \rangle &= y_0 \text{ for } y > y_0 \\ & \text{and} \\ \langle y \rangle &= y \text{ for } y \leq y_0 \end{aligned}$$

In this equation  $a_0$  is the dimensionless frequency given by  $a_0 = \omega d / V_s$ , and a variable  $Q$  is introduced, which in turn is given by the expression

$$Q = 2 \left[ 1 + \frac{3.4}{\pi(1 - \nu_s)} \right]^{1.25} \left( \frac{\pi}{4} \right)^{0.75} \quad (2.14)$$

In this equation the *Lysmer's analog wave velocity* is used which is equal to  $V_{La} = \frac{3.4V_s}{\pi(1-\nu_s)}$ . This velocity is applied instead of the pressure wave velocity to take into account that a pure compression (wave) velocity  $V_p$  is only applicable in exactly the same direction as the oscillation of the pile [9]. This more realistic assumption is based on an adjusted Plane-Strain model of Novak [28] where the radiation field is split up in four planes with shear waves in the perpendicular planes and 'Lysmer' waves in the two planes in line with the oscillation. This model is clarified in figure 2.9.

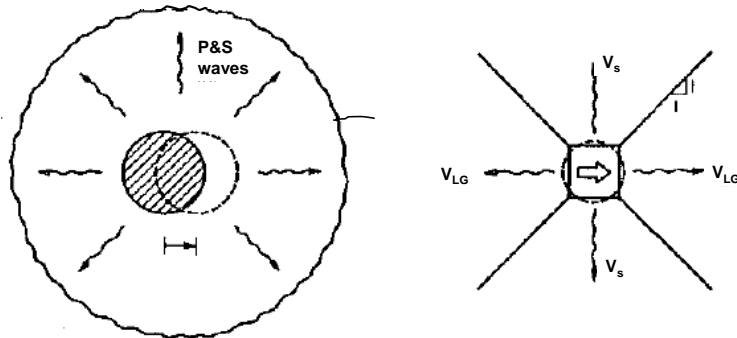


**Figure 2.9:** Plane-Strain radiation model originally proposed by Novak et al. (left) and adjusted model by G. Gazetas et al (right)[9]

Note that the part in between the brackets  $[Qa_0^{-0.25}\rho_s V_s d]$  in 2.13 is similar to a frequency dependent dashpot coefficient  $c$ , as for example given in equation A.1.0 in appendix A.

The total damping (both radiation and hysteretic), or the so called *equivalent damping* of the system, can be computed by looking at the area under the force-displacement loop  $W_d$  of the pile-head (the work performed by the damping force = energy) ;

$$c(\omega) = \frac{W_d}{\pi\omega y_{max}^2} \tag{2.15}$$

where  $y_{max}$  is the maximum pile-head displacement.

**Gazetas et al.**

A similar, but slightly different approach can be found in other literature, for instance G.Gazetas [9];

Assume a pile head is subjected to a dynamic lateral load  $F(t) = F_0 e^{i\omega t}$ , then the *impedance function* of the pile-head can be given by

$$K + i\omega C = \frac{F_0}{y_d} \quad (2.16)$$

where  $y_d$  is the amplitude of the displacement,  $K$  is the *equivalent* spring stiffness and  $C$  the *equivalent* dashpot coefficient of the *total* system. Impedance here means 'resistance', so this function is a measure of how much the system *opposes* an induced forcing or displacement. The complex nature (the 'i' in 2.16) of this function originates from the presence of damping: it causes the induced force and the resulting displacement to be out of phase. The dashpot coefficient  $C$  here represents the energy loss due to both material and radiation damping. The *equivalent* damping ratio  $D$  from this impedance function can be computed by

$$D = \frac{\omega C}{2K} = \frac{\pi f C}{K} \quad (2.17)$$

Instead of modeling the material and radiation characteristics via a hysteretic spring and frequency dependent dashpot as was done in the previous section, one can also apply two dashpots: a material and a geometric (radiation) one. These, together with the springs, can be distributed over the pile length.

The expression for the radiation dashpot coefficient  $c_r$  is similar to the one in between rectangular brackets in equation 2.13, so  $[Qa_0^{-0.25}\rho_s V_s d]$ . Though in this model it is taken into account that the dashpots for the shallow soil depths are more influenced by surface waves rather than body waves (the shear and Lysmer waves). Surface waves have lower velocities than shear waves, so the expression in 2.13 overestimates the dashpot coefficient for shallow regions of the soil. Instead, for the region up to  $2.5 \times d$  it is suggested to use

$$c_r = 2\left(\frac{\pi}{4}\right)^{0.75} a_0^{-0.25} \rho_s V_s d \quad \text{for } z < 2.5d \quad (2.18)$$

The material dashpot coefficient  $c_m$  is dependent on the hysteretic damping ratio  $\beta(z)$  which in turn is a function of the amplitude of the induced shear

$\gamma_e$	$10^{-5}$	$10^{-4}$	$10^{-3}$
$\beta$	0.02	0.05	0.10 – 0.15

**Table 2.1:** Material damping ratio's  $\beta$  dependent on strain amplitudes  $\gamma_e$

strains in the soil because of the oscillations. If a pile oscillates at a depth  $z$  with an amplitude  $y_d(z)$ , then the average shear strain amplitude can be computed by

$$\gamma_e(z) \approx \frac{1 + \nu}{2.5d} y_d(z) \quad (2.19)$$

The relation between damping ratio  $\beta$  and strain amplitude  $\gamma_e$  is empirically determined and numerous curves are available. Typical values can be found in table 2.1.

The material dashpot coefficient can then be computed by

$$c_m \approx 2k \frac{\beta}{\omega} \quad (2.20)$$

which is quite similar to equation 2.17. The difference here is that this expression is for a local dashpot which is part of the total distributed dashpot system, and expression 2.17 concerns the equivalent dashpot coefficient of all the distributed dashpots together. The relation between this total dashpot coefficient and the distributed dashpot values is given in equation 2.21. So  $k$  in the latter expression represents the local reaction stiffness of the soil to the induced deflection according to, for instance, p-y curves.

$$C = \int_0^L (c_r + c_m) \Upsilon_s^2(z) dz \quad (2.21)$$

in which  $\Upsilon_s(z) = y_s(z)/y_s(0)$  is the static deflection profile normalized to a unit top amplitude and  $L$  the length of the embedded part of the pile.

This model of Gazetas and Dobry was compared to FEM models and gave good correspondence. Also here the modeled piles were flexible beams; high L/D-ratio's, with pile diameters from 0.35m to 1.4m. The question remains if these models also apply for rigid behavior of piles with small L/D ratio's as is the case for the average MP in the offshore wind industry.

## 2.4 Current Design Practice and Damping Determination in the Offshore Wind Industry

In the offshore wind industry, the total damping acting on an OWT is calculated as the linear summation of the tuned passive sloshing damper in the nacelle, the aerodynamic damping acting on the rotating rotor and tower, hydrodynamic damping acting on the MP and transition piece (TP), structural damping in the entire construction and soil damping. These damping mechanisms are mainly assessed for the first natural bending frequency of the support structure. The foundation designer assesses all of these damping influences, except for the aerodynamic damping which is assessed by the turbine manufacturer.

For the determination of soil damping and these other mechanisms, the foundation designers often apply a calculation method developed by M.F. Cook ([37] and [6]).

### Cook's method

In this study from 1980, measurements of a single-pile platform in the Gulf of Mexico with a pile diameter of 2.13m are the basis of the model validation. In Cook's method to quantify the soil damping [6], an energy approach is applied: the total energy dissipated into the soil is linked to a soil material damping ratio, and the ratio of the soil-dissipated energy to the total energy in the pile platform is assessed. Cook also neglected radiational damping because of the low frequencies of excitation of the platform.

First of all a 'damping capacity parameter'  $\psi(z)$  is introduced which is a representation of the material damping ratio specified as the soil strain energy dissipated per cycle. It is expressed as  $4\pi$  times  $\zeta_{smd}$ , which is a constant soil damping ratio.  $\zeta_{smd}$  is believed to have a value somewhere in between 3 to 10%.

$$\psi(z) = \frac{D_z(z)}{U_z(z)} = 4\pi\zeta_{smd} \quad (2.22)$$

in which  $D_z(z)$  is the energy dissipated per cycle per unit length along the pile, and  $U_z(z)$  is the peak strain energy stored in the soil per cycle per unit length;

$$U_z(z) = \frac{1}{2}k_{soil}(z)X_p^2(z) \quad (2.23)$$

where  $k_{soil}(z)$  is the modeled soil spring stiffness per unit length and  $X_p(z)$  is the peak lateral displacement of the pile. When combining equations 2.22 and 2.23, and if the displacement of the top of the pile is  $A_0$  and integrating over the pile's length, one obtains the total energy dissipated within the soil,  $D_{TS}$

$$D_{TS} = 2\pi\zeta_{smd}A_0^2 \int_0^z k_{soil} \cdot \psi(z)dz \quad (2.24)$$

where  $\psi(z)$  is the value of the modeshape at depth  $z$ . Of an equivalent SDOF system the energy loss per cycle because of the soil damping coefficient  $R_{soil}$  would be

$$D_{eq} = \pi A_0^2 \omega R_{soil} \quad (2.25)$$

Now combining equations 2.24 and 2.25 and solving for  $R_{soil}$ , one gets

$$R_{soil} = \frac{2\zeta_{smd}}{\omega} \int_0^z k_{soil} \cdot \psi(z)dz \quad (2.26)$$

Taking the definition of damping ratio given in appendix A into account, expression 2.26 corresponds to a SDOF equivalent damping ratio of

$$\zeta_{soil} = \frac{\zeta_{smd}}{M\omega^2} \int_0^z k_{soil} \cdot \psi(z)dz \quad (2.27)$$

With  $M$  the modal mass of the structure.

## 2.5 Summary & Discussion

In this chapter three types of damping were discussed: viscous, hysteretic and radiational damping. It is expected that mainly the first two of these are present in the dynamic soil-pile interaction of a monopile based OWT.

In the second section different damping identification techniques are explained, with a focus on the Quality (Q) factor technique which is the technique used in this research. It is thought to be an accurate technique which is relatively fast and simply applied. The Q-factor technique renders the amount of damping related to each frequency in a signal.

In the third section, descriptions of two beam-on-Winkler foundation models from literature were given. In those models an attempt was made to express the coefficients of the damping dashpots and spring stiffness in soil parameters and some empirical-derived constants. In those studies, results of the models were compared with full-scale tests and FEM models, and gave good correspondence.

An important note to these models is that they are developed for slender flexible bending beams with L/D ratio of greater than 20, while the monopile foundations in the offshore wind industry have L/D ratio's of L/D smaller than 10 which cause a rather rigid behavior. The phenomena (both stiffness and damping) in soil-pile interaction occurring with rigid piles is not the same as with slender piles.

The last section renders the method in which the offshore wind industry currently assesses the amount of soil damping. The method was developed by M.F. Cook in 1980, and the paragraph on soil damping from the paper he wrote about his MSc thesis is the main reference today.

Soil damping values found with this method are low, and both Cook and the industry acknowledge that the actual values are expected to be higher. They recommend more research on this topic.

A first step in this further research is done in the next chapters which form the basis of this research. The results of the offshore field-tests are reported in the following chapter, and the model that was developed to analyze the measurements is described in chapter 4.

# 3

## Offshore Measurements

*This chapter starts with a description of the offshore rotor-stop tests that were performed. The acquired data is reported, after which the third section renders the output of the signal analyses: power spectra and identified damping values. The patterns in the power spectra of the signals are then discussed in the fourth section. The chapter is closed with a summary and discussion. In appendix D some first basics in signal analyses and the Fourier Transform are explained. Other studied offshore test opportunities and a possible roadmap towards the ultimate objective (see section 1.3.1) are given in appendix F.*

### 3.1 Performed Experiment

After exploring different opportunities for full scale offshore tests that were possible within Siemens Wind and their business partners, it was chosen to request performing *rotor stop* tests on the 'BB16' OWT structure of the DONG Energy-owned Burbo Bank (BB) windfarm.

Burbo Bank windfarm is a fully operational farm offshore the west coast of England close to Liverpool in the Irish sea. It consists of 25 Siemens SWT-3.6 MW turbines with a rotor diameter of 107m. BB16 (or sometimes called A6) is

one of the two OWTs in this farm equipped with strain gauges on the tower and an accelerometer in the nacelle.



**Figure 3.1:** Location of the BB16 offshore wind turbine on with which the rotor stops were performed.

A rotor stop is a relatively low cost test in which the operational turning rotor blades are pitched out of the wind with a relatively fast pitch speed. This fast pitching (six degrees per second) of a large blade angle causes the rotor to ‘suck’ itself forward into the wind. This movement and the gyroscopic effect of stopping the mass of the turning blades makes the nacelle initiate a mainly fore-aft movement that subsequently damps out (vibrational decrement). It is this vibrational decrement that is of interest for this research.

It was uncertain how valuable the information yield would be of such an experiment. Since measurement devices are only installed on the structure itself,

and no soil reaction is directly recorded, the possibility of actually stating something about the soil-pile interaction might be doubtful.

However, considering the low threshold (only costs of energy-loss due to the short shut downs, and the fact that the rotor stops are remotely controllable from the Siemens Wind main office in Brande, Denmark), performing these tests was seen as an appropriate first step for the roadmap that is described in appendix F. This appendix also elaborates on other test opportunities.

7 rotor stops were performed during low tide starting at 8:00AM (GMT+1) on the 29<sup>th</sup> of October 2010, and another 8 stops were done in the afternoon starting at 13:10 (GMT+1) of the same day during high tide. Having a tidal difference between the tests might allow for assessing the difference in damping of the seawater. Of these 15 tests, 3 tests involved the activation of a mechanical break on the rotor shaft during the final interval of blade pitching. The data of these tests was not used in this research, as the effect of the mechanical break was considered to have a disturbing effect on the vibration decrement of the structure. Effectively 6 useable tests were performed in the morning, and another 6 during the afternoon. After each stop, about a 13 minute pause was taken to let the structure reach steady state, damp out and start up the production again before initiating another stop. Figure 3.2 and table 3.1 give information of the test turbine, locations of the measurement devices and the environmental conditions during the rotor stops. In appendix C more details are given on the measurements.

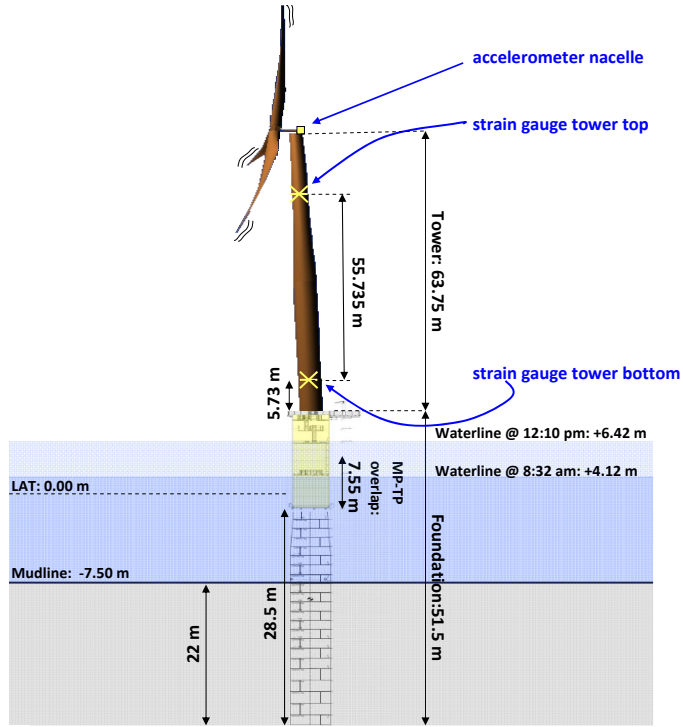


Figure 3.2: Schematic view of the OWT 'BB16' used for the rotor stop.

	Wind speed @ nacelle	Sign. Waveheight	Wind direction	Wave direction
Morning	10.96 m/s	0.62 m*	196°	158°*
Afternoon	19.7 m/s	0.59 m*	202°	160°*

**Table 3.1:** Environmental data during the experiment. All numbers with '\*' are forecasted data. It has to be noted that the windspeed during the afternoon was considerably higher then this predicted value, so the significant waveheight was probably higher then 0.59 m.

## 3.2 Obtained Data

BB16 is equipped with a PLM (Power Load Monitoring) system which has a sampling frequency of 25 Hz and has 34 synchronised channels of measured time signals.

Of these channels, 11 were of main interest for this research:

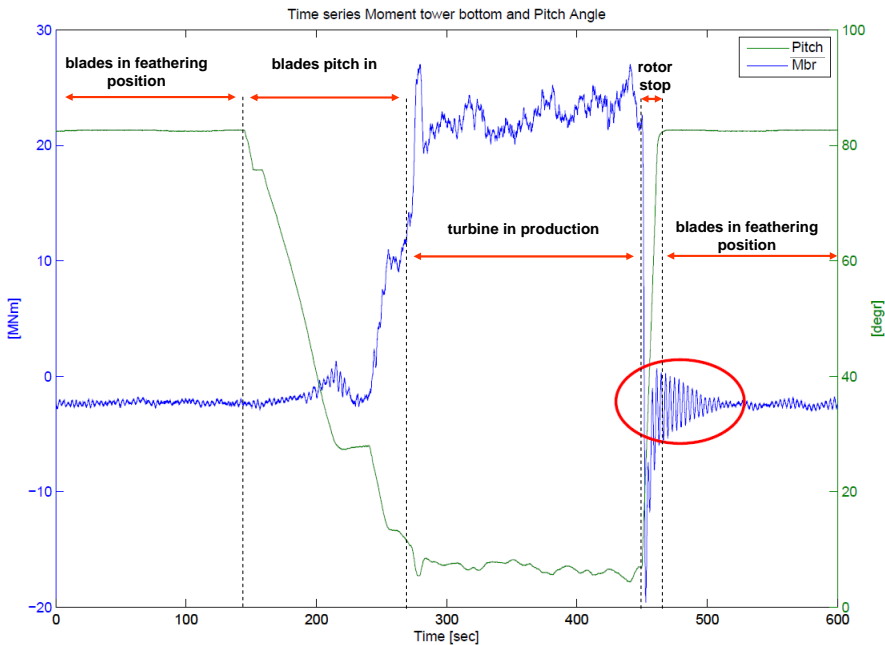
- the time line
- x- (fore-aft) and y- (side-side) directions accelerations of the nacelle
- x- and y-directions bending moment and the torque (torsional moment) at tower top
- x- and y-directions bending moment at the tower bottom
- pitch angle of the blades to be able to follow the advancement of the rotor stop.
- yaw angle of the nacelle (direction in which the rotor is faced), to be able to determine resulting bending moments.
- windspeed at the nacelle

Figure 3.2 depicts the locations of the strain gauges of the bottom and top locations. The y-bending moment corresponds with the binding of the structure about its East-West bounded axis. Likewise, the x-bending is the bending moment about the North-South directed axis. Documents with more details of the strain gauges and their location can be found in appendix C. The accelerometer in the nacelle is fixed to the nacelle which implies that its axes are fixed relative to the direction in which the rotor is faced, so fixed to the yaw-angle. That is why the x-direction of this accelerometer always corresponds to the fore-aft direction motion of the nacelle. Idem for the y-direction corresponding to the side-side accelerations.

The strain gauges are fixed to the tower having thus fixed axes relative to the tower. The total bending moment over the dominant axis was determined from the bending moment signals of x- and y- directions, incorporating the yaw angle. The maximum bending moment mostly exists over the axis perpendicular

to the rotor direction (yaw angle), as the fore-aft direction of the nacelle is the main direction of motion after a rotor stop. When mentioning the bending moment, it is this total moment which is always referred to in this report.

Each of the 12 tests are 10 min records, including a period of production, pitch-out (which causes the rotor to stop turning), vibration decrement, rotor stand still with blades in feathering position and pitch-in going back in production. These regions are shown in figure 3.3. In appendix C an overview of the time line of the morning test is given. An impression of the time series of the pitch angle and its effect on the moment at the tower bottom is given in figure 3.3.



**Figure 3.3:** Time series of the last rotor stop during the morning, test nr. 6. The influence of the pitch angle on the moment in the tower bottom is clearly seen. The red encircled part is of interest for this research: the decaying fore-aft movement of the tower.

A zoom-in on the red encircled vibration decrement region, the focus of this research, is given in figure 3.4.

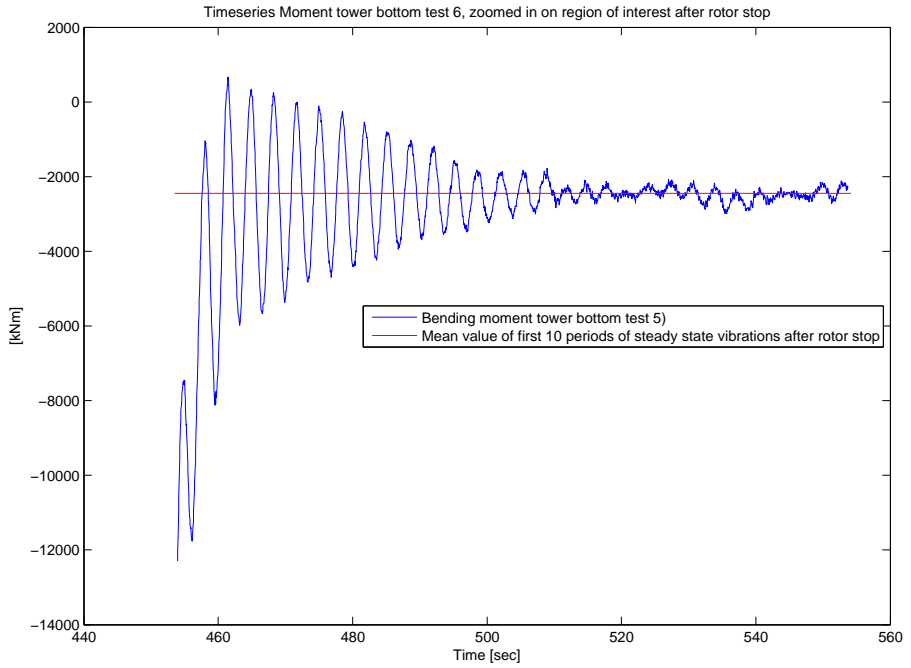


**Figure 3.4:** A zoom in on the red encircled part in figure 3.3 which is of interest for this research. The red line is the mean value of the first 10 oscillations of the linearly decaying vibrations after the rotor stop.

## 3.3 Data Analyses

In this section, the output of the Fourier analyses will be given, followed by the damping value results of the Q-factor analyses.

### 3.3.1 Power Spectra

Figures 3.5 and 3.6 depict the power spectra of the morning test for the fore-aft acceleration of the nacelle, the side-side acceleration of the nacelle, the bending moment at the tower top, the bending moment at the tower bottom and the torque at the tower top. Figures 3.7 and 3.8 show the same for the afternoon tests.

The power spectra were obtained by taking the absolute value of the Fast Fourier Transformed (FFT) time signal, and subsequently taking the square of this value. 40.96 seconds of time signal was taken of all the signals (similar regions as in figure 3.4) which was then multiplied with the Hanning window before performing the FFT. Also, the time signal was zero-padded by adding trailing zero's at the end of the time signal in order to increase the resolution of the frequency response.

Two main frequencies are present in the signal: the first natural frequency with an average of 0.296 Hz, and a second frequency at 0.825 Hz<sup>1</sup>.

---

<sup>1</sup>The true measurement resolution for the FFT is 0.0244 Hz. Frequency resolution = sampling frequency / sampling points, with sampling freq. = 25 Hz, and sampling points = 1024 (40.96 sec time window x sampling freq.). However, the FFT was zero-padded (adding zero's at the end of the time window) to increase the frequency resolution

### Morning tests

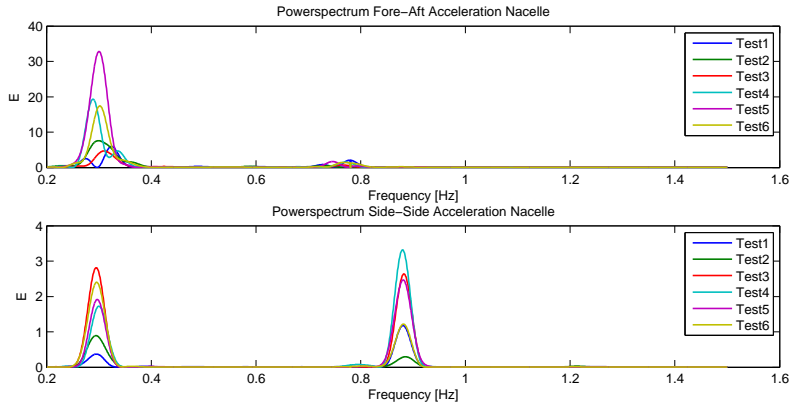


Figure 3.5: Power spectra of nacelle accelerations of the six **morning tests**

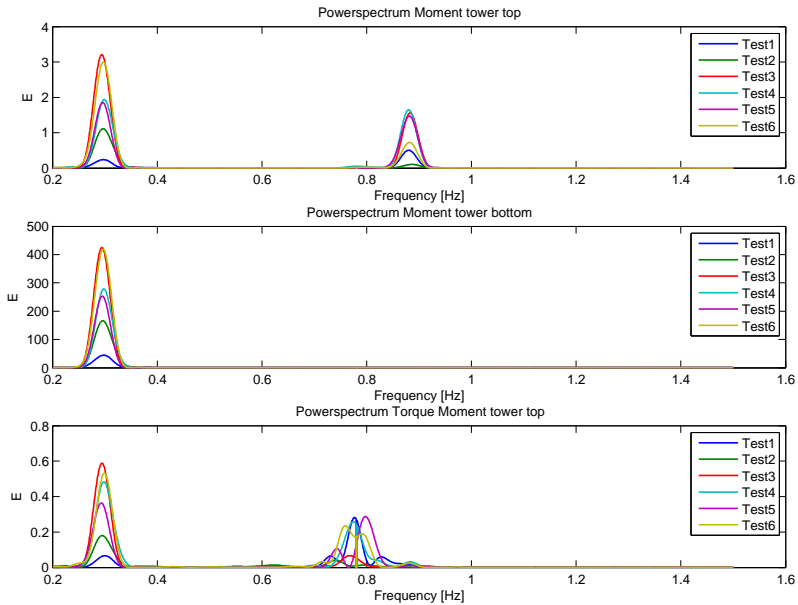


Figure 3.6: Power spectra of the moments along the tower of the six **morning tests**.

### Afternoon tests

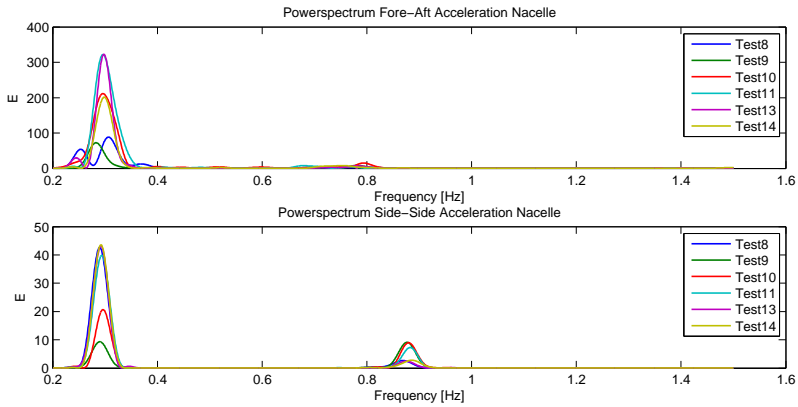


Figure 3.7: Power spectra of nacelle accelerations of the six afternoon tests

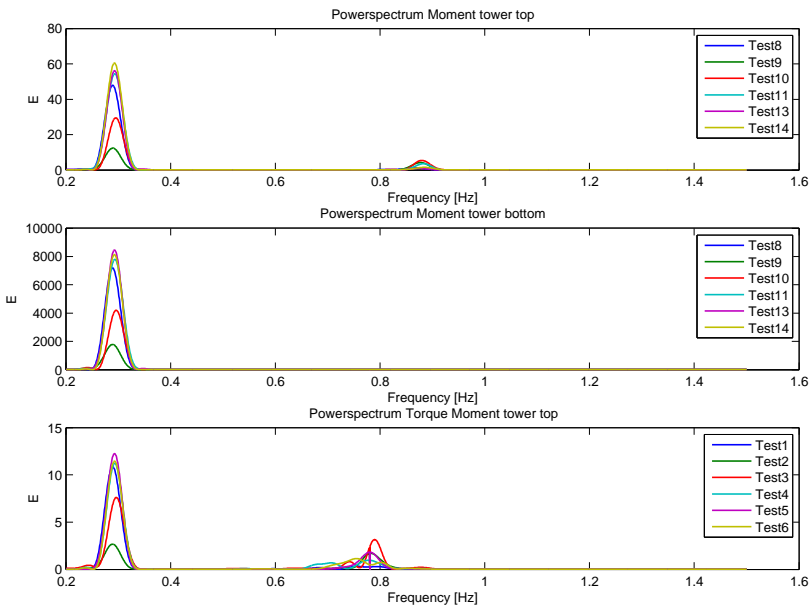


Figure 3.8: Power spectra of the moments along the tower of the six afternoon tests.

These plots were obtained incorporating the signal processing precautions and techniques (applying a Hanning Window, Nyquist frequency, folding etc.) as described in appendix D. As can be seen in the plots, the energy of the power spectra (y-axis) is not given a dimension. The calibration constants for especially the acceleration measurements were considered doubtful, and the numerical value of this energy is not important for the purpose of this research. It is more the patterns and the relative value that matters.

### **3.3.2 Damping Assessment**

The damping of the measured signals was assessed several times with varying techniques. As previously stated, the identification of damping is not straightforward, and the derivation of the power spectrum, the basis for the applied damping identification technique (Q-factor), is also not unambiguous. As will be discussed: there is no one true power spectrum, but rather different versions that depend on the application of window functions, that are again chosen with accordance of the goal of the research. In the next two sections, the results of two damping assessments will be discussed, of which the results of the second assessment are believed to be more realistic values for the damping that we are in search of: the effective equivalent viscous damping after a rotor stop excitation. The difference between the two assessments lies in the different approach of deriving the power spectrum.

#### **Damping results of Hanning-windowed sections of 41 seconds length**

From the acquired power spectra (as described and depicted in the previous paragraph §3.3.1), the damping was identified of the first two frequencies of all signals using the Q-factor technique. The application of the Q-factor technique is explained in §2.2.

The results of these analyses are summarized in the table shown in figure 3.9. The detailed results of all tests are given in appendix E.

	Average Frequency [Hz]	Average damp ratio $\zeta$ [%] of crit.	Av. overall Freq.	Av. overall Damp ratio $\zeta$ [%] of crit.	Log decr [%]
Acc 1st	0.302	6.309			
Mtop 1st	0.295	6.120			
Mtor 1st	0.294	5.973			
Mbot 1st	0.294	6.138	0.296	6.135	38.62
Acc 2nd	0.772	2.338			
Mtop 2nd	0.880	2.115			
Mtor 2nd	0.776	2.857			
Mbot 2nd	0.873	2.181	0.825	2.372	14.91
Difference in damping between two main frequencies:			$\Delta =$	3.762	23.66

**Figure 3.9:** Average frequencies and corresponding damping of the different signals of all tests. These values are again averaged, to derive the average *difference* in damping between the two measured frequencies.

Only the fore acceleration is assessed, Mtop indicates the bending moment at the tower top, Mtor the torque at tower top, and 1st and 2nd refer to the 1st and 2nd frequencies.

The identified damping values proved to be insensitive to shifting the time window of investigation (as red-encircled in figure 3.3). The found values for damping for pitch-out angles of 40 degrees (not entirely pitched out) were not generally more nor less than over a time window starting at pitch-out angle of 80 degrees (entirely pitched out, see figure 3.3 for better understanding).

The average bandwidth (deviance) of these averaged damping values over all tests was  $\pm 7.5\%$ . To evade ambiguity: a percentage of a percentage is meant here. The damping percentages of all tests deviated with an average of  $\pm 7.5\%$  of the average value given in the table of figure 3.9.

The influence of the tidal difference is not reflected in the identified damping values. Although some extra hydrodynamic damping might be expected, the damping values were found to be even slightly lower in the afternoon during high tide (2.3m difference with respect to the morning tests). The hydrodynamic damping seems to be of minor significance as compared to other mechanisms that are active in the damping of this structure. The expected magnitude of the hydrodynamic damping is discussed in chapter 4.

These acquired damping values have been derived with *non-normalized* power

spectra. Normalizing a power spectrum of a measured signal is not very straightforward. However, after having normalized part of the power spectra, the found damping values were usually higher, with a maximum deviation of 5% of the found values in the depicted table (the non-normalized values). So the here presented values could be seen as a lower limit.

### Damping results of Rectangular windowed first linear decaying cycles

However, the given values in figure 3.9 are most likely overestimates of the actual present damping directly after the rotor stop, because of the following three reasons.

First of all, note that the here presented damping values have been identified on power spectra of a 41 seconds long-time window that was multiplied with a Hanning window. However, a dependency exists of the shape of the power spectrum on the amount of periods (cycles) of vibrations that are incorporated in the analyses. This is caused by the fact that the pure Fourier transform is meant to be performed on an infinite time signal, and in practice we only incorporate an  $N$  amount of periods that we transform to the frequency domain. It can be proven that in doing so, the peak of a frequency  $\omega$  in a power spectrum is *underestimated* with an amount of

$$e^{\frac{-2N\pi(\zeta\omega+i\Omega)}{\omega\sqrt{1-\zeta^2}}} \quad (3.1)$$

times the theoretical value of a power spectrum (PS) when derived from an infinite time series, which is given by

$$PS = \left| A \frac{\omega\sqrt{1-\zeta^2}}{\omega^2 - \Omega^2 + 2i\Omega\omega\zeta} \right|^2 \quad (3.2)$$

with  $\Omega$  the running frequency along the x-axis of the spectrum,  $A$  the amplification giving the height of the peak and  $\omega$  the central frequency of the frequency in question. So the total analytical description of the corrected (for only incorporating  $N$  amount of periods) peak in the power spectrum derived from a finite time series is given by

$$PS = \left| A \frac{\omega\sqrt{1-\zeta^2}}{\omega^2 - \Omega^2 + 2i\Omega\omega\zeta} \right|^2 \cdot \left| 1 - e^{\frac{-2N\pi(\zeta\omega+i\Omega)}{\omega\sqrt{1-\zeta^2}}} \right|^2 \quad (3.3)$$

So if this factor is not incorporated in shaping the power spectrum of the finite time series, the peaks of the frequencies are depicted lower than they are in reality resulting in an overestimation of the damping values with the quality factor technique. This is the case for the damping values given in figure 3.9.

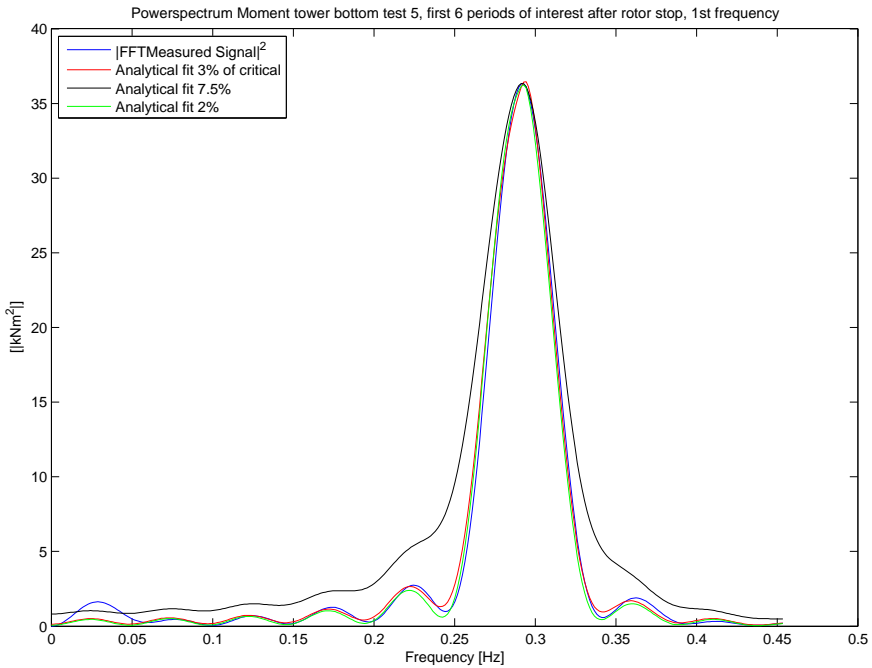
Secondly, apart from this factor, in this case also the timing and length of the selected time window has an influence on the eventual identified damping magnitude. First again the length: windows of 41 seconds have been taken for the identification. Further inspection on these windows indicate non-linearities to be seen in these time windows: only the first few periods (5 to 10 cycles) after the full rotor stop have a linear decaying trend. After these periods, the time series indicate a possible influence of another excitation of the structure or some other non-linearity. The 41 second-long time window cover both these linear decaying vibrations as the latter disturbances and non-linearities. Because of this reason, identifying the damping over this window will yield a different value than the linear equivalent viscous damping which is sought for in this research.

Last but not least, as mentioned, the Hanning window function has been applied on the time windows before taking the FFT. Application of the Hanning window yields a clean power spectrum without noise and spectral leakage. The peaks of the dominant frequencies are correctly depicted, both height and location-wise (location of the center frequency). However, the Hanning window does amplify the width of these peaks. This fact results in higher identified damping values when using the Q-factor technique. An assessment on the overestimating effect caused by the Hanning window on a modeled signal, indicated an overestimation of about 7 - 10% of the actual damping value. More explanation for the motivation for applying a window function and its effect is given in appendix D.

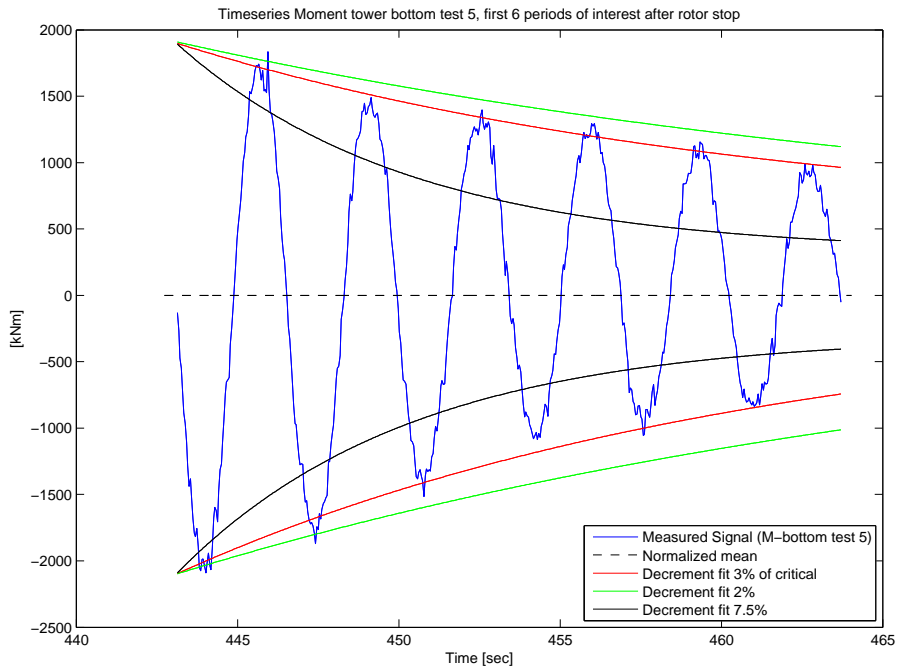
A further assessment was performed on tests 5 and 4 incorporating these three effects and measures (an analytical correction for taking a finite time record, only assessing the first few linear decaying cycles after the rotor stop and not applying a Hanning window function, but simply a rectangular window (which corresponds to not applying any window function)). Tests 5 and 4 are characterized by having frequency and damping values that are close to the average values of all tests presented in figure 3.9.

Figure 3.10 depicts the frequency domain assessment on the first 6 oscillation cycles after the rotor stop of the bending moment at tower bottom of test 5.

Only the first natural frequency is present at the bottom of the tower. A 3 % damping ratio fit gives best correspondence. This is confirmed by figure 3.11 in which time domain logarithmic decrement fits are depicted for this signal. It can be concluded that 3 % damping ratio is a good estimate for this time section of the signal.



**Figure 3.10:** Measured and analytical fitted power spectrum for first 6 cycles of the bending moment at tower bottom for test 5. Only the first natural frequency is present in this signal at the tower bottom. The fit with 3% damping ratio is found to be the closest fit.



**Figure 3.11:** Measured time response of first 6 cycles of the bending moment at tower bottom for test 5. The same fitted damping ratio's are plotted as logarithmic decrement. Again, the 3% damping ratio is found to be the best fit. The first natural frequency clearly dominates the time response.

To assess the second frequency, the signal of the bending moment at the tower top is analyzed. Figure 3.12 depicts good fits for the first natural frequency of again 3% and 1.6% for the second frequency. It is considered not to be valuable to fit a logarithmic decrement on a signal which is dominated by two frequencies, so that is why in figure 3.13 only the time response is given of the signal that was used for deriving this power spectrum.

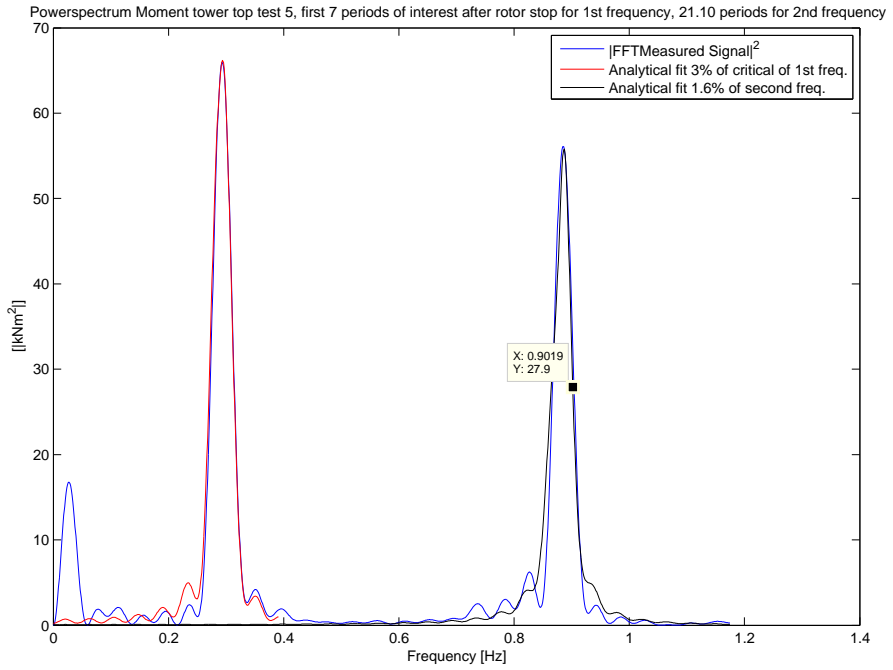


**Figure 3.12:** Measured and analytical fitted power spectrum for first 7 cycles of 1st natural frequency and 21 cycles for the second frequency of the bending moment at tower top for test 5.

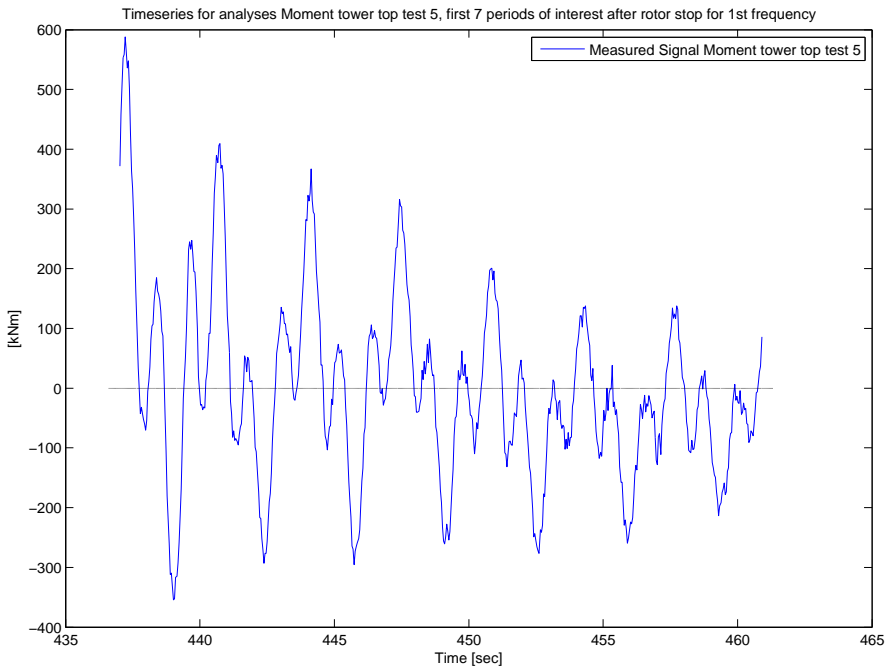


**Figure 3.13:** Time series taken for deriving the power spectrum for the first 7 cycles of 1st natural frequency and 21 cycles for the second frequency of the bending moment at tower top for test 5.

Similar analyses plots for test 4 can be found in appendix E. A summary of the results of these assessments on the initial vibrations of test 4 and 5 are given in figure 3.14.

	Test 4			Test 5		
	Frequency [Hz]	Damp ratio $\zeta$ [%] of crit.	Log decr [%]	Frequency [Hz]	Damp ratio $\zeta$ [%] of crit.	Log decr [%]
Mtop 1st	0.293	3	18.86	0.292	3	18.86
Mbot 1st	0.293	4	25.15	0.292	3	18.86
Mtop 2nd	0.877	1.5	9.43	0.883	1.6	10.05
Difference in damping between two main frequencies:				$\Delta \approx$	1.5	9.43

**Figure 3.14:** Damping values of rectangular windowed initial vibration cycles of tests 4 and 5. These vibrations are characterized by a linear decay pattern with low relative influence of other disturbances.

The identified damping values that are presented here are in the same order as those found in a previous research of LAC engineering in 2009, [30] which was performed on the same test turbine (BB16). The values that were identified in that research were in the range of 11 to 17 % log. decr. (1.75 - 2.71 % ratio of critical) for the first fore-aft bending frequency. This was identified using the Hilbert Transform technique on the time-series of 4 rotor stop experiments.

### Recommended Value

Based on the previous discussion on the influences of different signal processing aspects and the dependency of the time-region taken for analyses, the values found with the second presented analyses are expected to be more representative for the damping of the initial 5 to 7 vibration cycles after a rotor stop. These time regions seem to be dominated by linear decaying oscillations, with relative low influence of other disturbances or non-linear influences. This yields the opportunity to identify the equivalent linear viscous damping of the vibrations induced by a rotor stop. The magnitude of this damping is given in figure 3.14. These magnitudes are representative for all tests, as the values of tests 4 and 5 are close to the average values of all 12 tests. Summarizing it is stated that **the first natural bending frequency is damped with 3% ratio of its critical damping, and the second present frequency with 1.5% of critical. The difference in damping between the vibrations at these two frequencies is thus 1.5%.**

### 3.4 Patterns in Signal Output

When looking at the depicted power spectra, some main phenomena are noticeable, which in turn give rise to some questions.

- Every sensor/location shows the first natural frequency at an expected position; 0.296 Hz is within the usual frequency bandwidth of the first bending frequency of such a tower and top mass. However, the frequency of the second bending mode<sup>2</sup> of a beam is as a rule of thumb at least a factor 4 higher than the first. So if the first natural frequency would be found at 0.29 Hz, the second bending frequency would be expected to be found at no lower than 1.2 Hz. Nevertheless, a second resonant frequency is present at 0.825 Hz. This cannot be associated with the second bending mode, therefore giving rise to question **what causes this second resonant frequency? What motion is associated with it?**
- The **second frequency is only present at the top of the structure** (Acceleration nacelle, bending moment tower top, torque tower top)
- **This second frequency** is always present in **side-side acceleration of the nacelle**, less so in Fore-Aft directed acceleration.
- This second frequency is always present in the Bending moment at the top during the morning, little so during the afternoon.
- A third peak exists in the measurements at 1.213 Hz. This can be seen in the side-side acceleration power spectrum in the lower plot of figure 3.5, but is more noticeable in the logarithmic plot for the side-side acceleration measured in test 2 shown in figure 3.15. This third peak is expected to correspond to the second natural bending frequency and modal shape.

---

<sup>2</sup>Every natural frequency has its associated modal shape (or vice versa): the way the entire structure moves. More is explained in section 4.3

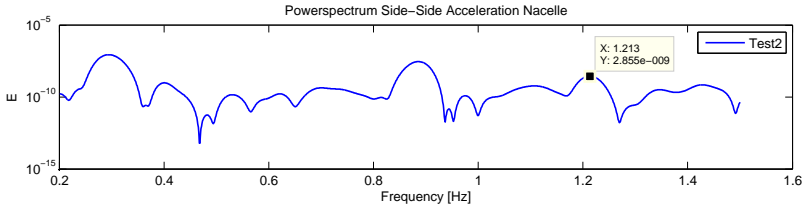


**Figure 3.15:** Logarithmic plot of power spectrum of side-side nacelle accelerations of the test 2. The third peak corresponding to the second natural bending frequency can be clearly seen (1.213 Hz).

When interpreting the outcome of the damping identification given in figure 3.9, the main question is

- Why is the second measured resonant frequency damped much less than the 1st natural frequency?

The combination of these trends and associated questions, raises the following question:

- What possibilities give these phenomena for the determination of the contribution of soil on the total damping of this structure?

## 3.5 Summary & Discussion

This section contains a summary that sums up what has been covered in this chapter and states the damping results. In the Discussion part, some more facts are stated that are then also interpreted, yielding possible causalities for patterns in the power spectra and the identified damping.

### 3.5.1 Summary

This chapter discloses the type of offshore tests that were performed and data that was acquired.

The power spectra of the fore-aft vibration decay recorded on different locations on the structure are depicted, and the results of damping analyses are summarized. Two damping assessment approaches were applied. The main difference between these approaches was the application of a window function and the length of the time signal to derive the power spectrum.

The found damping values of the analyses on only the first few linearly decaying vibration cycles without the use of a window function are found to be most representative for the equivalent viscous damping present on the vibrations of an OWT after a rotor stop. These identified damping values are quite high: 18.86% log. decr. (3% ratio) for the first natural bending frequency, and 9.43% log. decr. (1.5% ratio) for the blade frequency. A large difference (a  $\Delta$  of 9.43% log. decr.) in damping exists between the two main measured frequencies. The appraisal of the average measured damping value for the first natural frequency of almost 18.86 % log. decr. becomes more vivid in contrast to the 2.5 % log. decr. that was used to design the BB16 structure at the time. This 2.5 % was taken as the total damping without aerodynamic damping, which is basically the situation after a rotor stop after which the measurements were performed: the aerodynamic damping for completely pitched-out blades (idling position) is considered to be negligible. It has to be noted that nowadays (5 years later) larger values in the range of 6 to 8% log. decr. are applied for this damping are applied

The patterns in the depicted spectra and the large difference in damping value between the two frequencies give rise to some questions.

### 3.5.2 Discussion

#### Modal frequency of the blades

All records depict the first natural tower bending frequency at an expected value of 0.296 Hz. The second main frequency present in the signals has an unexpected center frequency of 0.825 Hz. The second main frequency for a tower (beam)-dominated structure would be expected to be associated with the second bending mode of the beam. The second bending mode of a beam (depending on its boundary conditions<sup>3</sup>) has a frequency of at least 4 times the first bending frequency. A closer look at the power spectra do indeed reveal a third peak at 1.213 Hz, which is expected to be associated with the second bending mode.

Also, this second identified resonant frequency seems to be localized at the top of the structure; only the nacelle accelerations and strain gauges at the top of the tower are associated with it.

Finally, the motion of this frequency is more side-side than fore-aft directed, as can be interpreted from the power spectra of the nacelle accelerations in these directions. Also the presence of this frequency is less pronounced during the afternoon than in the morning.

Considering these 3 phenomena, *this second frequency is expected to be associated with modal frequencies of the rotor blades.*

More explanation and justification for this statement is given in the next 4 paragraphs.

The blades are excited by the fast pitching over a large pitch angle. This causes a dominant forcing in the side-side direction of the nacelle. The main difference between morning and the afternoon test was the difference in wind speed.

---

<sup>3</sup>Boundary conditions are the conditions at the edges of a system; whether for instance the bottom of a tower is clamped (fixed for bending moment, horizontal and vertical movement) or if it has a top mass.

The wind speed in the morning, 10.96 m/s, was below nominal speed<sup>4</sup> for the turbine (13-14 m/s). In the afternoon the wind speed went up to 19.7 m/s, forcing the turbine to already partly pitch out its blades to reduce loads on the structure. The pitch-out angle for the rotor stops in the morning was about 82°, and 65° in the afternoon. This smaller difference in pitch angle ( $\Delta$  pitch) in the afternoon induces a lower excitation to the blades (despite the higher wind speed).

The vibration of the blades causes the top parts of the structure (nacelle and tower top) to vibrate. *It is expected that a localized mode shape is present at the top of the structure.* The transmittal of the motion of the blades to the lower part of the structure is limited, only the top part of the structure is excited.

More study on the B52 (52 meters long) blades this test turbine confirmed that their natural frequencies of 0.78 Hz is indeed closely located to the average measured frequency of 0.825.

Also Siemens' BHawC aero-elastic design model was consulted and simulations confirmed blade dominated trapped modes at the top of the structure with closely spaced frequencies at 0.783 Hz, 0.790 Hz and 0.835 Hz. This again is confirmed by the small spreading of frequencies between the tests that can be seen in the power spectrum of the torque at the tower top in figures 3.6 and 3.8.

### **Damping caused by the soil pile interaction**

The existence of these two different main modal shapes in the signal yields an opportunity to assess the influence of soil on the total damping of the structure. This is discussed in the next paragraphs.

The large difference in damping between the first natural frequency and this resonant frequency is remarkable, but by investigating the vibrational behavior

---

<sup>4</sup>A turbine has a nominal speed at which it starts producing its maximum design power output (in this case 3.6 MW). If the wind speed increases beyond this speed, the blades are partly pitched out according to the increase of wind speed with respect to the nominal speed. This ensures that the loading from the blades on the structure does not surpass the design loads. If the wind speed increases beyond 'cut-out' speed (25 m/s for this SWT 3.6 MW), the blades are fully pitched out to idling position, and the turbine stops operation.

of the entire structure that is associated with these frequencies, this difference in damping might be understood.

Where the first natural bending frequency has a mode shape with horizontal motion over its full height, with increasing amplitude from bottom to top (this mode shape is depicted in the next chapter in §4.3), the mode of the second resonant frequency has its main (both displacement and velocity-) amplitudes at the top of the structure. This implies that the different damping mechanisms cannot have the same influence on these different modes.

The main difference in possible contribution is expected to be associated with the soil; amplitudes caused by the blade-modes are small in the lower part of the structure at mudline. Because of this, the damping mechanisms working in this lower part of the structure (structural, hydrodynamic and soil damping) have negligible magnitude. Hydrodynamic and structural damping in general cause low damping ratios (in the order of respectively 0.18 and 0.22 % ratio of critical for the first bending mode<sup>5</sup>), so that is why

*the difference in measured damping between the two frequencies is mainly attributed to the difference in possible soil contribution.*

This difference of 9.43 % log. decr. (1.5 % ratio) indicates an order of magnitude for the amount of soil damping in soil-pile interaction on the motions associated with the first natural bending frequency. Apart from a global opposed to local dominance of the motions of the two main frequencies, the mode shapes of these frequencies are similar: the OWT structure is shaped in the first natural bending mode at these two frequencies. This is shown in figure 4.6 in chapter 4. The order of magnitude for this soil damping applied in the offshore wind industry today lies in the region of 0.44 % log. decr.<sup>6</sup> (0.07 % ratio) for the first natural frequency.

The influence of the timing of the time window taken for analyses on the damping that is subsequently identified, can possibly indicate the presence of non-

---

<sup>5</sup>These damping values are averages from industry design documents of comparable designs based on M.Cook's method [37] and a literature example reference case [11]

<sup>6</sup>This is an example value taken from an industry foundation design document.

linear damping mechanisms in soil-pile interaction. One expected factor of influence is the reaction caused by pre-stressed soil: during high wind and wave loads on the structure in a certain direction, the soil is pre-stressed in that direction. The (homogeneous) soil will react differently than in situations with lower environmental loads coming from other directions. Different amplitudes of displacement cause different damping magnitudes. If the time window is shifted up or down the time-line of the signal, different damping values are identified. So stating one certain general damping value is in that case not possible: it is related to the magnitude of displacement of the OWT structure. In this respect we can ask ourselves if the damping of the vibrations after a rotor stop is as relevant as that of the vibrations occurring during production of the turbine. After all, the OWT is designed to be in production during most of its lifetime.

In the assumption of relating the difference in damping between the two frequencies to be caused by the soil, it has to be noted that a part of the experienced damping is frequency-dependent, so stating that the difference in measured damping is exactly equal and due to soil damping is not strictly correct.

The damping caused by the passive sloshing damper is another effect limiting this statement. The sloshing damper is tuned to only damp the motions corresponding to the dominant first natural bending frequency with a ratio of 0.32 % of critical, *for motions of the turbine when it is in production*. The damping influence the slosher has during a vibrational decay as in the measurements is not known in this research, but it will surely have an effect on both frequencies.

In this chapter some first main conclusions and assumptions have been stated. To further analyze and possibly confirm these assumptions, a model has been developed to simulate the response of BB16. The next chapter gives a detailed description of this model.

# 4

## Modeling the Support Structure

*Where chapter 2 discussed developed models from literature for soil-pile interaction, and chapter 3 described measurements on an actual monopile based-offshore wind turbine, this chapter describes the developed analytical model and its output for this research. The included features are discussed and the governing equations are explained and solved. The second section discusses the way the model was implemented; what values were used for the variables in the model and why. The output of the model is depicted in various figures in the third section; the frequency equation giving the modal frequencies is plotted, followed by the modal shapes of the first 4 frequencies and finally the responses of the model in both frequency and time domain are depicted. The final section recapitulates and relates the content of the chapter in the form of a summary & discussion.*

*The presented model is the product of a development trajectory, of which this final model was considered to be adequate for the purpose of this research. Appendix G describes one of the predecing models, and appendices H and I provide further supporting material for this chapter.*

## 4.1 Constrained Beam Model

To be able to analyze the measured data properly, a modeled response is created by simulating a strongly simplified rotorstop on a continuous analytical model. The developed model used to represent the BB16 OWT can be seen in figure 4.1.

The 'Euler-Bernoulli' approach of modeling the bending of a beam is used to derive the equation of motion and conditions for this constrained beam. For the derivation of these expressions of the bending of an Euler-Bernoulli beam, the reader is referred to literature, for instance [16] or [27].

The model is seen as a constrained beam, because it is not clamped or pinned at one of its ends, but rather a free-free beam which is constrained by significant stiffness and damping at its soil-embedded part.

In the next subsections, a description of the aspects in the model is given, followed by the equation of motion, the initial-, boundary- and interface conditions. The final subsection describes how these governing equations can be solved to find the modal shapes with their frequencies, the natural frequencies of the system and the frequency response.

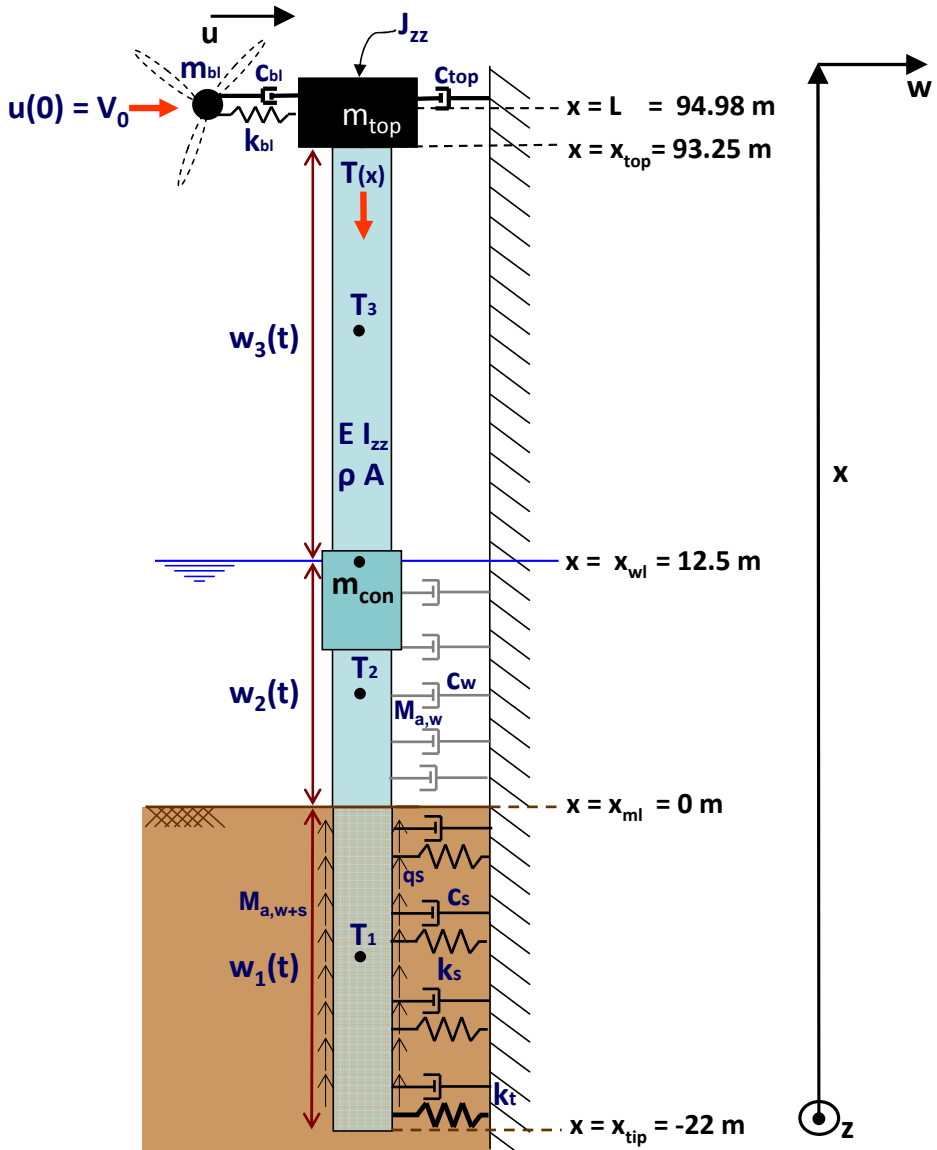


Figure 4.1: Extended model used to represent the performed rotor stops.  $x_{wl} = 12.5$  meter was the mean sealevel (waterline) during the tests.

### 4.1.1 Aspects of the Model

This section explains and refers to the graphical representation of the model which is depicted in figure 4.1. It discusses all the facets of this model from the bottom upwards.

The entire length of the support structure (from monopile tip under mudline up to tower top) of the BB16 turbine is modeled as a beam constrained in the soil by distributed springs with stiffness  $k_s$ , and damping dashpots,  $C_s$  representing respectively the soil stiffness and damping.

At the pile tip (22m under mudline) an extra stiff spring,  $k_t$ , is included to incorporate the extra stiffness of this transition and the extra shear force that is generated at the lateral sliding pile tip cross-sectional surface.

Further in the soil-embedded part of the beam, added mass of the seawater and the soil pile plug ( $M_{a,w+s}$ ) is incorporated. The soil pile plug is formed during the piling of the monopile: the hollow inside is filled with soil up to a height at which the total shaft-friction on the inside of the pile becomes larger than the pressure force on the full (solid) surface area of the cross-section at the pile tip.

The beam has a bending stiffness per unit vertical length of  $EI_{zz}$  or simply  $EI$ , with  $E$  the Young's modulus of the applied construction steel, and  $I_{zz}$ <sup>1</sup> the average moment of inertia, or more correctly *the second moment of area*, incorporating the average cross-sectional surface areas of the steel and grout of the MP, grouted connection, TP and tower.

The mass of the beam is  $\rho A$  in which  $\rho$  is the unit weight of the construction steel, and  $A$  the average cross-sectional surface area of the steel along the height of the structure (as described here above for the moment of inertia).

From mudline up to water surface, the effect of the seawater is incorporated by hydrodynamic damping, modeled by distributed dashpots with coefficient  $C_w$ , and added mass of the water,  $M_{a,w}$ .

The structural damping that can be expected in the construction materials in

---

<sup>1</sup>The 'zz' subscript of  $I_{zz}$  indicates that it concerns the bending moment of inertia around the z-axis (see figure 4.1).

the entire structure is included as an extra dashpot coefficient-value in the distributed soil damping  $C_s$ , and water damping  $C_w$  (not depicted in figure 4.1).

At the waterline, the extra mass of the grouted connection (an overlap of the MP and TP of 7.55m with a 83mm thick grout layer between them) is modeled as a point mass,  $m_{con}$ . To simplify finding the mathematical solution of this model, the center of gravity of this mass is layed on the interface level at the waterline. In reality this center of gravity is situated 2.2m lower, but this difference is not expected to have major influence in the model's behaviour.

The nacelle is modeled as a point mass,  $m_{top}$ , having a mass moment of inertia,  $J_{zz}$  or simply  $J$ .

At the nacelle a dashpot,  $C_{top}$ , is included that represents the passive sloshing damper which is installed in the nacelle of BB16. The aerodynamic damping after a rotor stop with blades pitched out of the wind is considered to be negligible.

The rotor with blades attached to the nacelle is modeled by an auxiliary mass-dashpot-spring system having a point-mass,  $m_{bl}$ , equalling the mass of the three blades, a blade stiffness,  $k_{bl}$ , and a damping dashpot,  $C_{bl}$ .

A frequency response as that of the measured tests can only be modeled by including this blade system. If this is not included, it is impossible to get the second resonant frequency as closely located to the first frequency as is the case in the measurements. See the discussion on second bending mode frequencies in section 3.4 and 3.5. Without this auxiliary system, the second resonant frequency of the system would be the second bending modal frequency of the beam, which has a frequency which is at least a factor 4 higher than the first natural bending frequency.

The rotor stop is modeled in a simplistic way by giving the rotor an initial velocity  $V_0$ .

Finally also the compressional force in the beam because of the weight of the rotor-nacelle-assembly (RNA) and the weight of the beam itself is modeled as a pressure force  $T$ .  $T$  is simplistically modeled as having three different constant values for three regions of the beam:  $T_1$  is the average pressure force in the top part of the beam up to waterline. This part of the beam is thus modeled

as being subject to this average pressure force,  $T_1$ . The same applies for  $T_2$  for the water-submerged part of the beam from waterline up to mudline. The decreasing effect of the buoyancy force of the water is incorporated in this average pressure force. In the pressure force for the soil-embedded part,  $T_3$ , the decreasing effect of both the water buoyancy force as the soil shaft friction,  $q_s$ , on the MP are included.

The values for all the applied physical variables are given in section 4.2 and appendix H.

### 4.1.2 The Governing Equations

The model presented in the previous subsections can be described with an *equation of motion* (EOM), the *initial conditions*, the conditions at the *boundaries* of the beam, and by the conditions at the *interfaces* between two subsequent sections of the beam. These sets of equations are called the *governing equations*. These are all mathematically described and explained in this subsection. The variables in these equations are all described in section 4.1.1.

The beam-model is split up in three parts, see figure 4.1;

1. The soil-embedded part from the pile tip at  $x=-22$  m to  $x=0$  m at mudline
2. The water submerged part from mudline up to watersurface at  $x=12.5$ m
3. and a top part from waterline up to nacelle height at  $x=94.98$ m.

The horizontal displacement of these three parts are respectively  $w_1(x, t)$ ,  $w_2(x, t)$  and  $w_3(x, t)$ . This separation is included to simplistically incorporate the fact that the values of the terms in the here presented EOM ( $m(x)$ ,  $T(x)$ ,  $C(x)$  and  $k_s(x)$  in eq's G.3 to 4.6) vary along the height of the beam. The method used to solve the subsequent governing equation, requires the values of the terms in the EOM to be kept constant over the length of these three distances. This gives the EOM the following form:

### The Equation of Motion

$$EI \frac{\partial^4 w(x, t)}{\partial x^4} + m(x) \frac{\partial^2 w(x, t)}{\partial t^2} + T(x) \frac{\partial^2 w(x, t)}{\partial x^2} + C(x) \frac{\partial w(x, t)}{\partial t} + k_s(x) w(x, t) = 0 \quad (4.1)$$

where

$$w(x, t) = \begin{cases} w_1(x, t) & x_{tip} < x < 0 \\ w_2(x, t) & 0 < x < x_{wl} \\ w_3(x, t) & x_{wl} < x < L \end{cases} \quad (4.2)$$

$$m(x) = \begin{cases} m_1 = \rho A + M_{a,w+s} & x_{tip} < x < 0 \\ m_2 = \rho A + M_{a,w} & 0 < x < x_{wl} \\ m_3 = \rho A & x_{wl} < x < L \end{cases} \quad (4.3)$$

$$T(x) = \begin{cases} T_1 & x_{tip} < x < 0 \\ T_2 & 0 < x < x_{wl} \\ T_3 & x_{wl} < x < L \end{cases} \quad (4.4)$$

$$C(x) = \begin{cases} C_1 = C_s & x_{tip} < x < 0 \\ C_2 = C_w & 0 < x < x_{wl} \\ C_3 = 0 & x_{wl} < x < L \end{cases} \quad (4.5)$$

$$k_s(x) = \begin{cases} k_{s,1} = k_s & x_{tip} < x < 0 \\ k_{s,2} = 0 & 0 < x < x_{wl} \\ k_{s,3} = 0 & x_{wl} < x < L \end{cases} \quad (4.6)$$

### The Initial Conditions

As a rotor stop is a complex excitation force to model, it was chosen to give an initial velocity,  $V_0$  to the auxiliary rotor mass,  $m_{bl}$ , of which the horizontal motion in time is described with  $U(t)$ . The system is not given any initial displacements, and also the initial velocity of the beam equals zero. In mathe-

mathematical form, this is stated as:

$$w(x, 0) = \frac{\partial w(x, 0)}{\partial t} = 0 \quad (4.7)$$

$$u(0) = 0 \quad (4.8)$$

$$\frac{\partial u(0)}{\partial t} = V_0 \quad (4.9)$$

### The Boundary Conditions

The boundary conditions of this model are as follows:

$$EI \frac{\partial^3 w(x_{tip}, t)}{\partial x^3} + k_t w(x_{tip}, t) + T \frac{\partial w(x_{tip}, t)}{\partial x} = 0 \quad (4.10)$$

$$EI \frac{\partial^2 w(x_{tip}, t)}{\partial x^2} = 0 \quad (4.11)$$

$$EI \frac{\partial^2 w(L, t)}{\partial x^2} + J \frac{\partial^3 w(L, t)}{\partial t^2 \partial x} = 0 \quad (4.12)$$

$$EI \frac{\partial^3 w(L, t)}{\partial x^3} + T \frac{\partial w(L, t)}{\partial x} - m_{top} \frac{\partial^2 w(L, t)}{\partial t^2} - C_{top} \frac{\partial w(L, t)}{\partial t} \quad (4.13)$$

$$= k_{bl}(u - w(L, t)) + C_{bl} \frac{\partial(u - w(L, t))}{\partial t}$$

$$m_{bl} \frac{\partial^2 u}{\partial t^2} + k_{bl}(u - w(L, t)) + C_{bl} \frac{\partial(u - w(L, t))}{\partial t} = 0 \quad (4.14)$$

The structure is constrained at its bottom tip by a horizontal translational spring  $k_t$  to incorporate the extra shear force that is generated at the lateral sliding pile tip cross-sectional surface. At this tip, a shear force equilibrium must exist with the pressure force  $T$ , and the bending stiffness  $EI$  of the beam. This condition is given in the first boundary condition (BC) of eq. 4.10.

Also, this tip of the pile should be bending moment-free, as stated in eq. 4.11.

The top free end of the beam is conditioned by the fact that the resulting bending moment (eq. 4.12) and shear force (eq. 4.13) should equal zero. The bending stiffness  $EI$ , the compressional force  $T$ , the inertia of the nacelle associated with  $m_{top}$ , the damping force associated with  $C_{top}$  and the forces of the

auxiliary spring and dashpot,  $k_{bl}$  and  $C_{bl}$ , should be in shear force equilibrium.

Lastly, the fifth BC gives the equation of motion of the auxiliary system representing the blades with their mass, stiffness and damping.

### The Interface Conditions

As the horizontal motion of the beam is described by three motions (eq. G.2), two sets of interface conditions are pertinent. The first set at location  $x=x_{ml}=0$  being:

$$w_1 - w_2 = 0 \quad (4.15)$$

$$\frac{\partial w_1}{\partial x} - \frac{\partial w_2}{\partial x} = 0 \quad (4.16)$$

$$\frac{\partial^2 w_1}{\partial x^2} - \frac{\partial^2 w_2}{\partial x^2} = 0 \quad (4.17)$$

$$EI\left(\frac{\partial^3 w_1}{\partial x^3} - \frac{\partial^3 w_2}{\partial x^3}\right) + T_1 \frac{\partial w_1}{\partial x} - T_2 \frac{\partial w_2}{\partial x} = 0 \quad (4.18)$$

These equations from top to bottom state that respectively the displacement, the slope, the moment (bending) and the shearforce in the lower part ( $w_1$ ) and the upper part ( $w_2$ ) at the interface are equal.

Analogously at location  $x=x_{wl}=12.5$ , the following interface conditions apply:

$$w_2 - w_3 = 0 \quad (4.19)$$

$$\frac{\partial w_2}{\partial x} - \frac{\partial w_3}{\partial x} = 0 \quad (4.20)$$

$$\frac{\partial^2 w_2}{\partial x^2} - \frac{\partial^2 w_3}{\partial x^2} = 0 \quad (4.21)$$

$$EI\left(\frac{\partial^3 w_2}{\partial x^3} - \frac{\partial^3 w_3}{\partial x^3}\right) + T_2 \frac{\partial w_2}{\partial x} - T_3 \frac{\partial w_3}{\partial x} = m_{con} \frac{\partial^2 w_2}{\partial t^2} \quad (4.22)$$

### 4.1.3 Solving the Problem in the Frequency domain

The above stated time-dependent governing equations will be solved in the frequency domain. To do so, the equations have to be transformed to the frequency domain by either a Fourier or Laplace transform. Because of the presence of initial conditions, the Laplace transform is applied.

In the next paragraphs a brief explanation of the Laplace Transform is given, followed by its application on the governing equations and the derivation of the solution.

The governing equations of this model can also be solved in the time domain. When interested in this technique, the reader is referred to appendix G, where a similar model is solved in the time domain.

#### The Laplace Transform

The Laplace transform is very similar to the Fourier Transform, and going into detail about their differences is beyond the scope of this report. Though worth mentioning is that when dealing with initial conditions, preference is given to the Laplace Transform. Where the Fourier transform (usually) integrates a function from minus infinity ( $-\infty$ ) to plus infinity ( $+\infty$ ), the unilateral Laplace transform transforms the function (which is often a function of time) from 0 to  $+\infty$ .

If the original function is  $f(t)$ , its Laplace Transform,  $\tilde{F}(s)$ , is defined as

$$\tilde{F}(s) = \mathcal{L}\{f(t)\} = \int_0^{\infty} f(t)e^{-st} dt \quad (4.23)$$

In literature, Laplace transform tables can be found, which give general properties of the transform. For this case the following list is of concern, where the original function is given on the left hand side, and its Laplace transform on the right hand side of the arrow:

$$f(t) \implies \tilde{F}(s) \quad (4.24)$$

$$\dot{f}(t) \implies s\tilde{F}(s) - f(0) \quad (4.25)$$

$$\ddot{f}(t) \implies s^2\tilde{F}(s) - sf(0) - \dot{f}(0) \quad (4.26)$$

where  $f(0)$  is the initial condition/value of the original function at  $t=0$ , and  $\dot{f}(0)$  is the value of the first derivative to time at  $t=0$  of the original function  $f(t)$ .

These expressions can be obtained by using the given definition of the Laplace transform and using integration by parts, or using the general formulation that is given by;

$$f^n(t) \implies s^n \tilde{F}(s) - s^{n-1}f(0) - \dots - f^{n-1}(0) \quad (4.27)$$

### Shifting to the Frequency domain

The Laplace transform is applied on the above stated governing equations, with the operator  $s$  in eq. 4.27 equal to  $-i\omega t$ . Doing so for the EOM of eq. 4.2, we get for the bottom part described by  $w_1(x, t)$ :

$$EIW_1'''' - m(x)\omega^2 W_1 + T(x)W_1'' + i\omega C_s W_1 + k_s W_1 = 0 \quad (4.28)$$

the middle part described by  $w_2(x, t)$ :

$$EIW_2'''' - m(x)\omega^2 W_2 + T(x)W_2'' + i\omega C_w W_2 = 0 \quad (4.29)$$

and the top part described by  $w_3(x, t)$ :

$$EIW_3'''' - m(x)\omega^2 W_3 + T(x)W_3'' = 0 \quad (4.30)$$

Doing the same for the boundary and interface conditions, we get:

$$EIW_1''''(x_{tip}) + k_t W_1(x_{tip}) + TW_1'(x_{tip}) = 0 \quad (4.31)$$

$$EIW_1''(x_{tip}) = 0 \quad (4.32)$$

$$EIW_2''(L) - \omega^2 JW_2'(L) = 0 \quad (4.33)$$

$$EIW_2''(L) + TW_2'(L) + \omega^2 m_{top} W_2(L) - i\omega C_{top} W_2(L) \quad (4.34)$$

$$-k_{bl}(U - W_2(L)) - i\omega C_{bl}(U - W_2(L)) = 0$$

$$m_{bl}(-\omega^2)U + k_{bl}(U - W_2(L)) + i\omega C_{bl}(U - W_2(L)) = m_{bl}V_0 \quad (4.35)$$

In this last boundary condition (4.35), the Laplace transform properties given in equations 4.25 to 4.26 and the initial conditions of equations 4.7 to 4.10 have been used. For reasons of simplicity, the dependency of  $U$  and  $W$  on  $s(= i\omega)$  is not depicted here.

Doing the same for the interface conditions at location  $x=x_{ml}=0$ :

$$W_1(x_{ml}) - W_2(x_{ml}) = 0 \quad (4.36)$$

$$W_1'(x_{ml}) - W_2'(x_{ml}) = 0 \quad (4.37)$$

$$W_1''(x_{ml}) - W_2''(x_{ml}) = 0 \quad (4.38)$$

$$EI(W_1'''(x_{ml}) - W_2'''(x_{ml})) + T_1 W_1'(x_{ml}) - T_2 W_2'(x_{ml}) = 0 \quad (4.39)$$

and the interface conditions at location  $x=x_{wl}=12.5$ :

$$W_2(x_{wl}) - W_3(x_{wl}) = 0 \quad (4.40)$$

$$W_2'(x_{wl}) - W_3'(x_{wl}) = 0 \quad (4.41)$$

$$W_2''(x_{wl}) - W_3''(x_{wl}) = 0 \quad (4.42)$$

$$EI(W_2'''(x_{wl}) - W_3'''(x_{wl})) + T_2 W_2'(x_{wl}) - T_3 W_3'(x_{wl}) + \omega^2 m_{con} W_2(x_{wl}) = 0 \quad (4.43)$$

## Finding the Solution

In this section the general solution for the location-related part  $W(x)$  is sought, which is then substituted in the governing equations to find the undamped natural frequencies of the modal shapes. Once these are found (to be correct), the damped natural frequencies of the system can be found by including the damping influences, yielding the frequency responses and the corresponding damping of the system. This all is done in the next paragraphs.

For  $W(x)$  we now presume the form  $W(x) = e^{i\beta x}$ . Using this in the acquired frequency domain expressions for the EOM (equations 4.28 and 4.30) and dividing by  $e^{i\beta x}$ , we get the *characteristic equations* for the bottom part:

$$EI \beta_{bot}^4 - m_1 \omega^2 - T_1 \beta_{bot}^2 + i\omega C_s + k_s = 0 \quad (4.44)$$

for the middle part:

$$EI \beta_{mid}^4 - m_2 \omega^2 - T_2 \beta_{mid}^2 + i\omega C_w = 0 \quad (4.45)$$

and for the top part:

$$EI \beta_{top}^4 - m_3 \omega^2 - T_3 \beta_{top}^2 = 0 \quad (4.46)$$

This yields us three times four relations for the  $\beta$ s.

For the  $\beta$ s of the embedded part at the bottom we get;

$$\beta_{bot,1} = \frac{1}{2} \frac{\sqrt{-2EI(-T_1 + i\sqrt{-T_1^2 - 4EI m_1 \omega^2 + 4iEIC_s \omega + 4EIk_s})}}{EI} \quad (4.47)$$

$$\beta_{bot,2} = -\frac{1}{2} \frac{\sqrt{-2EI(-T_1 + i\sqrt{-T_1^2 - 4EI m_1 \omega^2 + 4iEIC_s \omega + 4EIk_s})}}{EI} \quad (4.48)$$

$$\beta_{bot,3} = \frac{1}{2} \frac{\sqrt{2} \sqrt{EI(T_1 + i\sqrt{-T_1^2 - 4EI m_1 \omega^2 + 4iEIC_s \omega + 4EIk_s})}}{EI} \quad (4.49)$$

$$\beta_{bot,4} = -\frac{1}{2} \frac{\sqrt{2} \sqrt{EI(T_1 + i\sqrt{-T_1^2 - 4EI m_1 \omega^2 + 4iEIC_s \omega + 4EIk_s})}}{EI} \quad (4.50)$$

for the middle part:

$$\beta_{mid,1} = \frac{1}{2} \frac{\sqrt{-2EI(-T_2 + i\sqrt{-T_2^2 - 4EI m_2 \omega^2 + 4iEIC_w \omega})}}{EI} \quad (4.51)$$

$$\beta_{mid,2} = -\frac{1}{2} \frac{\sqrt{-2EI(-T_2 + i\sqrt{-T_2^2 - 4EI m_2 \omega^2 + 4iEIC_w \omega})}}{EI} \quad (4.52)$$

$$\beta_{mid,3} = \frac{1}{2} \frac{\sqrt{2} \sqrt{EI(T_2 + i\sqrt{-T_2^2 - 4EI m_2 \omega^2 + 4iEIC_w \omega})}}{EI} \quad (4.53)$$

$$\beta_{mid,4} = -\frac{1}{2} \frac{\sqrt{2} \sqrt{EI(T_2 + i\sqrt{-T_2^2 - 4EI m_2 \omega^2 + 4iEIC_w \omega})}}{EI} \quad (4.54)$$

and the  $\beta_s$  of the top part:

$$\beta_{top,1} = 1/2 \frac{\sqrt{2} \sqrt{EI \left( T_3 + \sqrt{T_3^2 + 4 EI m_3 \omega^2} \right)}}{EI} \quad (4.55)$$

$$\beta_{top,2} = -1/2 \frac{\sqrt{2} \sqrt{EI \left( T_3 + \sqrt{T_3^2 + 4 EI m_3 \omega^2} \right)}}{EI} \quad (4.56)$$

$$\beta_{top,3} = 1/2 \frac{\sqrt{-2 EI \left( -T_3 + \sqrt{T_3^2 + 4 EI m_3 \omega^2} \right)}}{EI} \quad (4.57)$$

$$\beta_{top,4} = -1/2 \frac{\sqrt{-2 EI \left( -T_3 + \sqrt{T_3^2 + 4 EI m_3 \omega^2} \right)}}{EI} \quad (4.58)$$

Because we presumed (and know) that the general solution has a harmonic form, and incorporating these different values for  $\beta$ , we can now write the general solutions for the location-related part  $W(x)$  as:

$$W_1(x) = A_1 e^{(i \cdot \beta_{bot,1} \cdot x)} + B_1 e^{(i \cdot \beta_{bot,2} \cdot x)} + C_1 e^{(i \cdot \beta_{bot,3} \cdot x)} + D_1 e^{(i \cdot \beta_{bot,4} \cdot x)} \quad (4.59)$$

$$W_2(x) = A_2 e^{(i \cdot \beta_{mid,1} \cdot x)} + B_2 e^{(i \cdot \beta_{mid,2} \cdot x)} + C_2 e^{(i \cdot \beta_{mid,3} \cdot x)} + D_2 e^{(i \cdot \beta_{mid,4} \cdot x)} \quad (4.60)$$

$$W_3(x) = A_3 e^{(i \cdot \beta_{top,1} \cdot x)} + B_3 e^{(i \cdot \beta_{top,2} \cdot x)} + C_3 e^{(i \cdot \beta_{top,3} \cdot x)} + D_3 e^{(i \cdot \beta_{top,4} \cdot x)} \quad (4.61)$$

Finally, these general solutions have to be substituted in the thirteen boundary and interface conditions (eq. 4.31 to 4.47), to get a linear system of equations for each  $\omega$  that can be solved for the thirteen unknown coefficients ( $A_1$  to  $D_3$  in 4.59 to 4.61 and  $U$  in eq. ??) by computing  $\underline{\mathbf{A}}\mathbf{x}=\mathbf{b}$

Here  $\underline{\mathbf{A}}$  is the coefficient matrix of the thirteen conditions,  $\mathbf{b}$  is the forcing vector which equals the right hand side of the BC and ICs and  $\underline{\mathbf{x}}$  the vector of thirteen unknown coefficients.

$$\text{So } \underline{\mathbf{b}} = \begin{bmatrix} 0 \\ 0 \\ 0 \\ 0 \\ m_{bl}V_0 \\ 0 \\ 0 \\ 0 \\ 0 \\ 0 \\ 0 \\ 0 \\ 0 \\ 0 \\ 0 \end{bmatrix}, \text{ and } \underline{\mathbf{x}} = \begin{bmatrix} A1 \\ B1 \\ C1 \\ D1 \\ U \\ A2 \\ B2 \\ C2 \\ D2 \\ A3 \\ B3 \\ C3 \\ D3 \end{bmatrix}$$

$\underline{\mathbf{A}}$  is too large to be printed here, but a similar but slightly smaller of such a coefficient matrix can be found in appendix G.

When the coefficient matrix is found, the natural frequencies of the modal shapes can be found by calculating the determinant of the coefficient matrix for each frequency  $\omega$ . This expression of this determinant is called the *frequency equation*. The natural frequencies can be found at the zero crossings of the frequency equation. It has to be noted that this has to be done for the undamped system. So to find the modal shapes, one has to equal all damping terms to zero.

So in short, if  $\underline{\mathbf{A}}$  is the coefficient matrix (without damping terms), the natural frequencies of the modal shapes can be found by;

$$\text{Frequency equation} = \det(A) = 0 \quad (4.62)$$

The modal shapes can now be found by solving the above mentioned equation of  $\underline{\mathbf{A}} \cdot \underline{\mathbf{x}} = \underline{\mathbf{b}}$  and eq.'s 4.47 to 4.61 for each location, x (in eq.'s 4.59 to 4.61), for the acquired natural frequencies ( $\omega$ 's) of the modal shapes.

Once the modal shapes are found to be correct (having the shape that we would more or less expect), the frequency response of the system (including the damping terms) can be found by solving the above mentioned equation of  $\underline{\mathbf{A}} \cdot \underline{\mathbf{x}} = \underline{\mathbf{b}}$  for each  $\omega$ .

## 4.2 Model Implementation

### 4.2.1 Model Variables

In general only realistic values (as found in the design documents from BB16 and industry and literature documents) were applied for all physical variables as discussed in §4.1.1. This section elaborates on the - mostly dynamics-related - parameters that deserve more attention on the way their value was determined.

#### The top dashpot, $C_{top}$

The top dashpot at the nacelle,  $C_{top}$  was initially tuned to model the passive sloshing damper which is designed to induce a damping of 2% log. decrement (0.32 % ratio of critical) on the first natural bending frequency. The dashpot value was later on increased, as will be explained in the final paragraph of this section.

#### The auxiliary blade system, $k_{bl}$ and $C_{bl}$

The dashpot modeling the damping of the blades,  $C_{bl}$ , was set to 1.73 % of its critical damping ( $C_{cr} = 2\sqrt{k_{bl}m_{bl}}$ , see appendix A). This dashpot value resulted in the same damping as was identified in the test signals for this second frequency.

$m_{bl}$  is found in design document and  $k_{bl}$  is set to reach the average measured modal frequency of the blades at 0.825 Hz:  $\omega = \sqrt{\frac{k_{bl}}{m_{bl}}}$

#### The hydrodynamic damping, $C_w$

The distributed dashpots,  $C_w$  modeling the hydrodynamic drag damping were

tuned to cause a hydrodynamic damping of 1.13 % log. decrement (0.18 % ratio of critical). This is the average value from the M.Cook-based damping assessment [37] from the industry and a value taken from literature of a comparable design [11].

When using a simplified expression assuming a viscous drag dashpot coefficient based on the Morrison equation, reading:

$$C_w = \frac{1}{2}\rho_w C_d D_o \quad (4.63)$$

with  $C_d$  the drag coefficient equalling 1, the resulting damping in the model was too low compared to the above mentioned expected value. A more realistic variable expression for the drag coefficient should be used, based on the Keulegan-Carpenter number (relation of the displacement amplitude of the pile and its diameter) and the Stokes parameter (relation of outer diameter-squared, the kinematic viscosity of the water and the period of oscillations)[14].

Applying this in a correct manner might yield expected values for this hydrodynamic drag damping. Instead, the dashpots were simply tuned to yield the expected values.

### The soil stiffness, $k_s$ and $k_t$

The distributed stiffness of the soil springs,  $k_s$ , is based on the MSc thesis of Philip Wegener [39]. In this study a critical evaluation was performed on the way the initial soil stiffness is currently assessed. The p-y curves of the API, developed for slender flexible piles with L/D ratios of more than thirty ( $L/D > 30$ , L is the embedded pile length), are still the basis for this assessment. Wegener showed that the initial stiffness is not comparable for the currently used large diameter monopiles with L/D ratio's smaller than ten ( $L/D < 10$ ) which also behave rather rigid than flexible. He suggested to - although two different parameters but with the same dimensions - couple the distributed stiffness,  $k_s$ , to the (constant) Young's modulus of the saturated soil,  $E_s$ , by introducing ratios for different L/D values. The soil is assumed to be homogeneous. For BB16, with L/D=4.68, a  $k_s$  value of

$$k_s = 1.48E_s \quad (4.64)$$

is applied. This is the ratio that Wegener proposed for L/D = 5. These ratios were based on comparison and matching between a Winkler-foundation based

model (as is applied in this model) and an elastic FEM model.

Modeling the distributed stiffness by one constant average value  $k_s$  which is applied for all depths, is quite a major simplification of reality. The stiffness should increase with depth, because of the pressure increase. But for the purpose of this model, this is an acceptable simplification.

The Young's modulus of the saturated sand (in this case) of the above stated relation is somewhat arbitrary in the way that it is not very straightforward to find this modulus. Especially considering the fact that an on average 12.5 m water column increases the pressure. Without this water column, the Young's modulus might lie in the range of 60 to 130 MPa. This is based on lower boundary and upper boundary densities for saturated sand and lower and upper boundary shear wave speeds [19]. In this model, a value of  $E_s = 130$  MPa is taken. Further on in this section a discussion is devoted to this.

The second suggestion of Wegener's work was to incorporate a pile tip correction factor because of the nowadays quasi-rigid pile behavior. As previously explained, the transition at the pile tip and the shear forces caused by the sliding tip make for the pile to locally experience an extra stiffness from the soil at its tip.

In this model, an extra stiff spring,  $k_t$ , is incorporated.  $k_t$  was set to be 11.5 times larger than  $k_s$ . Also this will be discussed further on in this section.

It has to be noted that Wegener's research naturally also includes assumptions and simplifications that limit its generic applicability. However, as this is one of the latest studies on the increased initial stiffness of soil in soil-monopileinteraction, incorporating part of his work is seen as a step in the right direction, and is thus taken as a starting point with respect to the soil stiffness.

### The soil damping, $C_s$

Finally, one of the major important variables in the model: the distributed dashpot value inducing the soil damping,  $C_s$ .  $C_s$  is linked to the distributed stiffness  $k_s$  by multiplying it with a value of  $3.9 * 10^{-2}$  times  $k_s$ . This value (in combination with other parameter values, as will be explained later on) gave the desired damping value of the soil. This value is the difference in damping measured between the two main frequencies as was identified in the assessment with longer time windows that were multiplied with a Hanning window. This difference is 23.66 % log. decr. (3.76 % ratio).

It should be understood that there is an interaction between the stiffness in the soil ( $k_t$  and  $k_s$ ) and the amount of damping that can be generated. From the measurements, an idea of the possible magnitude of soil damping is derived. The factor of  $C_s$  to  $k_s$  which has been applied is quite an upper level. A more usual measured factor of soil damping with respect to its stiffness would be in the order of  $C_s = 1 * 10^{-3} k_s$  [23] and [10].

Besides increasing this factor even more, the soil stiffness can be decreased to allow for larger motion and velocity amplitudes in the soil, thus allowing for more damping being generated. But then again, this stiffness can't be decreased too much, as then the frequency of the entire system becomes too low.

In short, the measured frequencies and damping values are a given, and the interacting variables of  $C_s$ ,  $k_t$  and  $k_s$  have been given values that were aimed at still - to a certain extent - being realistic.

To this extent, the average moment of inertia,  $I_{zz}$ , of the entire beam has been increased with 15% to match the measured frequencies. This might be justified, as the very stiff grouted connection has only been incorporated as an extra point mass and an increased weighted average cross section of the entire beam, but not, for instance, an increased Young's modulus,  $E$ .

But an important question that remains is:

parameter *Why is it challenging to model the measured soil damping in this way?*

It has to be noted that among the various models that were developed before the here presented model, a pinned beam model was developed. The effective stiffness and damping of the soil were modeled with a rotational and translational spring and a rotational dashpot. This model is described and solved in

appendix G. After adding also a translational dashpot, it was still *not possible* to model the amount of soil damping that is expected to be measured. The dashpot coefficients were given unrealistically high values, which were found to have an optimum value. Increasing the coefficient value beyond this optimum, decreased the amount of damping generated in the model. This way of modelling *effective* soil behavior (total generated stiffness and damping represented by single rotational and translational springs and dashpots) can for many studies be a sufficiently accurate way of modeling, but in this case it was too limited. Ignoring the mass of the imbedded beam, and the fact that more damping can be generated by the soil via distributed dashpots over a certain vertical height than one translational and rotational dashpot at one location, are already two limiting features of modeling *effective* behavior.

The soil damping in the final presented model is modeled as distributed *viscous* damping. These dashpots have been given values that are significantly larger than usual values in order to be able to model the measured soil damping of the tests. This way of modeling is thus limiting for representing the actual real phenomena in the soil-pile interaction.

It is expected that the solution to this limiting modeling problem can be found by incorporating other types of damping. As discussed in sections 2.1 and 3.3.2 and expected in literature, also hysteretic and to a lesser extend radiational damping might play an important role in the total damping contribution. Exactly what types of damping are present in soil-pile interaction is not known, but non-linear soil reactions most likely play an important role.

Another reason might be the simplistic constant distributed dashpot value that is applied for all depths in this model. Like the distributed spring stiffness to which it is linked, this is quite a rigorous simplification of reality. The stiffness should increase with depth.

Also the three-dimensional effect of displaced soil causing consolidation (and increased stiffness and possibly damping)) of surrounding soil in all directions is not taken into account in this way.

### **Combined effect**

As explained in this section, the different damping influences (dashpots) in the model have been tuned to correspond to that the damping that was measured.

This was done by considering them one by one and excluding the others while doing so. However, the combined damping effect of all the dashpots is not necessarily equal to the sum of the individual dashpots. For instance, it can be understood that the damping force induced by the hydrodynamic damping reduces the amplitudes in the lower part of the structure, resulting in less damping generation of the soil dashpots.

In order to match the total measured damping, this diminishing effect was compensated with the use of the top dashpot,  $C_{top}$  which has less effect on other dashpots because of its isolated position. This dashpot was tuned to generate 10 % log. decr. instead of the initial 2 % for the sloshing damper. 10% damping effect of the sloshing damper in combination with the applied values for the other damping influences, gave the same total damping for the two main frequencies as was identified from the measurements. This increase of the effect of the sloshing damper is, at least partly, justified by the fact that it is unknown what kind of damping effect the sloshing damper has during rotor-stop associated motions. This effect could be substantial.

#### 4.2.2 Software

A combination of Maple and MATLAB was used to implement the given analytical description of the model.

Maple is useful for symbolically deriving the coefficient matrix which can then be used in MATLAB to numerically solve the frequency equation, plot and check the normal mode shapes and calculating the frequency responses of the modeled system.

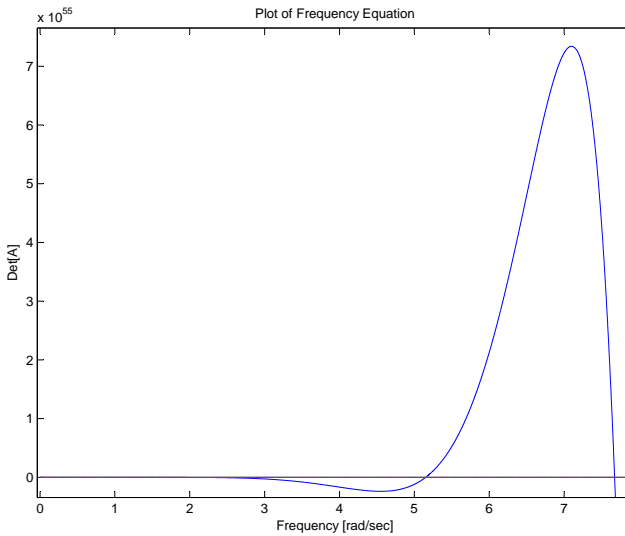
### 4.3 Model Results

#### 4.3.1 Frequency Equation

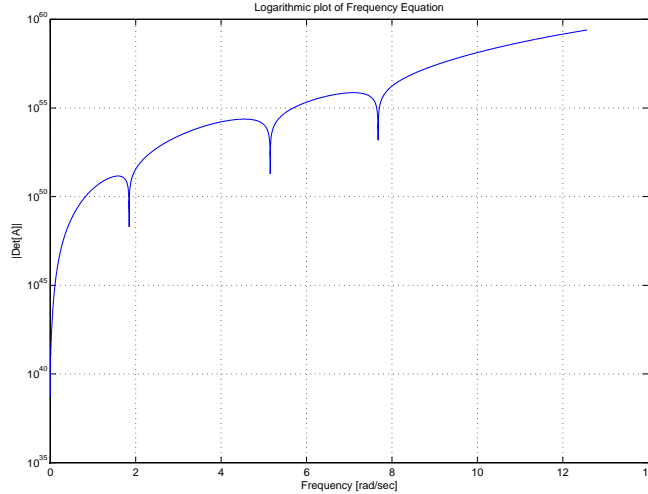
The frequency equation is solved for the undamped system for frequencies up to 2 Hz. The modal shapes, are found with these undamped modal frequencies found with the frequency equation (eq. 4.62).

Figure 4.2 depicts a plot of the solved frequency equation to give an idea of its exponential oscillations. The zero-crossings are the resonant frequencies.

Because of these exponential increasing peaks, lower zero-crossings can't be seen. That is why also a logarithmic plot of the absolute value of the frequency equation is plotted in figure 4.3, showing also higher resonant frequencies. The model frequencies are solved in radians/sec, so this unit is used for the horizontal frequency axis. Hertz (Hz) is a factor  $2\pi$  smaller than radians/sec.



**Figure 4.2:** Plot of the frequency equation solved for the frequencies of interest. The first three zero-crossings are the three frequencies of the first three modal shapes.



**Figure 4.3:** Logarithmic plot of the absolute value frequency equation solved for the frequencies of interest. The first three frequency peaks can be clearly seen.

### 4.3.2 Modal Shapes

This section depicts the undamped normalized modal shapes. The normalization is done with respect to the deflection at the top of the structure. Figures 4.4 to 4.8 depict respectively

1. the first natural bending modeshape at 1.84 rad/sec = 0.29 Hz
2. the modeshape associated with the blades at 5.15 rad/sec = 0.82 Hz
3. a comparison plot of these two latter modes
4. the second bending modeshape (which is thus the third frequency of the system) at 7.67 rad/sec = 1.22 Hz
5. the third bending modeshape (fourth frequency of the system) at 18.49 rad/sec = 2.94 Hz

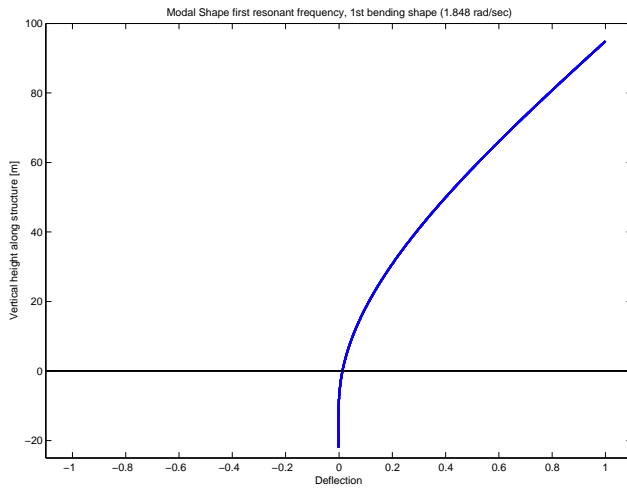


**Figure 4.4:** The modal shape corresponding to the first natural bending frequency.

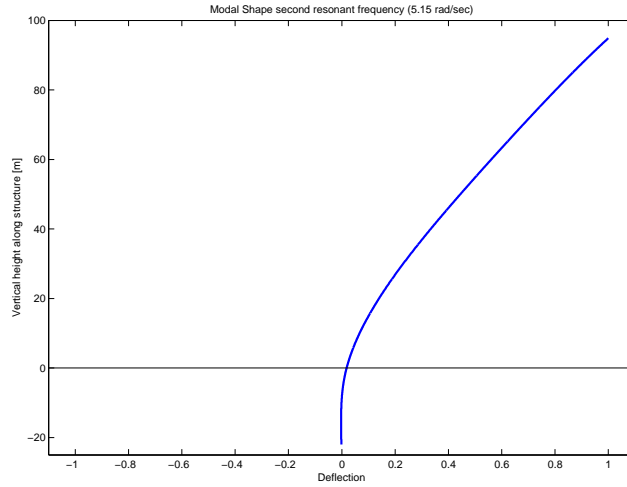


**Figure 4.5:** The modal shape corresponding to the second resonant (blade) frequency.

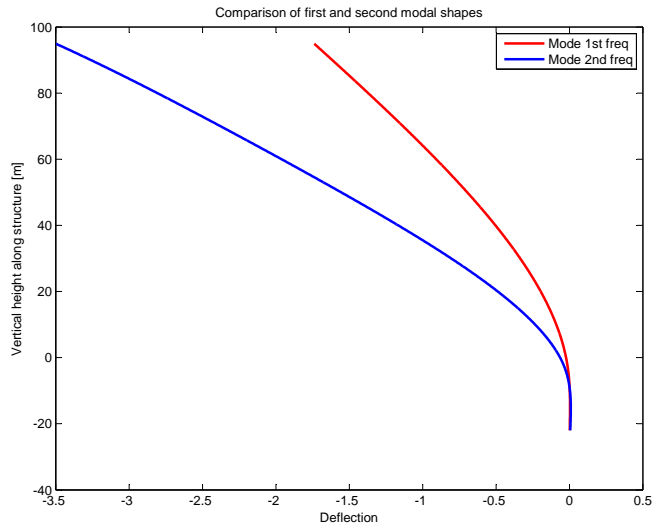


**Figure 4.6:** A comparison of the unnormalized modal shapes of the first bending mode and the second resonant (blade) mode.

The modeshapes of the first two first frequencies look very similar on first glance, that is why a non-normalized comparison plot is given in figure 4.6. In this comparison plot it can be seen that the blade mode does comprise more deflection-dominance at the top of the structure than the first bending mode.

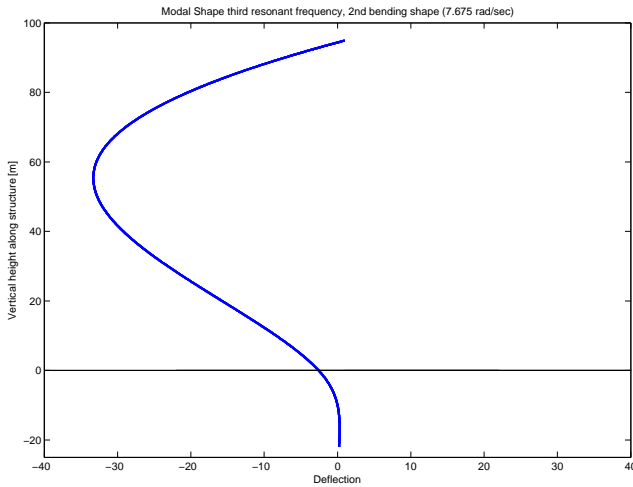


Figure 4.7: The modal shape corresponding to the second natural bending frequency.

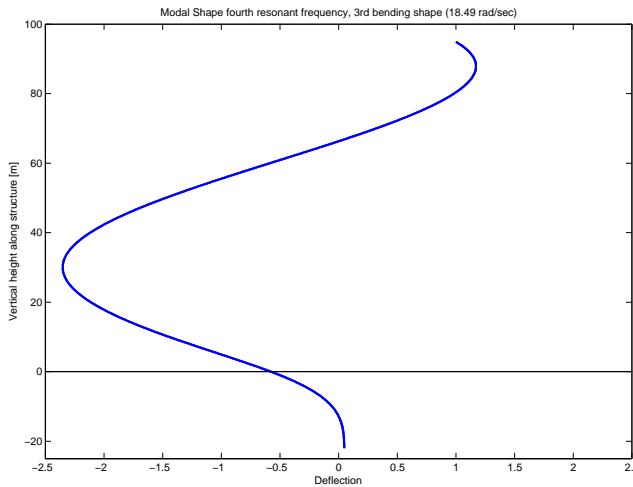
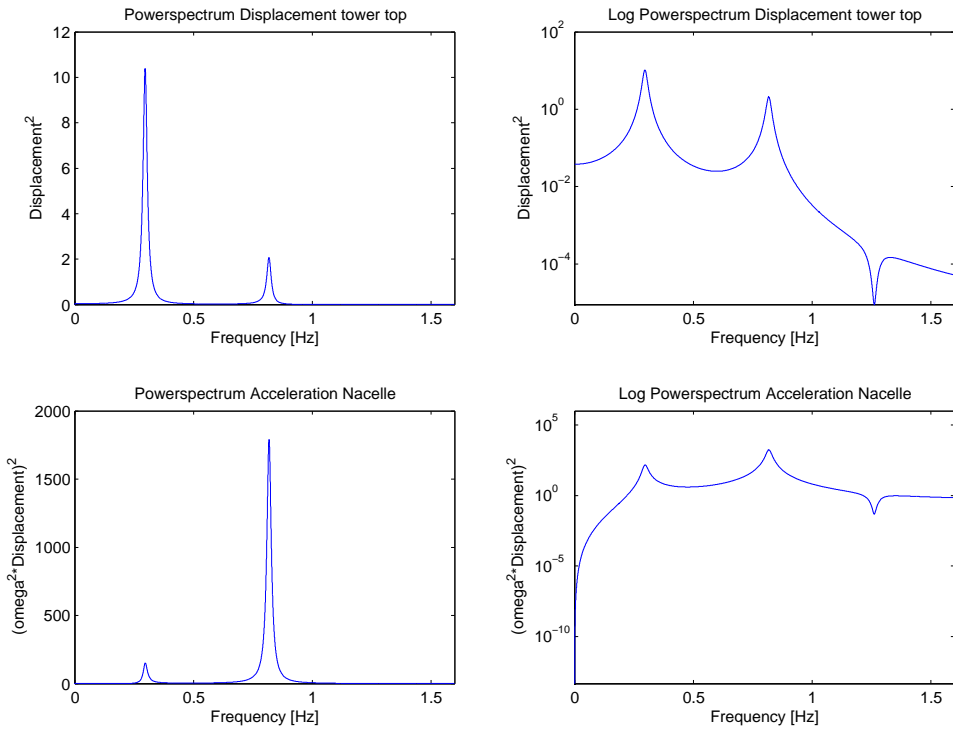


Figure 4.8: The modal shape corresponding to the third natural bending frequency.

### 4.3.3 Power Spectra

This section depicts the obtained power spectra of the model. The locations for the acceleration, bending moment tower top and bending moment tower bottom are the same as in the tests (see figure 3.2). These power spectra are the responses to the initial velocity  $V_0$  that was previously described. The displacement spectrum is found by solving equations 4.59 to 4.61 for each frequency of interest. Along the y-axis of the other spectra, the way of finding the depicted physical quantity related to the displacement is printed.



**Figure 4.9:** Power spectra for the displacement of the tower top and the acceleration of the nacelle.

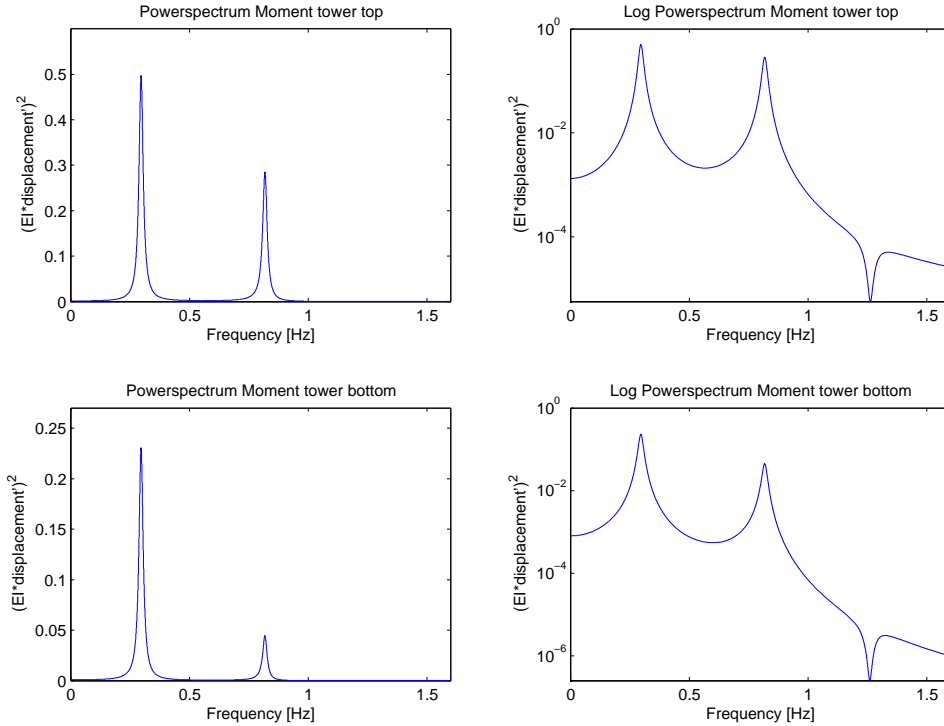


**Figure 4.10:** Power spectra for the bending moment at the tower top and bottom.

Both frequencies have the same value and are damped with the same magnitude as in the measurements.

The figures show that the second frequency corresponding to the blades has more energy in the accelerations of the nacelle, and the difference in its energy between the moment at the tower top and at the bottom indicates the pattern of a localised mode at the top.

In the logarithmic plots, the third (anti-resonant) peak corresponding to the second bending mode of the beam can be seen at 1.26 Hz.

In figures 4.11 and 4.12 the powerspectra of the morning tests are depicted again for comparison reasons. The torque is left out, as this was not modeled in the 1-dimensional model.

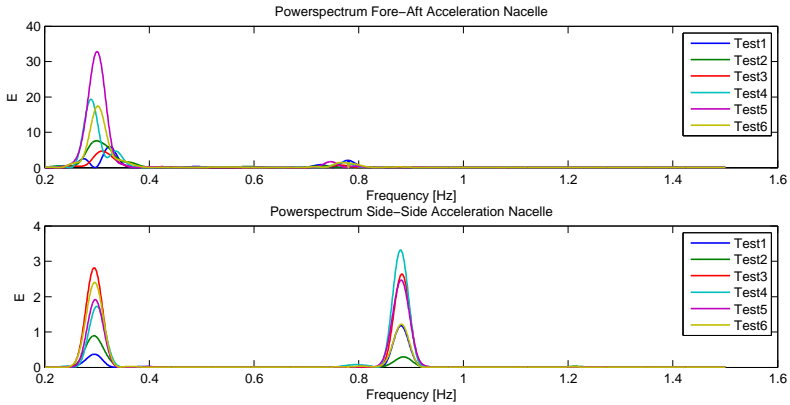


**Figure 4.11:** Power spectra of nacelle accelerations of the six morning tests.

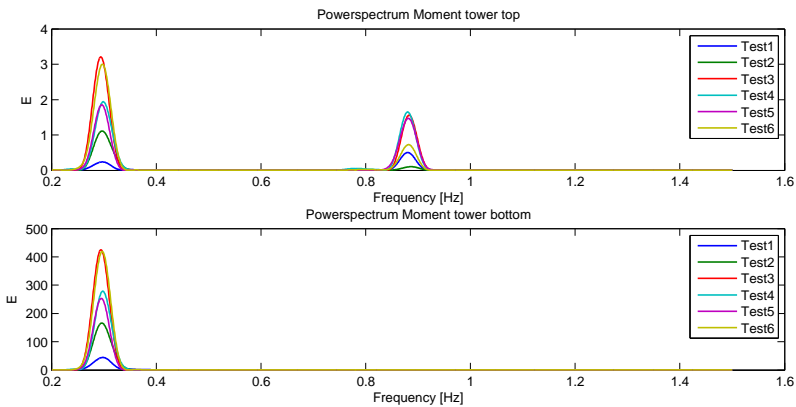


**Figure 4.12:** Power spectra of the bending moments along the tower of the six morning tests.

The correspondance is considered satisfactory. The bending moments at tower top and bottom of the model show similar patterns as in the measurements. The fact that the modeled second resonant blade frequency in the bending moment at the tower bottom is relatively more present than in the measurements, could be due to the fact that the extra stiffness of the grouted connection was not sufficiently incorporated. This extra stiffness could cause the motions in the tower bottom to further diminish.

Also a deviance between the modeled and measured signal is seen in the response of the fore-aft acceleration of the nacelle: the modeled signal indicates more energy in the blade frequency than the first natural bending frequency, while the measured signal shows the reverse of this. This could be reasoned by the fact that the auxiliary rotor mass was given an initial velocity,  $V_0$ . This is a simplistic way of modeling the rotor stop, and it may be clear that this is not physical. In this way, relatively more energy is put in the auxiliary system (as can be seen in figure 4.9) than in the bending of the entire system. An initial displacement of the top mass in the model might result in a better resemblance of the powerspectrum of the measurements.

#### 4.3.4 Timedomain comparison

The acquired frequency response can be inversely Fourier transformed to the time domain. The modeled time series can then be compared with the measured time series. This is done in figures 4.13 and 4.14, in which a comparison plot of the measured (test 1) and modeled signal of the bending moment at tower top and respectively at tower bottom are depicted. Note that this is a comparison of a modeled signal based on averaged values of all tests with a signal of only one test.

It can be seen that the attenuation rate of the two plotted signals in figure 4.13 is roughly the same. Both the measured and modeled signal at the tower top are dominated by the first two frequencies. The measured signal in this case clearly shows an other excitation/disturbance after Time=45 sec: the mean value of the oscillations is shifted downwards.

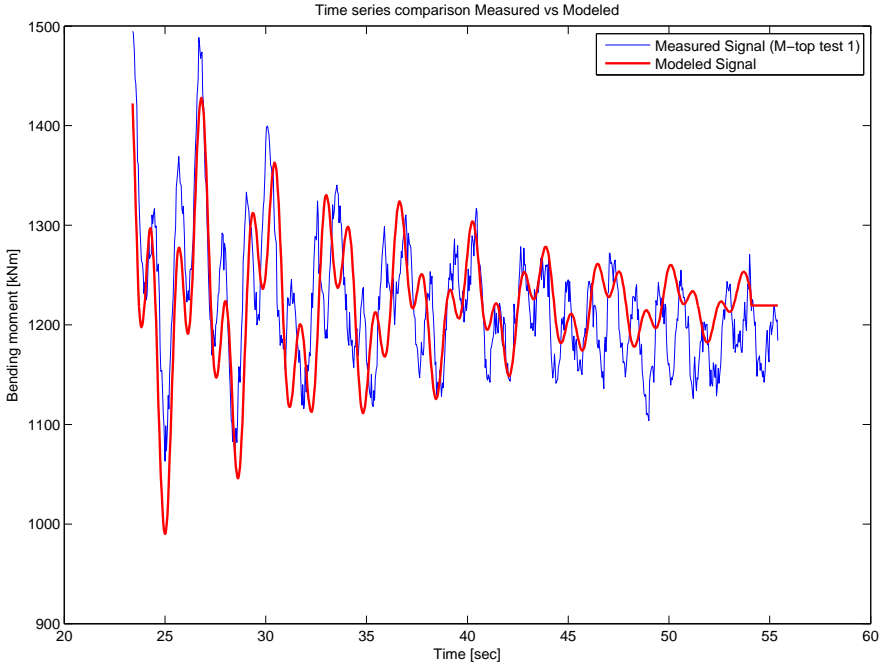


**Figure 4.13:** A comparison plot of the modeled signal (red) and the measured signal (blue) which is in this case the bending moment at the tower top of test 1.

Also the attenuation rate of the modeled signal of the bending moment at tower bottom is similar to that of the measured signal during test 1, although maybe the first two oscillations of the modeled signal have a somewhat higher damping pattern than the measured signal. The second frequency, although less than at tower top, is more present in the modeled signal as in the measured signal. This is also confirmed by the power spectra of these signals: in the power spectra of the measured signals at the tower bottom, no second frequency peak is present. In the modeled power spectrum of this location, still a small peak is to be seen. So the model does not entirely successfully model the localisation of the blade frequency at tower top. Again, the measured signal shows a disturbance after Time=45 sec: the mean value of the oscillations is shifted upwards.

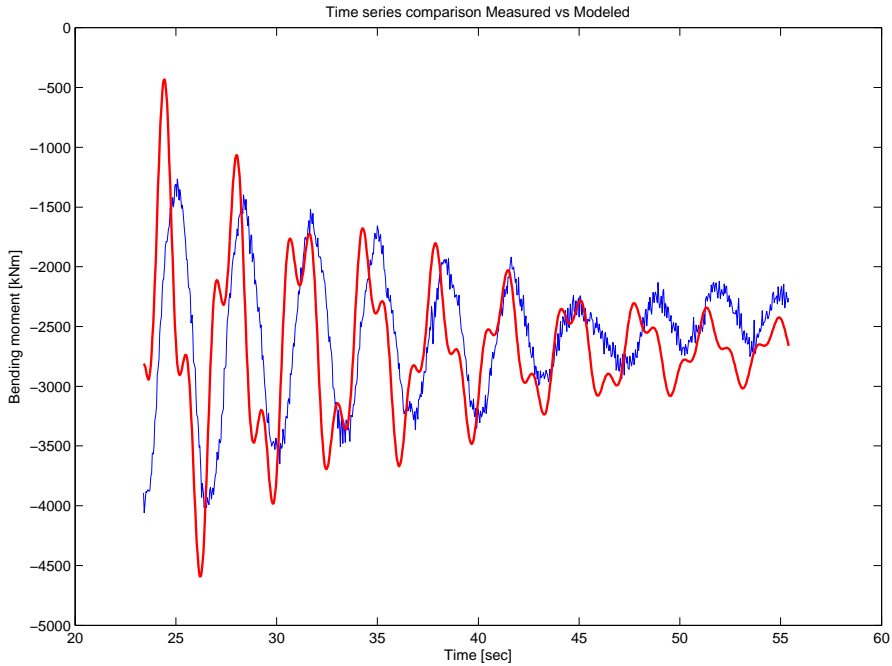


**Figure 4.14:** A comparison plot of the modeled signal (red) and the measured signal (blue) which is in this case the bending moment at the tower bottom of test 1.

## 4.4 Summary & Discussion

Again, in this section some paragraphs are devoted to summarize the material reported in this chapter, afterwhich a more in depth analysis on the acquired information is given in the discussion-paragraphs.

### 4.4.1 Summary

In this chapter a simplistic continuous model has been derived, incorporating enough aspects of the real BB16 structure to be able to model its behaviour up

to an extent that is sufficient for the objective of this research.

The parameters and their values have been discussed, and limitations of the model were reported.

The model output, in the form of modal shapes and power spectra with frequencies and damping values that correspond to the measurements, is considered satisfactory. The model exhibits the same behavior as BB16, in the way that it renders a second resonant frequency corresponding to a mode giving more deflections in the top of the structure.

A comparison of the modeled signal with that of a measured signal in the time domain revealed generally similar attenuation patterns.

As every model, implicit in its definition, some features and parameter values are debatable.

#### 4.4.2 Discussion

The dominant questions arise in modeling the soil. This is not surprising seen the focus of this study and the fact that literature confirms the complex nature of soil-pile interaction which make it challenging to model.

An interacting relation exists between the soil stiffness, modeled with  $k_s$  and  $k_t$ , and the generated soil damping potential. The soil stiffness has a large influence on the natural frequencies of the system, and it is found that the soil should be modeled quite stiff to reach the real frequencies of the measured signals. This fact has also already been indicated in previous work on soil-pile interaction by P. Wegener, whose findings have been incorporated in the model of this thesis. Modeling the soil too stiff, limits the potential of the dashpots to generate enough damping because of the lower resulting amplitudes. This is also a 'real-life' interaction phenomenon: if a pile is limited in its oscillation amplitudes in the soil because of a very large soil-stiffness, less damping can be generated.

The measured frequencies and their corresponding damping are a given and form the benchmark. The soil stiffness is modeled having an upper boundary Young's modulus of 130 MPa for saturated sand. This Young's modulus could be even on the low side, considering the 12.5 m seawater column above mudline

inducing extra pressure on the soil.

As previously stated, the Young's modulus is not further increased, as the potential of damping generation (the possible work done by the dashpots) is limited. To be able to match the expected measured soil damping, the distributed dashpots are given a value of a factor  $3.9 * 10^{-2}$  of the distributed stiffness  $k_s$ . This is already a factor which is quite a bit higher than the expected relation between these two soil parameters.

Modeling the soil damping as was done in the simplistic way proves to be limiting.

The limitations of the model might be found in the simplistic constant distributed dashpot value that is applied for all depths in this model. Like the distributed spring stiffness to which it is linked, this is quite a rigorous simplification of reality. The stiffness should increase with depth. This allows for relatively larger displacements at mudline.

Another limitation is the fact that the three-dimensional effect of displaced soil, causing consolidation of surrounding soil in all directions, which is not taken into account in this one dimensional model.

Lastly and maybe the most important improvement to the model, would be the inclusion of other types of damping in the model. As discussed in section 2.1 and expected in literature, also hysteretic and to a lesser extent radiational damping might play an important role in the total damping contribution. Exactly what types of damping are present in soil-pile interaction is not known, but non-linear soil reactions, and thus non-linear damping mechanisms, most likely play an important role.

# 5

## Conclusions and Recommendations

*This chapter seeks to draw the main conclusions from this research, but also gives a discussion on these conclusions. Recommendations are given in the last section of this report.*

### 5.1 Conclusions

The objective of this thesis as it is stated in the first chapter is:

***The estimation of the vibration decrement of an offshore wind turbine support structure, caused by its interaction with soil.***

1. The estimation of the vibration decrement caused by equivalent linear viscous damping generated by soil-pile interaction of the 'BB16' test turbine support structure lies in the range of 9.5 % logarithmic decrement, which equals 1.5 % ratio of critical damping of the first bending mode. The order of magnitude for this value applied in the offshore wind industry

today lies in the region of 0.44 % log. decr. (0.07 % ratio) for this first natural frequency.

2. Considering the fact that the average magnitude of the total identified damping in the measurements of the 'BB16' OWT is
  - 19 % logarithmic decrement (3 % ratio of critical) for the first natural bending frequency of 0.296
  - 9.5 % log. decr. (1.5 % ratio) for the second main present frequency of 0.825 Hz

it is concluded that, compared to the design value for BB16 of 2.5 % log. decr. (0.4 % ratio) of damping for the first natural frequency, the identified value in the measurements is relatively high.

3. Besides linear viscous damping, non-linear soil reactions and damping mechanisms are expected to play an important role in soil-pile interaction.
4. In this thesis, a tool has been developed to simplistically assess the influence of soil on the damping of an OWT. A difference in displacement in the soil profile between the vibrations of two different frequencies allows for identifying the influence of soil on these vibrations.

The mode shapes that correspond to the first and second measured frequencies have been identified via a combination of analyses of power spectra of signals at different measurement locations, the development of an analytical model, and a confirmation with the Siemens-design model BHawC. A difference in displacements of these mode shapes in the soil profile and a difference in damping of the vibrations of these two modes was identified. This allowed for assessing the influence of the structure's interaction with soil on the total damping of the structure. The second frequency in the signal is associated with a localized mode in the top of the structure caused by the closely spaced natural modal frequencies of the blades. The amplitudes in the soil profile of this modal shape are smaller than those of the first bending mode shape. Because of the varying amplitudes of the vibrations of these two modes in the soil profile, the difference in identified damping is attributed to the difference in possible influence that the soil can have on this damping.

Caution should be taken in generalizing the above stated order of magnitude

for the damping caused by soil-pile interaction. Generalization of the results of this research is limited by some factors of which some are discussed here.

The research is based on 12 rotor stops on a specific turbine during one day. Except for changing soil conditions, also changing environmental conditions (in particular wind speed) have influence on the magnitude of damping. For instance, displacement dependent damping is expected to be active in the soil-pile interaction process, the initial amplitude of vibration after a rotor stop has an important influence on the experienced damping of the structure. In this respect, the damping associated with vibrations induced by a rotor stop, might not be representative for the damping experienced during most of the lifetime of the OWT: the damping occurring during vibrations while the turbine is in production.

Another factor limiting the general validity of the results can be the unknown effect of the sloshing damper on the damping of vibrations after a rotor stop. A part of the identified difference in damping between the two dominant modes can possibly be attributed to a difference in sloshing damping influence on the vibrations of these modes. Lastly, it should be noted that the amplitudes of vibration after a rotor stop are relatively large compared to those occurring during production time of the turbine. As the experienced damping might be proportional to these amplitudes, the presented values can not directly stated to be representable for the situation in which the turbine is in production.

## 5.2 Recommendations

This MSc thesis is considered as a first step on a longer trajectory to reach the objective of

*The ability to predict the amount of damping an offshore wind turbine support structure will receive of a certain type of soil present at a certain location.*

Here some suggestions are given as possible next steps.

- Other active OWTs are currently equipped with similar PLM set-ups as was used for this thesis. The same tests and analyses can be performed with these turbines. This research yielded a tool for assessing the influence of soil on the damping of an OWT, which might be used on other OWTs. Comparing results is expected to yield interesting information. Whether comparable soil and pile combinations give comparable results as found in this research, and the effect of different soil profiles might be assessed.

Besides these PLM setups, all nacelles are nowadays equipped with so called 'G-sensors'. These are a type of accelerometer with a non-fixed sampling frequency. If the data of these sensors are found to be usable, a very large array of test turbines lies within grasp.

- Further analyses of the acquired data of the performed tests is a low threshold first action. A different approach might be interesting. Data analysis techniques like the Wavelet Transform and Cross Correlation can be used to see if it is possible to measure (wave-) energy transmittal throughout different parts of the structure in the transient region of the signal. The analysis of soil-reflected waves back into the structure can generate insight in energy dissipation in the soil.

Also the model-based approach of this thesis can be enhanced by a more complete model, integrating other types of damping. The data can be analyzed with other damping identification techniques as a check upon the here presented values. Also techniques that are not limited to identify the equivalent viscous damping in the signal should be applied.

- More full scale offshore experiments are required to generate insight in the complex soil-pile interaction phenomena. These tests should be performed on monopile foundations, as the processes playing a role at these rigid large-diameter piles in offshore soil (saturated and pressured) are not comparable with those of slender piles which were the focus of previously performed research. Both stiffness (updated p-y curves) as damping assessments should be performed. To this end, it is recommended to also measure the soil's reaction with, for instance, the use of accelerometers installed at mudline. Appendix F and figure F.2 elaborate more on possible measurement set-ups.
- In combination with these full scale experiments, a proper soil-pile interaction model should be developed incorporating as many aspects as

possible.

It is suggested to define a PhD research project focused on the development of this model in combination with full scale offshore experiments.

With respect to the design of OWT support structures, this research has indicated that there is room for increasing the value of experienced damping. Doing so, will enable using less construction steel because of smaller diameters and wall thickness of the monopile. An other option can be to extend the lifetime beyond the currently applied 20 years. More research must indicate up to what extend the design damping value may be increased.

It could also be considered to adjust the conventional design of these uniform tubulars. If indeed the damping generated in the soil is so substantial, we could think of thickening the outer diameter of the monopile at mudline, or maybe welding flaps or wings on the outer skin to mobilize more soil. Obviously this in turn can be un-beneficial for other aspects as fatigue hotspots or transportation and installation procedures. However, knowledge on the damping effect of soil could motivate new designs for the support structures of offshore wind turbines.

# Appendices



# An Introduction to Damping in System Dynamics

'Panta Rhei' - 'Everything moves' as the Greek philosopher Heraclitus once said. This was already the case in Greek times and is still a fact today; every thing - cars, houses, people, offshore wind turbine constructions - can obtain a certain dynamic movement. Structures or objects can vibrate or oscillate in a cyclic way in which they return to a certain position with an interval time which is called the *period* ( $T$ ) of that vibration. The magnitude of these oscillations is called the *amplitude* ( $A$ ).

Fortunately systems in the real world do not vibrate for ever (which could be quite destructive in many cases), because they lose their dynamic energy to their environment. This dissipation of energy is called *damping*. The amplitude of a dynamic vibration becomes smaller with each period, the vibration is damped until the equilibrium position is reached. In the displacement-time plot given in figure A.2 one can see a typical *decay* of the amplitudes (the peaks of this sinusoidal curve) of the displacement over each period  $T$ .

**Basic features of a Single Degree of Freedom System** The simplest model

for simulating the vibrations of a system is a *Single Degree of Freedom* model (SDOF). A schematic view of a SDOF is given in figure A.1. The block with mass  $m$  is excited by an external time-varying force  $f(t)$ . The displacement in  $u$ -direction  $u(t)$  is counteracted by the spring restoring force caused by the spring which has spring coefficient  $k$  in [N/m]. The spring force always acts in the opposite direction of the displacement of the mass. As stated before, this system eventually stops vibrating (in the case the external force is removed) because of the damping caused by the dashpot. The dashpot has a damping coefficient  $c$ , having dimension  $[\frac{N}{m/s}]$ , creating a counter force in the opposite direction of the *velocity* of the mass. The above textual description of the situation can be

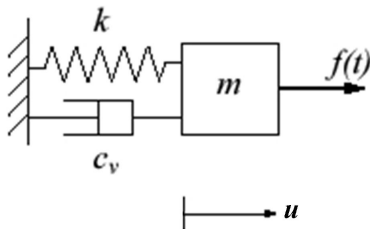


**Figure A.1:** Single Degree of Freedom model

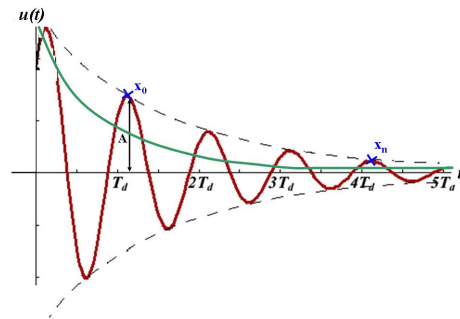


**Figure A.2:** Typical displacement-time relation of an underdamped (red) and a super-critically damped (green) system after an initial excitation

mathematically described with an *equation of motion* (EOM) which results from Newton's second law  $F=ma$ . The EOM for this example with a mass, a spring stiffness, damping and a time dependent forcing has the form

$$m\ddot{u} + c\dot{u} + ku = f(t) \quad (\text{A.1})$$

The mass will oscillate with a certain *frequency* ' $f$ ' in [Hz], which is the amount of oscillations it makes in 1 second, so  $f = \frac{1}{T}$ . In Dynamics usually the *angular frequency* ' $\omega$ ' is used which states the amount of *radians* per second:  $\omega = \frac{2\pi}{T}$ .

A dynamic system can be characterised by a couple of parameters. For instance: every object has its own *natural frequency*,  $\omega_0$ , which is the frequency with which the object will vibrate if it is given only an initial excitation (free vibration without influence of external forces) In this case the natural frequency can be computed by

$$\omega_0 = \sqrt{\frac{k}{m}} \quad (\text{A.2})$$

If a system is excited at this frequency, it will resonate: it will oscillate with larger amplitudes than at other frequencies. Figure A.3 shows the amplification factors of the amplitude according to the ratio of the exciting frequency  $\omega$  and the natural frequency  $\omega_0$ .

What is also of interest is how the system is damped. There are numerous ways of quantifying damping. One way is by stating the damping factor  $n$  [27]:

$$\frac{c}{m} = 2n \quad (\text{A.3})$$

The general solution of the homogeneous version of A.1 (the right-hand side of the equation equals zero, so without external force) can be found in the form of

$$u(t) = \sum_{k=1}^2 U_k e^{s_k t} \quad (\text{A.4})$$

with  $U_k$  and  $s_k$  the complex amplitude and eigenvalues respectively. When inserting this general solution in the EOM of A.1, dividing by  $U_k \exp(s_k t)$  and  $m$ , and incorporating the expressions of A.2 and A.3, one obtains the *characteristic equation*

$$s^2 + 2ns + \omega_0^2 = 0 \quad (\text{A.5})$$

As stated before,  $s_1$  and  $s_2$  are the eigenvalues of the system which can then be computed by

$$s_1 = -n + \sqrt{n^2 - \omega_n^2} \quad \text{and} \quad s_2 = -n - \sqrt{n^2 - \omega_n^2} \quad (\text{A.6})$$

Eigenvalues give important information about the *stability* of a system. A system is unstable if the real part of the (possibly complex) eigenvalues are positive.

The more specific solution of the homogeneous EOM with damping of an under-damped (explained further on) SDOF in free motion is

$$u(t) = e^{-nt}(A\cos(\omega_d t) + B\sin(\omega_d t)) = A_0 e^{-nt} \cos(\omega_d t - \varphi) \quad (\text{A.7})$$

where the amplitudes A and B or  $A_0$  can be found by incorporating the initial conditions  $u_0$  - the initial displacement and  $\dot{u}_0$  - the initial velocity. In A.7  $\varphi$  is the phase angle which (when multiplied by the damped angular frequency of the system  $\omega_d$ ) is the timelag that the system lags behind the exciting force. This phase difference is caused by the damping.

Note that in dynamics the following goniometric relation is frequently used:

$$e^{i\omega t} = \cos(\omega t) + i\sin(\omega t) \quad (\text{A.8})$$

which is called ‘*Euler’s Formula*’, after Leonhard Euler who first published this relation in 1748.

The reason why the form of equation A.4 is sought for as a possible solution is connected to this relation; the solution must be some form of a goniometric function.

Now elaborating more on damping, some more expressions will be introduced. A system is said to be *critically damped* when the free motion does not oscillate: the mass of the object does not pass its equilibrium point. From an initial displacement, it moves towards its equilibrium point without passing by that point. Schematically the decay of a critically damped motion is given by the green line in figure A.2. The value of the damping coefficient of a critically damped system is

$$c_{crit} = 2\sqrt{km} = 2m\omega_0 \quad (\text{A.9})$$

The damping in a system is usually quantified with the *damping ratio* which in literature is commonly denoted by  $\zeta$ . The damping ratio of a system is the ratio between the occurring damping coefficient  $c$  and the critical damping of that system. So in formula form:

$$\zeta = \frac{c}{2\sqrt{km}} = \frac{c}{2m\omega_0} \quad (\text{A.10})$$

If a system has a damping ratio of  $\zeta < 1$ , it is said to be *under or sub-critically damped*. If  $\zeta = 1$ , it is critically damped (as explained in the definition of critical

damping), and when  $\zeta > 1$ , the system is super-critically damped. The influence of different values for the damping ratio on the amplitude amplification close to resonant-exciting frequency is given in figure A.3.

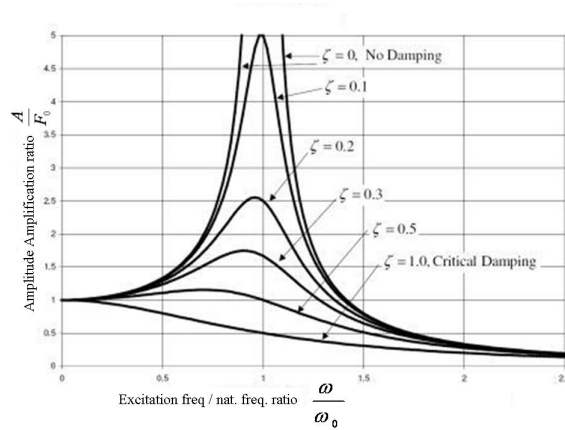


**Figure A.3:** The influence of damping ratio on the (amplitude) frequency response of a system.  $A/F_0$  is the amplitude amplification factor with  $A$  the amplitude of the response, and  $F_0$  the static induced displacement of the system.

As mentioned before, the presence of damping also influences the undisturbed natural frequency of the system, and thus causes the phase shift in the time domain in equation A.7. The relation between the undisturbed natural frequency and the damped frequency is as follows:

$$\omega_d = \omega_0 \sqrt{1 - \zeta^2} \quad (\text{A.11})$$

Here  $\omega_d$  is the *damped frequency* of the system.

Another way of quantifying damping in an under-damped system is by calculating the *logarithmic damping decrement* usually denoted as  $\delta$ . This is also a frequently used technique to determine the damping of a system from a measured response in the time domain. In figure A.2 the dotted line through the peaks of the curve is the exponential relation between these peaks. One takes the natural logarithm of the ratio of subsequent 'peaks' or amplitudes ( $x_0$  and  $x_n$  in the figure) and divides it over the amount of periods ' $n$ ':

$$\delta = \frac{1}{n} \ln \frac{x_0}{x_n} \quad (\text{A.12})$$

The relation between the damping *ratio* and the logarithmic damping *decrement* is as follows:

$$\zeta = \frac{1}{\sqrt{1 + \left(\frac{2\pi}{\delta}\right)^2}} \quad (\text{A.13})$$

Looking at this relation, one could say that as an approximation  $\zeta \approx \frac{\delta}{2\pi}$  if  $\delta \ll 4\pi^2$  which is usually the case for wind turbines.

# B

## Measuring Soil Damping

Models and resulting computations of damping ratios have to be validated by performing experiments. Besides validation, some in situ soil parameters in the model have to be found by measuring.

When interested in the damping during soil pile interaction, one can look into real-sized experiments where a pile is given an excitation and accelerometers at various locations are used to analyse the response of the pile, and possibly the response of the soil. Also laboratory test with models of the system on shaking tables or in centrifuges are a possibility for this objective.

This thesis comprises an experiment where the damping of a complete OWT is assessed. The description of this setup and the processing of the measurement data is treated in chapter 'Offshore Measurements'. In this section, various measuring techniques for pure dynamic properties of the soil only (so without a pile) are described. These techniques can be distinguished in laboratory test and in situ (real size, out in the field) experiments.

Laboratory tests tend to render lower damping values than in situ tests, but it might be questionable how realistic the perfect homogeneous soil samples and the confining pressures in laboratories are. On the other hand, severe inhomogeneities like a big rock in the soil can generate biased outcomes when measuring in situ. In both types of experiments, mostly the material damping

is measured. As can be understood from the previous paragraphs, this type of damping is more dependent on varying soil characteristics like shear strain and confining pressure which have to be measured. Because performing these type of (pure soil-) measurements is not within the scope of this thesis, the following section will only briefly describe the existing in situ and laboratory techniques without elaborating in too much detail.

## **B.1 In situ measurements**

Depending on exactly what parameter is of interest, various (non-/)invasive and (non-/)disturbing measurement setups exist.

For instance the Seismic reflection/refraction tests (echosounders or radars and at some distance a receiver), and Seismic cross-hole, down-hole and up-hole tests where a vibration source (e.g. an explosive) and a receiver at a certain distance are used to measure the velocity of P- and S-waves. The relative location of the vibrating source to the receiver make it either a cross-hole- (both are underground), up-hole- (explosive at soil surface) and down-hole- (explosive is underground, receiver at soil surface) test.

However, two techniques which can be more interesting for the scope of this research are the Seismic Cone Penetration test and the Spectral Analysis of Surface Waves-technique.

### **Seismic Cone Penetration Test (SCPT)**

A form of an invasive soil measurement is the Seismic Cone Penetration Test (SCPT). SCPT is used to determine the shear and pressure wave velocity and the material damping ratio variation with depth. Figure ?? shows the SCPT measurement set-up. [25]

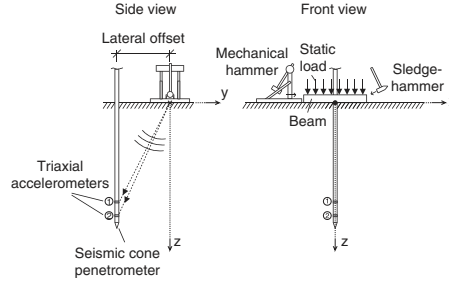


**Figure B.1:** Front and side view of SCPT measuring set-up

A beam on the soil surface is simultaneously hit on its side by a sledge hammer to induce the shear wave, and on its top by a mechanical hammer creating the pressure wave. The different arrival times of the waves at the two accelerometers in the down-hole cone enables us to compute the velocities of the different waves. Here the cross correlation technique has turned out to give good results. From a Fourier transform of the signal, a Spectral Ratio Slope (SRS) method can be used to determine the variation of material damping with depth. The SRS method is also based on the slope of the logarithmic ratio of consecutive amplitude peaks (from the two accelerometers). The method only measures material damping, not radiation damping. With this test, the material damping ratio  $\zeta_m$  can be computed by

$$\zeta_m = \frac{V_s}{2\pi} \left( \frac{\partial^2 \ln(x_1/x_2)}{\partial f \Delta z} \right) \quad (\text{B.1})$$

in which the part in brackets is the slope of the logarithmic ratio of two consecutive amplitude peaks in a selected frequency range.

### Spectral Analysis of Surface Waves (SASW)

In this setup wave measurements are performed to measure the shear wave velocity and the material damping.

These surface wave tests are a non-invasive seismic technique (as opposed to cone penetrating-techniques), using an array of accelerometers on the soil surface at some distance away from the wave-making source.

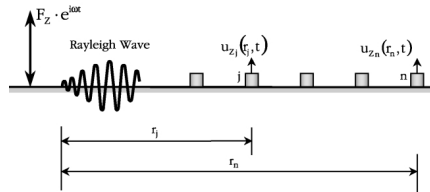


**Figure B.2:** SASW multi-station measurement set-up

With the Spectral Analysis of Surface Waves (SASW) method the measured signals are simultaneously turned into an attenuation and a dispersion curve with a displacement transfer function. These curves are then inverted to obtain the shear wave velocity and shear damping ratio using a newly developed algorithm [5] for the solution of the coupled Rayleigh eigenproblem in linear viscoelastic media. This method accounts for the relationship between the phase velocity and the damping of the seismic waves propagating in linear viscoelastic media as these are measured simultaneously from the same measurement setup and computed with the same displacement transfer function. This is unlike most other techniques where two measurements are performed; one for determining the shear wave velocity and one for the shear damping ratio.

## B.2 Laboratory experiments

Various laboratory tests have been developed to - among others - determine the material damping ratio of a homogeneous soil sample. The main ones are the Resonant Column test, the Free Torsion Pendulum, the Bender Element Test and the Cyclic Triaxial Test. The Free Torsion Pendulum is very similar to the Resonant Column Test and will thus not be separately discussed. These tests can be distinguished in low strain tests where the range of elastic soil reaction is simulated (the first three tests of the above mentioned), and experiments where the plastic range of soil reaction is considered for seismic earthquake engineering purposes (Cyclic Triaxial Test).

**Resonant Column test**

In the Resonant Column test procedure a cylindrical soil specimen is excited in its fundamental (eigen-) mode of vibration. This can be either a torsional or a longitudinal motion. From the resonance frequency and the subsequent amplitude decay after stopping the excitation, the wave velocities, strain amplitudes, shear modulus and damping ratio are calculated. Limitations of this test are that the calculation procedure is a back-calculation. The measured reaction is not the pure reaction of the soil, but rather of the system of soil sample plus apparatus.

**Bender Element Test**

In this test a cylindrical sample is equipped with a sender and a receiver element at its ends [22]. These elements can change its form and dimension because of electric pulses. This causes shear waves or compression waves to propagate through the sample. The arrival time is measured at the receiving element. This setup provides determination of the dynamic shear modulus and the dynamic elasticity modulus. The advantage of this setup is that the sample is subjected to minor disturbance.

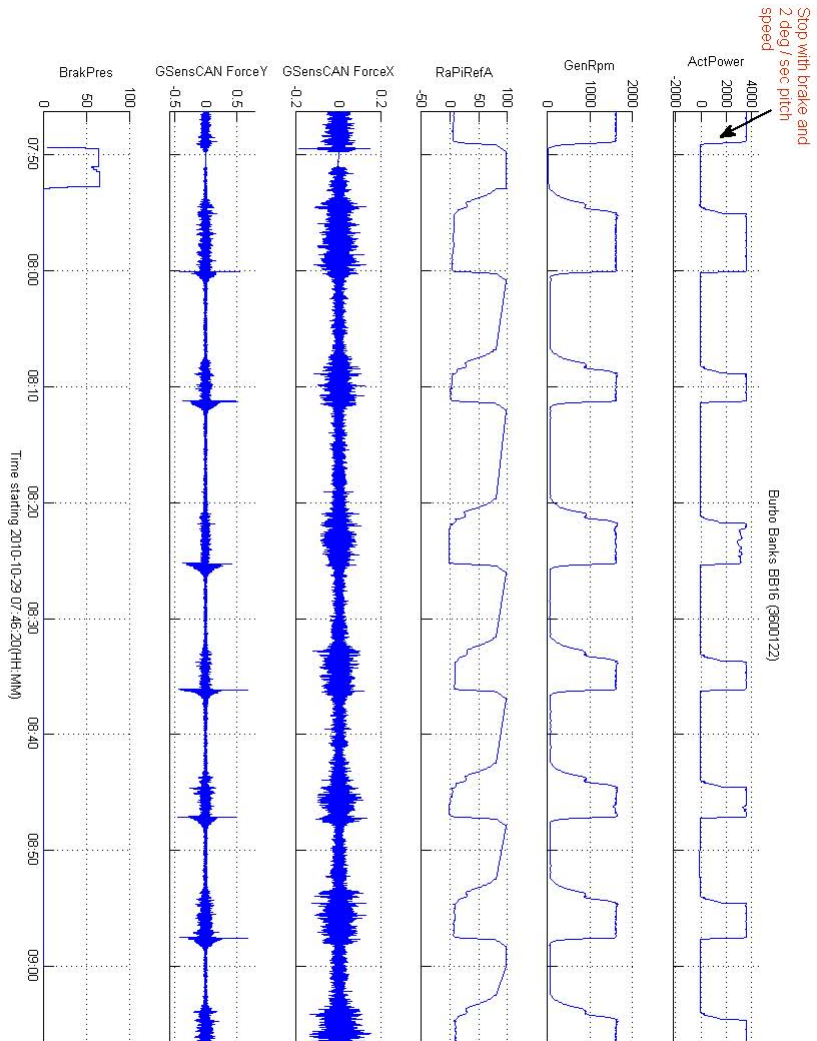
**Cyclic Triaxial Test**

This test setup is very similar to the soil Triaxial test, but extended with a cyclic loading element. It falls in the category of high strain tests to study the plastic liquefaction reaction of soil. Other similar cyclic tests are the Cyclic simple Shear test and the Cyclic torsional Shear test, which also focus on the plastic deformation of soil, usually for earthquake engineering purposes.

C

# BB16 Rotor Stop Measurement Specification Documents

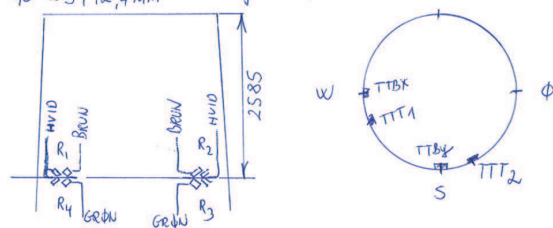
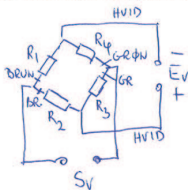
## C.1 Overview Morning Tests



**Figure C.1:** An overview of the rotor stop tests that were performed during the morning. Only stops without mechanical break were used for this research: a mechanical break applied at the end of a rotor stop induces extra undesired excitations to the decaying structure. From top to bottom the graphs depict the active power, the generator rotations per minute, the pitch angle of blade A, G-sensor force in x-direction, G-sensor force in y-direction and the mechanical break activity of the turbine.

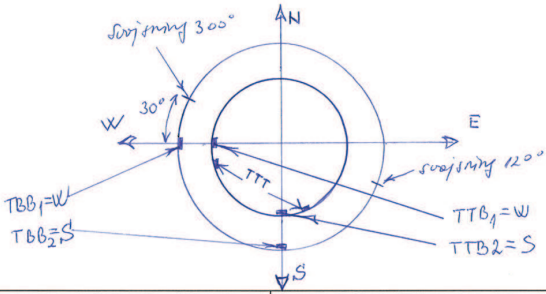
## C.2 Location and Orientation of Strain Gauges BB16

	<b>KVALITETS Skema</b>	QS 07.07 Rev. 2 SG installation
Af: S.O.L./B.W.	Dato: 01-12-1999	Side 1 af 1

Projekt: 3,6MW Burbo Banks	Dato: 17.06.2007	Init: HM	
Måle parameter: TTT	Arbejds sted: UK - Burbo		
Brottype: 4/4			
Strain gage type: 1-XY21-6/120	Lot. Nr. A345/M1		
Gage faktor: A+B/2,05 ± 1%	Gage modstand: 120 ± 0,35 Ohm	Shunt modstand: /	
Isolation: /			
Fysisk placering af strain gages (med fysisk afstand til reference punkt på møllen)			
<p> <math>R_1, R_4 \rightarrow R_2, R_3 = 90^\circ</math>  <math>90^\circ = 3992,4 \text{ mm}</math> </p> <p> <math>TTBX \rightarrow TTT_1 = 100 \text{ mm}</math>  <math>TTBY \rightarrow TTT_2 = 100 \text{ mm}</math> </p> 			
Dato: 17.06.2007	Init: HM		
Forstærker no. b-12-06-556	Hottinger nr. 13		
Kanal betegnelse: TKS CH: 8	Gain 1000		
Diagram for opkobling af bro:	E+ Excitation voltage plus E- Excitation voltage minus S+ signalspænding plus S- signalspænding minus		
	Farve	Klemme nr.	Betegnelse
	R1 HVID	HVID	E-
	R2 HVID	BRUN	E+
	R3 GRØN	GRØN	S-
	R4 GRØN	GUL	S+
		12,0,25	
Bemærkninger:			

**Figure C.2:** Location of used strain gauges at BB16 tower top. TTBX=strain gauge measuring bending moment x-axis. Idem for TTBY. TTT1 en TTT2 are the strain gauges for measuring the torque. Also see figure 3.2 for better understanding.

	<b>KVALITETS Skema</b>	QS 07.07 Rev. 2 SG installation
		Af: S.O.L. /B.W. Dato: 01-12-1999 Side 1 af 1

Projekt: <b>3,6MW Burbo Banks</b>		Dato: <i>20.06.2007</i>		Init: <b>HM</b>	
Måle parameter: <i>777</i>		Arbejds sted: <b>UK - Burbo</b>			
Brotpe: 4/4					
Strain gage type:		Lot. Nr.			
Gage faktor:	Gage modstand:	Shunt modstand:	Isolation:		
Fysisk placering af strain gages (med fysisk afstand til reference punkt på møllen)					
					
Dato:		Init:			
Forstærker no.		Hottinger nr.			
Kanal betegnelse:					
Diagram for opkobling af bro:		E+ Excitation voltage plus E- Excitation voltage minus S+ signalspænding plus S- signalspænding minus			
	Farve	Klemme nr.	Betegnelse		
			E-		
			E+		
			S-		
			S+		
Bemærkninger:					

**Figure C.3:** Location of used strain gauges at BB16 tower top. TTBX=strain gauge measuring bending moment x-axis. Idem for TTBY. Also see figure 3.2 for better understanding.

	<b>KVALITETS Skema</b>	QS 07.07 Rev. 2 SG installation
		Af: S.O.L./B.W.

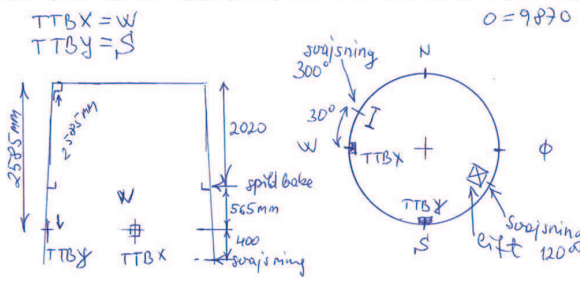
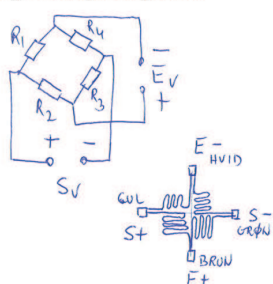
Projekt: 3,6MW Burbo Banks	Dato: 17-06-2007	Init: HM																		
Måle parameter: TTBX + TTBY	Arbejds sted: UK - Burbo																			
Brotype: 4/4																				
Strain gage type: 1XY11-6/120	Lot. Nr. A 383 / 32																			
Gage faktor: $2,04 \pm 1\%$	Gage modstand: $120 \pm 0,35 \Omega$	Shunt modstand: /																		
Isolation: 																				
Fysisk placering af strain gages (med fysisk afstand til reference punkt på møllen)																				
																				
Dato: 17-06-2007	Init: HM																			
Forstærker no. B-12-06-	Hottinger nr. 6																			
Kanal betegnelse: TK5	GAIN 1000																			
Diagram for opkobling af bro:	E+ Excitation voltage plus E- Excitation voltage minus S+ signalspænding plus S- signalspænding minus																			
	<table border="1"> <thead> <tr> <th>Farve</th> <th>Klemme nr.</th> <th>Betegnelse</th> </tr> </thead> <tbody> <tr> <td>HVID</td> <td>TTBX GRØN TTBY SØD</td> <td>E-</td> </tr> <tr> <td>BØVN</td> <td>TTBX RØD TTBY LILÅ</td> <td>E+</td> </tr> <tr> <td>GRØN</td> <td>TTBX BLÅ TTBY GRØN/120Ω</td> <td>S-</td> </tr> <tr> <td>GUL</td> <td>TTBX RØD TTBY BLÅ/120Ω</td> <td>S+</td> </tr> <tr> <td></td> <td>12X0,25</td> <td></td> </tr> </tbody> </table>	Farve	Klemme nr.	Betegnelse	HVID	TTBX GRØN TTBY SØD	E-	BØVN	TTBX RØD TTBY LILÅ	E+	GRØN	TTBX BLÅ TTBY GRØN/120Ω	S-	GUL	TTBX RØD TTBY BLÅ/120Ω	S+		12X0,25		
Farve	Klemme nr.	Betegnelse																		
HVID	TTBX GRØN TTBY SØD	E-																		
BØVN	TTBX RØD TTBY LILÅ	E+																		
GRØN	TTBX BLÅ TTBY GRØN/120Ω	S-																		
GUL	TTBX RØD TTBY BLÅ/120Ω	S+																		
	12X0,25																			
Bemærkninger: TK5 TTBX ch. 6 B-12-06-554 TK5 TTBY ch. 7 B-12-06-555																				

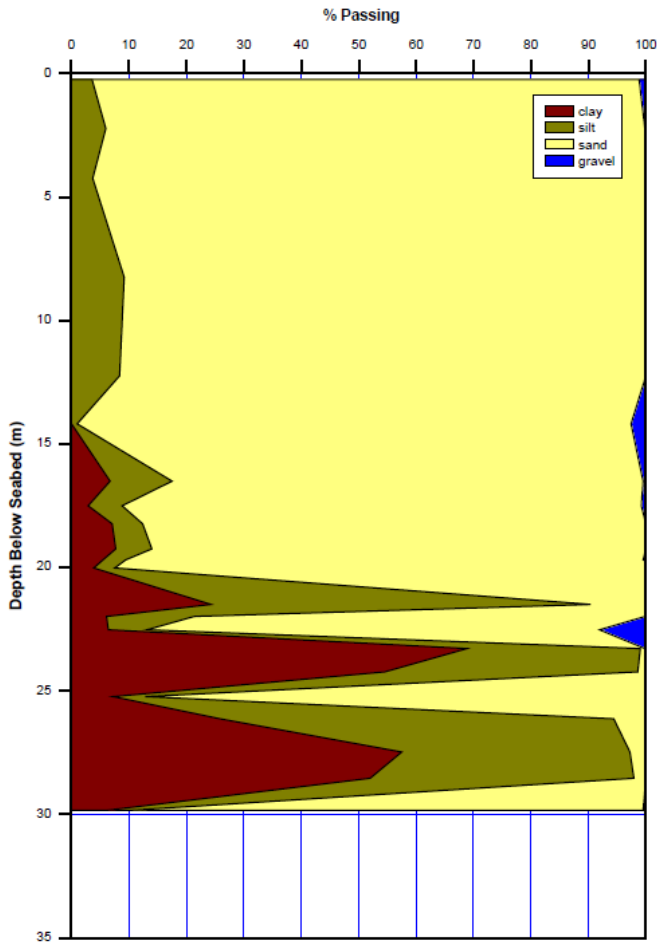
Figure C.4: Location of used strain gauges at BB16 tower top. TTBX=strain gauge measuring bending moment x-axis. Idem for TTBY. TTT1 en TTT2 are the strain gauges for measuring the torque. Also see figure 3.2 for better understanding.

	<b>KVALITETS Skema</b>	QS 07.07 Rev. 2 SG installation
	Af: S.O.L./B.W.	Dato: 01-12-1999

Projekt: 3,6MW Burbo Banks		Dato: 23.06.2007	Init: HM																
Måle parameter: TBBX-TBBY		Arbejds sted: UK - Burbo																	
Brottype: 4/4																			
Strain gage type: 1XYM-6/120		Lot. Nr. A 383 / 32																	
Gage faktor: 2,04 ± 1%	Gage modstand: 120 ± 0,35 Ohm	Shunt modstand: 	Isolation: 																
Fysisk placering af strain gages (med fysisk afstand til reference punkt på møllen)																			
Dato: 23.07.2007		Init: HM																	
Forstærker no. B-12-06-		Hottinger nr. 6																	
Kanal betegnelse:		GAIN 1000																	
Diagram for opkobling af bro:		E+ Excitation voltage plus																	
		E- Excitation voltage minus																	
		S+ signalspænding plus																	
		S- signalspænding minus																	
		<table border="1"> <thead> <tr> <th>Farve</th> <th>Klemme nr.</th> <th>Betegnelse</th> </tr> </thead> <tbody> <tr> <td>HVID</td> <td>TBBX GRØ TBBY GRØT</td> <td>E-</td> </tr> <tr> <td>BRUN</td> <td>TBBX RØD TBBY LIL</td> <td>E+</td> </tr> <tr> <td>GRØN</td> <td>TBBX BLÅ TBBY GRØN/BLÅ</td> <td>S-</td> </tr> <tr> <td>GUL</td> <td>TBBX RØ TBBY BLÅ/GRØ</td> <td>S+</td> </tr> <tr> <td></td> <td>12x0,25</td> <td></td> </tr> </tbody> </table>		Farve	Klemme nr.	Betegnelse	HVID	TBBX GRØ TBBY GRØT	E-	BRUN	TBBX RØD TBBY LIL	E+	GRØN	TBBX BLÅ TBBY GRØN/BLÅ	S-	GUL	TBBX RØ TBBY BLÅ/GRØ	S+	
Farve	Klemme nr.	Betegnelse																	
HVID	TBBX GRØ TBBY GRØT	E-																	
BRUN	TBBX RØD TBBY LIL	E+																	
GRØN	TBBX BLÅ TBBY GRØN/BLÅ	S-																	
GUL	TBBX RØ TBBY BLÅ/GRØ	S+																	
	12x0,25																		
<b>Bemærkninger:</b> $\phi = 15970 \text{ mm}$ $30^\circ = 1330,8 \text{ mm}$ $15970 \cdot 360 = 44,36 \text{ cm}$ $1^\circ = 44,36 \text{ cm}$ $90^\circ = 3992,4 \text{ mm}$ Ch 8 = PR 2261 = B-12-06-520 Ch 9 = PR 2261 = B-12-06-225																			

Figure C.5: Location of used strain gauges at BB16 tower bottom. Also see figure 3.2 for better understanding.

### C.3 Soil Profile at BB16 OWT



BURBO BANK OFFSHORE WIND FARM

Particle Size Distribution. Area Chart - T3

Figure C.6: The soil profile at in the region of BB16 OWT.

Turbine Location A6 (T18)

Coordinates WGS84 / UTM Zone 30 North  
W 486077.65 m  
N 5926607.57 m

Testing Completed to Depth  
BH 33.2 m  
PCPT

By: N Brown  
Checked: T Powell  
Approved:  
Date: 6/30/2005

Notes: Broken CPPT log i.e. several blanks areas in best record are indicated down the hole. Break in record at 24.8 m to 28.2 m due to airlocks.

Depth Below MSL (m)	Soil Description	General		Submerged Unit Weight		Internal Angle of Friction		Interface Friction Angle		Limiting Skin Friction (kPa)	Limiting Tip Resistance (MPa)	End Bearing Factor $N_c$
		Indicative End Tip Resistance $q_c$ (MPa)	Indicative Skin Friction $f_s$ (MPa)	Best Estimate (kN/m <sup>3</sup> )	Highest Expected (kN/m <sup>3</sup> )	Best Estimate (Deg)	Highest Expected (Deg)	Best Estimate (Deg)	Highest Expected (Deg)			
0		0.0	0.0									
0.25	SAND	0.2	0.01	7.26	8.25	25	30	20	25	67	67	2.9
0.75	SAND	0.7	0.04	7.26	8.25	25	30	20	25	67	67	2.9
1.25	SAND	1.2	0.07	7.26	8.25	25	30	20	25	67	67	2.9
1.75	SAND	1.7	0.09	7.26	8.25	25	30	20	25	67	67	2.9
2.25	SAND	2.2	0.12	7	8	29	30	24	25	67	67	2.9
2.75	SAND	2.2	0.12	10.5	11.5	37	40	32	35	114.8	114.8	12
3.25	SAND	2.5	0.12	10.5	11.5	37	40	32	35	114.8	114.8	12
3.75	SAND	1.8	0.12	10.5	11.5	37	40	32	35	114.8	114.8	12
4.25	SAND	1.8	0.12	10.5	11.5	37	40	32	35	114.8	114.8	12
4.75	SAND	25.0	0.01	8	10.5	35	38	30	33	95.7	95.7	8.6
5.25	SAND	20.0	0.07	9	10.5	35	38	30	33	95.7	95.7	8.6
5.75	SAND	20.0	0.07	10.5	11.5	37	40	32	35	114.8	114.8	12
6.25	SAND	24.4	0.17	10.5	11.5	37	40	32	35	114.8	114.8	12
6.75	SAND	24.4	0.17	10.5	11.5	37	40	32	35	114.8	114.8	12
7.25	SAND	24.4	0.17	10.5	11.5	37	40	32	35	114.8	114.8	12
7.75	SAND	24.4	0.14	10.5	11.5	37	40	32	35	114.8	114.8	12
8.25	SAND	24.4	0.14	10.5	11.5	37	40	32	35	114.8	114.8	12
8.75	SAND	22.2	0.14	10.5	11.5	37	40	32	35	114.8	114.8	12
9.25	SAND	22.2	0.14	10.5	11.5	37	40	32	35	114.8	114.8	12
9.75	SAND	22.2	0.14	10.5	11.5	37	40	32	35	114.8	114.8	12
10.25	SAND	22.2	0.14	10.5	11.5	37	40	32	35	114.8	114.8	12
10.75	SAND	22.2	0.14	10.5	11.5	37	40	32	35	114.8	114.8	12
11.25	SAND	22.2	0.14	10.5	11.5	37	40	32	35	114.8	114.8	12
11.75	SAND	22.2	0.14	10.5	11.5	37	40	32	35	114.8	114.8	12
12.25	SAND	22.2	0.12	10.5	11.5	37	40	32	35	114.8	114.8	12
12.75	SAND	22.2	0.12	10.5	11.5	37	40	32	35	114.8	114.8	12
13.25	SAND	22.2	0.12	10.5	11.5	37	40	32	35	114.8	114.8	12
13.75	SAND	22.2	0.12	10.5	11.5	37	40	32	35	114.8	114.8	12
14.25	SAND	22.2	0.12	10.5	11.5	37	40	32	35	114.8	114.8	12
14.75	SAND	22.2	0.12	10.5	11.5	37	40	32	35	114.8	114.8	12
15.25	SAND	22.2	0.12	10.5	11.5	37	40	32	35	114.8	114.8	12
15.75	SAND	22.2	0.12	10.5	11.5	37	40	32	35	114.8	114.8	12
16.25	SAND	3.3	0.12	7	8	29	30	24	25	67	67	2.9
16.75	SAND	3.3	0.12	7	8	29	30	24	25	67	67	2.9
17.25	SAND	3.3	0.12	7	8	29	30	24	25	67	67	2.9
17.75	SAND	3.3	0.12	7	8	29	30	24	25	67	67	2.9
18.25	SAND	17.2	0.12	9	10.5	35	38	30	33	95.7	95.7	8.6
18.75	SAND	17.2	0.12	9	10.5	35	38	30	33	95.7	95.7	8.6
19.25	SAND	17.2	0.12	9	10.5	35	38	30	33	95.7	95.7	8.6
19.75	SAND	17.2	0.12	9	10.5	35	38	30	33	95.7	95.7	8.6
20.25	SAND	17.2	0.12	9	10.5	35	38	30	33	95.7	95.7	8.6
20.75	SAND	17.2	0.12	9	10.5	35	38	30	33	95.7	95.7	8.6
21.25	CLAY	6.7	0.12	7.5	10.5	30	35	25	30	81.3	81.3	4.8
21.75	CLAY	10.0	0.17	8	10.5	30	35	25	30	81.3	81.3	4.8
22.25	CLAY	3.3	0.17	7.5	10.5	30	35	25	30	81.3	81.3	4.8
22.75	CLAY	3.3	0.17	7.5	10.5	30	35	25	30	81.3	81.3	4.8
23.25	CLAY	3.3	0.17	7.5	10.5	30	35	25	30	81.3	81.3	4.8

Figure C.7: Soil parameters at the BB16 (=A6) OWT.



# D

## The Fourier Transform and Signal Processing Basics

The total dynamic motions of a system are often a summation of (an infinite number of) different harmonics with different wavelengths and periods, different harmonics. So the sinusoidal time domain pattern is a summation of an infinite amount of different sinusoidals with each their own frequency. Usually, the lowest frequency governs the time domain pattern, and the 'higher harmonics' oscillate around or on top of that sinusoidal. An example of such a pattern is given in figure D.1.

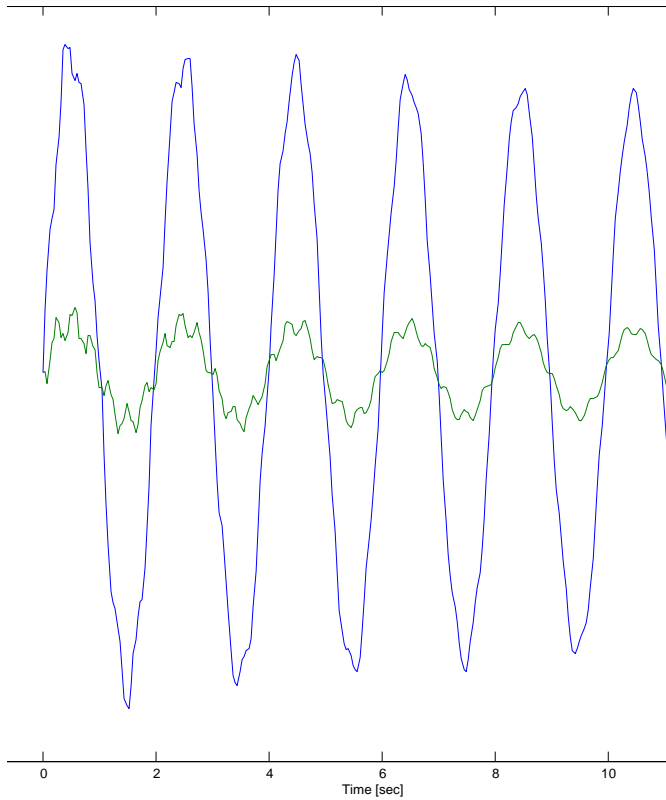


**Figure D.1:** A modeled signal of the horizontal motion of a beam at two different vertical locations along the beam. The bottom-clamped beam was given a horizontal excitation at its top, the blue signal is the motion of the higher location, the green signal is the horizontal motion of the lower location (and thus has lower amplitude). Six different modeshapes and frequencies were incorporated in this signal, and the above explained summation of sinusoidals can be clearly seen. We also see that the higher frequencies undergo more damping than the lower ones.

If one models a certain continuous signal  $f(t)$  one can perform a Continuous Fourier transform on it by

$$\hat{f}(\omega) = \int_{-\infty}^{+\infty} f(t) \cdot e^{-i\omega t} dt \tag{D.1}$$

Here we see that the original function is transformed from the time domain ( $t$ ) to the frequency domain ( $\omega$ ).

A way to display the result of this Fourier transform is to plot the power spectrum. A power spectrum shows how the energy of a system is distributed over the occurring frequencies in that signal. The spectrum is found by taking the square of the product of the Fourier transform. Figure D.2 gives a schematic overview of how the Fourier Transform decomposes a certain time signal into its frequencies and how each frequency has its own energy in the energy density spectrum, a form of a power spectrum. This figure is an example in which this is done for ocean waves.

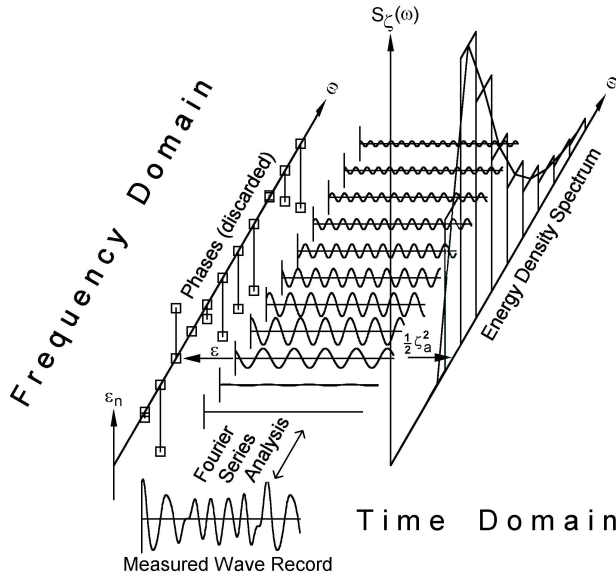


**Figure D.2:** Breaking up a wave record into its frequency components with their energy, and plotting this in a energy density spectrum.

However, in real-life measurements, recorded signals are never continuous, but discrete. A signal can only be recorded with a certain *sampling frequency*; the amount of recordings per second. This frequency can be very high, but of course never continuous. For that extend, we can also use the Discrete Fourier Transform (DFT). The algorithm is given by;

$$\hat{f}(\omega) = \sum_{n=1}^N f(n)e^{-\frac{2\pi i}{N}\omega n} \quad \text{with } \omega = 1, \dots, N \quad (\text{D.2})$$

$N$  is the amount of sampled points in the recorded vector of the signal in time. So  $N$  equals the time length divided by the sampling frequency. Small 'n' indicates the n-th index number in this vector.

### Hanning Window

Before any transform is applied, the set of data of interest should be selected from the raw data. Once this is done, the selected set can be multiplied with a *window function* to decrease *spectral leakage* and to suppress *noise*.

Noise in signal analyses refers to the low-amplitude and high frequency disturbance caused by the environment where and the equipment with which the measurements were performed.

Without going into the mathematical background, spectral leakage is the effect that energy of a frequency leaks or shifts towards other frequencies when applying a discrete Fourier transform on a finite signal towards a finite frequency spectrum. This has to do with the fact that the Fourier transform assumes an infinite periodic signal. This is in real life usually not the case: a finite time window of a signal is analyzed, of which the start of the window is not necessarily the same as the end (non-periodic), and the window length does usually not equal exactly an integer amount of cycles of the vibrations of each present frequency. Nevertheless, these conditions for successful transformation can be met by multiplying the finite time window of interest with a window function which forces the signal to be periodic within the time frame of interest. Most window functions result in zero valued beginning and end of the frame, and a

scaled value between 0 and 1 of the middle section of the time frame.

The *Hanning Window function* is a function with the shape of half a sinus; a wide lobe with sides moving towards zero. When multiplying this window with the selected set of data, the effect is that most of the important middle part of the signal is (almost) unaffected and the side-values turn to zero. If these values wouldn't be zero, the DFT would shift this 'initial' energy onto other frequencies. The frequency spectrum that is derived after a Hanning window is applied on the time-signal, is a 'clean' spectrum (without noise and spectral leakage) revealing only the main present frequencies with their peaks at the right frequency locations and with correct heights. However, multiplying the time response with this window, does have an influence on the width of the frequency peaks.

If the Hanning window is used to sample a signal in order to convert to the frequency domain, it is complex to reconvert to the time domain without adding distortions.

### **Aliasing, Nyquist Frequency and Folding**

The frequency bandwidth of a recorded signal that can be analyzed is limited by the frequency with which the signal is sampled,  $f_s$ .

If a signal is reproduced with a too low resolution (frequency), this reconstructed image will form an *Alias* of the original, real signal. An alias differs from the original signal.

The most famous example of this is the wagon-wheel effect; the spokes of the wheel seem to turn too slowly or even backwards. This is because our eyes or brain sample the spinning wheel at a rate that is too low to portray the real frequency at which the spokes pass. Another example is given in figure D.3, where for a certain sampling frequencies, two possible 'real' sinusoidals are plotted.

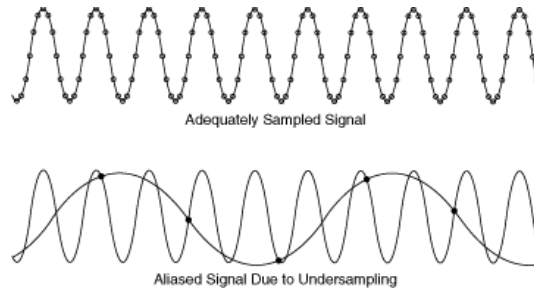


**Figure D.3:** A well sampled signal, and an undersampled frequency. A different sinusoidal can be fitted through the under sampled points; an alias is formed.).

To prevent aliasing from occurring, one can only analyze frequencies up to half the sampling frequency. This frequency is called the *Nyquist frequency*:

$$f_{Nyq} = \frac{1}{2}f_s \quad (D.3)$$

Reversibly one can say that the sampling frequency  $f_s$  should be at least twice the highest frequency that one wants to analyze. The mathematical proof of the Nyquist-Shannon sampling theorem is left to the reader to be found in literature.

Related to this, is another signal processing phenomenon called *Folding*. Positive valued frequencies also have aliases on the negative-frequency axis. So when the absolute value or square is taken from a DFT, an image of the frequencies from 0 to  $f_s/2$  is produced which runs from  $f_s$  to  $f_s/2$ . So a mirror image of the frequencies is portrayed with the mirror line lying at  $f_s$ . This is called *folding*. An example of folding is given in figure D.4.

The energy of all the frequencies is evenly split over the real frequency and its mirrored alias at  $f > f_s$ , so when processing a signal, all the alias frequencies  $f > f_s$  are discarded, and the original frequencies ( $f < f_s$ ) are multiplied by factor two.

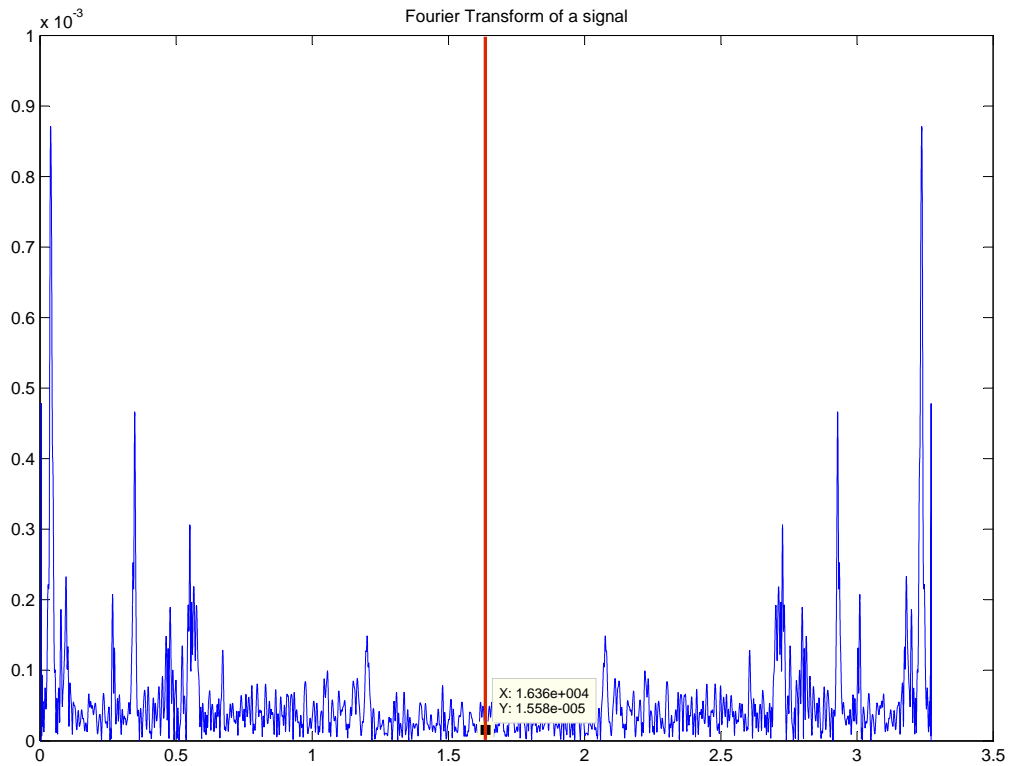


**Figure D.4:** An example of folding. In this case the Nyquist or Folding frequency was 1.63 Hz, indicated by the red line.)



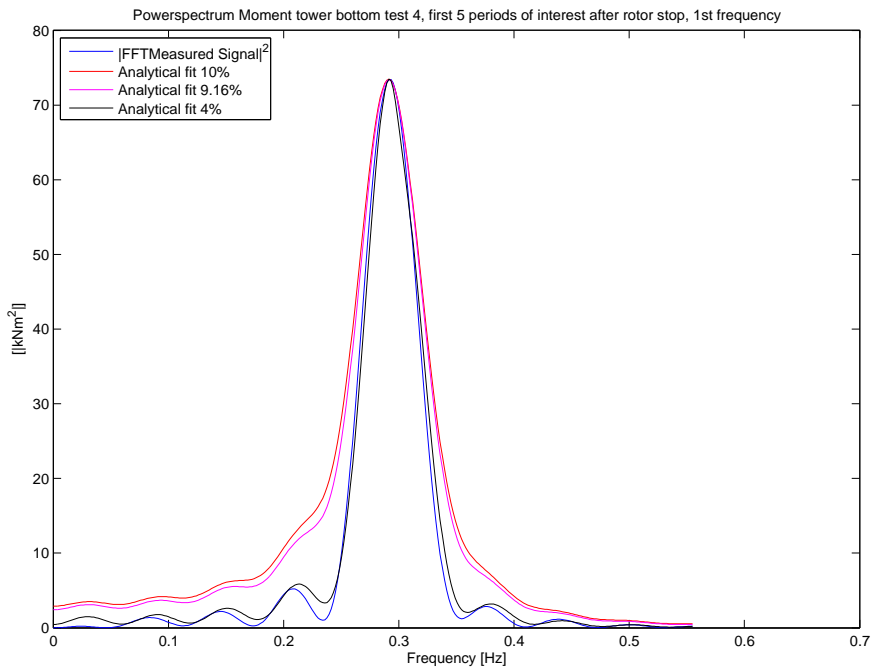
# Damping Assessment Results

Damping results of Hanning-windowed sections of 41 seconds length

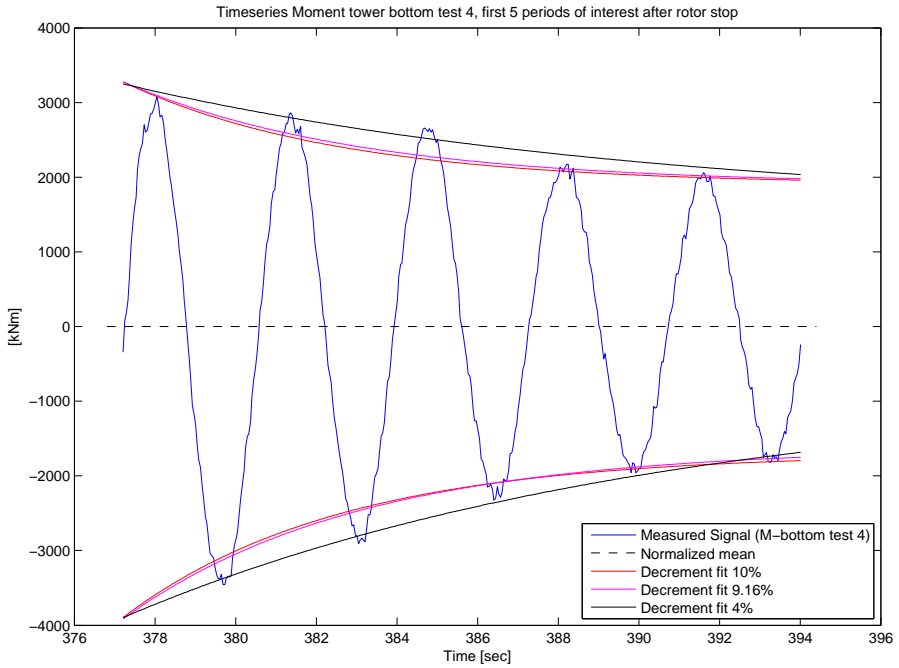
	Test 1		Test 2		Test 3		Test 4		Test 5		Test 6	
	Frequency	Damping										
Acc 1st	0.325	4.596	0.303	6.634	0.313	7.117	0.289	5.524	0.300	6.420	0.302	5.899
Mt 1st	0.296	6.536	0.298	6.467	0.294	6.236	0.299	6.212	0.296	5.932	0.297	6.292
Mor 1st											0.299	5.967
Mb 1st	0.297	6.633	0.297	6.546	0.294	6.198	0.298	6.148	0.295	6.030	0.297	6.269
Acc 2nd	0.780				0.767	2.306	0.771	2.465	0.746	2.032	0.776	
Mt 2nd	0.880	1.960	0.885	2.006	0.883	1.976	0.880	2.017	0.881	2.122	0.882	1.997
Mor 2nd											0.775	4.040
Mb 2nd	0.882	1.871	0.876	2.506	0.882	1.967	0.880	2.194	0.875	2.137	0.880	1.971
	Test 8		Test 9		Test 10		Test 11		Test 13		Test 14	
	Frequency	Damping										
Acc 1st	0.308	5.711	0.283	6.297	0.299	8.374	0.299	7.456	0.298	5.413	0.299	6.310
Mt 1st	0.290	6.061	0.290	6.057	0.296	5.701	0.293	6.185	0.293	5.802	0.293	5.955
Mor 1st	0.290	6.094	0.289	6.104	0.297	5.896	0.294	5.977	0.293	5.874	0.293	5.898
Mb 1st	0.289	6.047	0.289	6.173	0.296	5.702	0.294	6.147	0.293	5.858	0.293	5.906
Acc 2nd	0.788		0.782	2.283	0.795	2.258	0.770	2.254	0.781	2.764	0.741	
Mt 2nd	0.867	2.624	0.877	2.173	0.880	2.045	0.882	2.006	0.875	2.160	0.884	2.296
Mor 2nd			0.784	2.827	0.790	1.867	0.780	3.139	0.780	2.610	0.748	
Mb 2nd	0.849	3.351	0.876	2.134	0.882	2.007	0.883	2.056	0.836	1.831	0.880	2.142

Figure E.1: Results of Q-factor analyses on all 12 tests, based on 41 second Hanning windowed sections. These numbers were averaged to give the values given in figure 3.9.

## Damping results of Rectangular windowed first linear decaying cycles



**Figure E.2:** Measured and analytical fitted power spectrum for first 5 cycles of the bending moment at tower bottom for test 4. Only the first natural frequency is present in this signal at the tower bottom. The fit with 4% damping ratio is found to be the closest fit.



**Figure E.3:** Measured time response of first 5 cycles of the bending moment at tower bottom for test 4. The same fitted damping ratio's are plotted as logarithmic decrement. Again, the 4% damping ratio is found to be the best fit. The first natural frequency clearly dominates the time response.

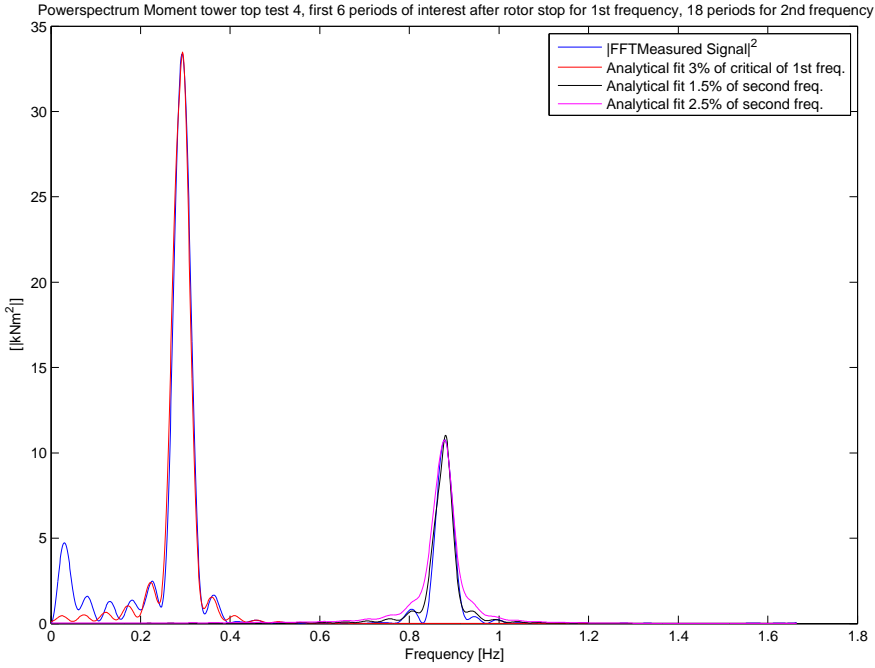


**Figure E.4:** Measured and analytical fitted power spectrum for first 6 cycles of 1st natural frequency and 18 cycles for the second frequency of the bending moment at tower top for test 4. The fit with 1.5% damping ratio for the second frequency is found to be the closest fit. The first natural frequency is well fitted with 3% damping ratio.

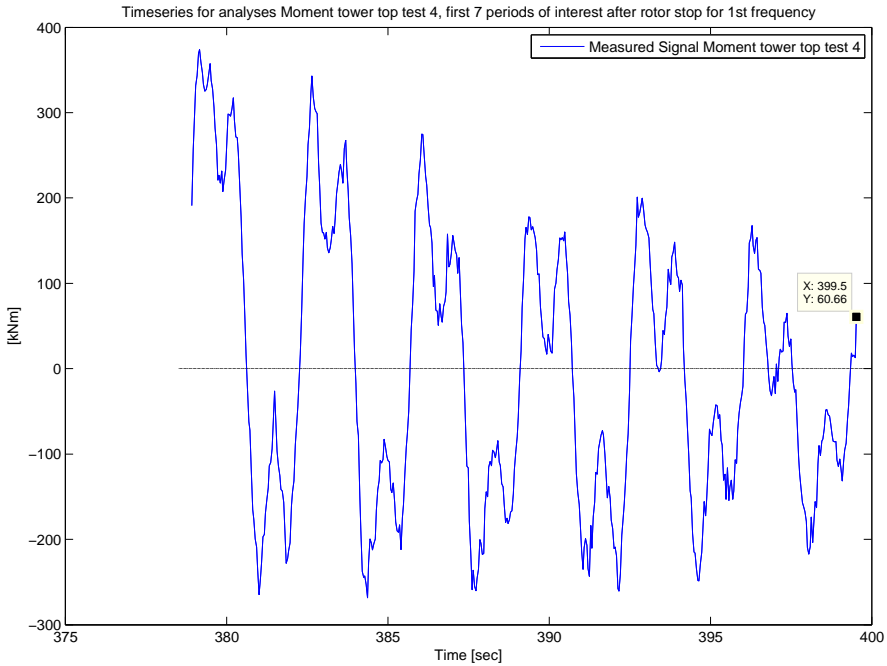


**Figure E.5:** Time series taken for deriving the power spectrum for the first 6 cycles of 1st natural frequency and 18 cycles for the second frequency of the bending moment at tower top for test 4.



## Test Opportunities and Roadmap

This appendix covers different opportunities for in situ experiments that were possible at the start of this thesis, it describes the selection procedure which led to the choice of the performed in situ experiment, and finally a roadmap towards the ultimate goal is suggested. To remind the reader, the ultimate goal is to predict the amount of soil damping an OWT will receive for a certain location, related to the types of soil present at that location.

### **Opportunities**

Two different wind farms were suitable for performing measurements:

- Burbo Bank wind farm (BB) - a fully operational farm offshore the west coast of England at the height of Liverpool in the Irish sea
- Sheringham Shoal wind farm (ShSh) - currently under construction offshore the east coast of England, above Norwich

Figure F.1 shows their geographic locations.



**Figure F.1:** Locations of Burbo Bank (red cross) and Sheringham Shoal (yellow cross) wind farms.

The main difference between these farms is their state of construction completion.

The construction phase of Sheringham Shoal creates a situation where measurements can be performed on the foundation (MP+TP) without the tower and RNA on top. As we are only interested in what happens in the soil, this is beneficial because the obtained signal from strain gauges or accelerometers on the foundation will be free of dynamic influence of the top part.

ShSh wind farm is owned by the Norwegian oil company Statoil, and they launched a fatigue monitoring project involving the full time measurement of occurring stresses (via strain gauges) on two of the foundations. This implies that two of the foundations already had a Power Load Monitoring (PLM) system installed on them.

To be able to measure a dynamic decaying amplitude signal (as the one plotted in figure 2.5) on such a foundation, it has to be given an initial excitation or

disturbance. This could for instance be done by attaching a cable to the top of the foundation which is then tensioned by a tugboat. The cable would have a quick release mechanism and a tension measurement device. After the tensioned cable is 'snapped' by the quick release mechanism, the foundation will start to vibrate in its natural modeshapes and corresponding natural frequencies. Another way of exciting such a structure is by installing a shaker. This is an installation that can vibrate a structure with a controllable frequency and amplitude by means of rotating masses or dynamic hydraulic forces applied on the structure. Advantage of a shaker over a snapping tension cable is that you can decide which frequencies you want to evaluate. Nevertheless, installing a heavy shaker on top of a TP will require a costly offshore crane on a barge, being more costly than a tugboat.

Figure F.2 visualizes this measurement setup with the two excitation methods. It is expected that this setup will yield large scientific knowledge.

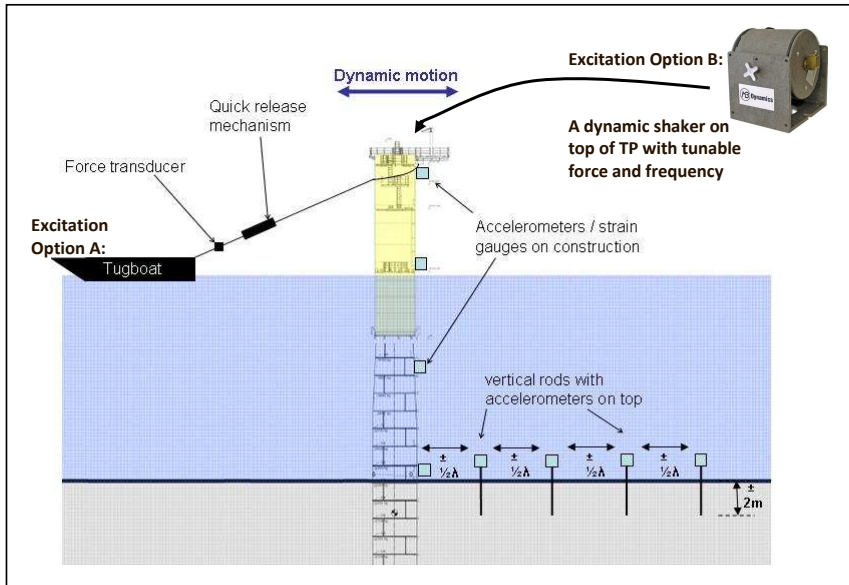


**Figure F.2:** Schematic view of the experimental setup with most expected 'knowledge gain', in which using a shaker would be more favorable than using a tensioned cable as excitation method.

Performing measurements on the operational OWTs of Burbo Bank will include the dynamic effect of the tower and RNA which is less desirable. Though a benefit of performing measurements on this site is that a 'rotor stop' procedure can be used to give the structure its initial excitation. During a rotor stop, the fully operational and turning rotor blades are pitched out of the wind at a speed of about 6 degr/sec up to an angle of 80 degrees with respect to the angle in which they were during full operation. This makes the 107m diameter-rotor brake fast enough to give the nacelle a certain (mainly-) for-aft vibration. This vibration is mainly caused by a relatively sudden removal of the thrust force, where even some suction towards the wind direction occurs because of the sudden change in angle of the wind with respect to the blades. Also the law

of constant rotational momentum in a system and the gyroscopic effect play a role in the vibrations after such a rotor stop.

Besides the advantage of relatively easy excitation method (rotor stop), Burbo Bank wind farm has the advantage that two OWTs were already equipped with strain gauges and accelerometers during installation of the WF. Because of these reasons, the measurement set up at Burbo Bank is ready to go and costless; the rotor stop procedure and the data acquisition is all software controlled and can be done so to speak from behind the desk.

The critical reader might still miss something in the described measurement set ups. Since we are interested in how much energy is dissipated in the soil, measuring the reaction of that soil is recommended. Besides measuring the reaction of the steel structure via strain gauges and accelerometers, placing an array of accelerometers on the soil surface to measure the soil waves is even more essential. Unfortunately this would require a costly operation; a diver would have to install rods on the soil surface and equip these rods with accelerometers.

From all this we can conclude that quite some good possibilities and combinations of these measurement facets exist. From a scientific point of view, the most knowledge gain is expected to be received from the experimental set up as drawn in figure F.2; measuring the behavior of only a foundation, measuring the soil reaction through an array of accelerometers on the soil surface and exciting the structure by means of a shaker. Coincidence has it that this set up also happens to be the most expensive one.

The different experimental options at the two locations were combined to form nine different set ups, of which one was to be selected on basis of estimated scientific knowledge gain, financial cost and relative short term achievability. Figure F.3 gives a visual representation of these options.

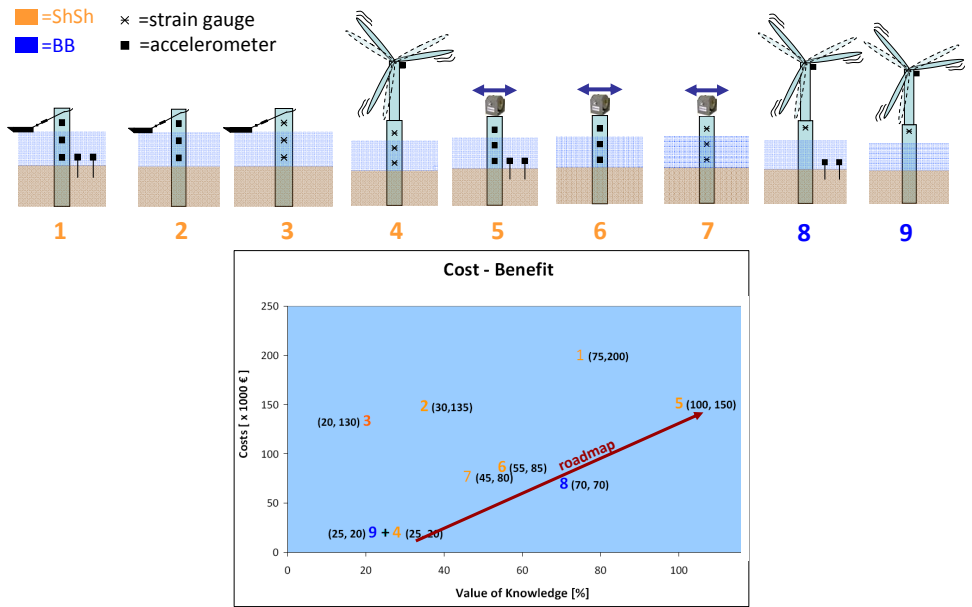


**Figure F.3:** Schematic view of the nine possible experimental set ups and result of the cost benefit analysis.

Since the PLM system at ShSh consists only of uncalibrated strain gauges, it was considered expanding the system with accelerometers. This explains the difference between options '2' and '3', and '6' and '7'. From the cost-benefit graph it can be concluded that only options '9', '4', '8' and '5' have to be taken into consideration. The only difference between options 4 and 9 is that option '9' is ready to be used, and performing a rotor stop at ShSh will have to wait until summer 2011 when the turbines are expected to be installed. That leaves only options 9,8 and 5 for realistic experimental set ups.

## Roadmap

The previous section was part of the output of the first trajectory of this thesis, in which numerous meetings were held with Statoil and internally within Siemens concerning the choice of experiment. Eventually the author suggested a two-phase-roadmap to reach the ultimate goal.

The first phase of this roadmap is the nearly costless experiment 'number 9' which is performing a rotor stop on one of the two OWTs at BB which is equipped with a PLM system. Performing this experiment, making a model serving the analysis of the obtained experimental data, and analysing the obtained data to try and make an educated guess about the soil damping at the location of the used OWT is the scope of this thesis. It has to be noted that this experiment is limited in its possible information output since only the structure's reaction is measured. Since the soil's reaction is not measured, it will not be possible to map how this energy dissipation is related to soil types.

Another limitation of the obtained signal from this experiment will be the influence of the dynamics of the tower and RNA. Also, a rotor stop is a less precise definable forcing than a shaker or snapping tension cable.

Nevertheless, this experiment will yield valuable learning on this subject and the fact of it being a very low-cost experiment, makes it an evident first step. An important side note must be mentioned; all OWTs at BB are equipped with so called *G-sensors* in their nacelle which are a type of accelerometer with a non-constant sampling frequency. Nowadays all Siemens turbines are equipped with these *G-sensors*, so if these signals turn out to be useable for analysis, many of these low-cost experiments can be performed on all locations with relative new Siemens turbines.

The second phase will consist of expanding the measurement locations. Apart from the structure itself, also the soil reaction will be measured via accelerometers installed on the soil surface. This will render information on the propagation and dispersion of waves in the soil surface. Knowing exactly the type of soil on which these accelerometers are installed, lets us connect the properties of that soil to the attenuation of waves or energy in that specific soil. This expansion of measurement locations might be done at a complete OWT on which a rotor stop can be performed, or on a foundation only which lacks the dynamic influence of the tower and RNA. This choice depends on the outcome of the first phase. If the influence of the dynamics of the tower and RNA really turn out to be blocking proper analysis of the damping in soil-structure interaction, then performing measurements on a foundation without tower is a logical second

step. This path or roadmap is indicated with the red arrow in the cost-benefit graph in figure F.3.



## Pinned Beam Model

One of the models that was developed in the process of attempting to develop a satisfactory model was a pinned beam model. The pinned beam is constrained at its bottom by equivalent stiffness (a rotational and translational spring) and damping of the soil. The facets of this model are visualized in figure G.1.

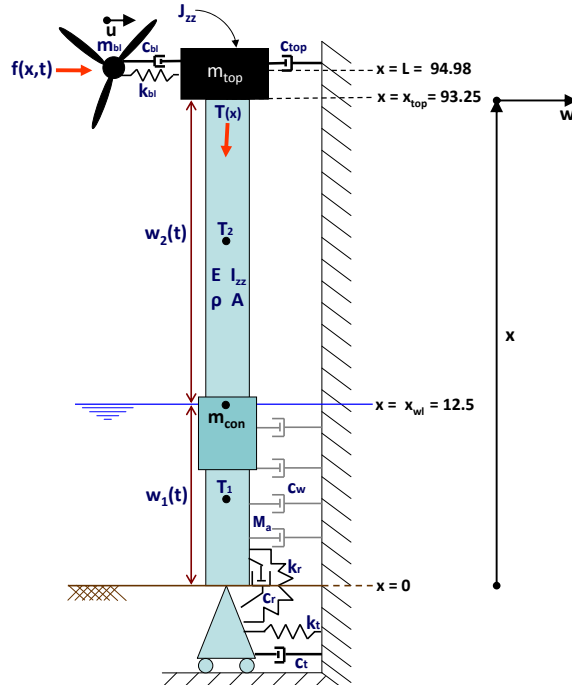


**Figure G.1:** Second model used to represent the performed rotor stops.  $x_{wl} = 12.5$  was the mean sealevel (waterline) during the tests.

This model, other than the finally used 'constrained beam' model presented in chapter 4, is solved in the time domain. It was thought that this second way of solving might serve as an extra piece of material for those interested in modal analysis.

## Solution in the Time domain

### The governing equations

This model's behavior can be summarized by three sets of equations; the equation of motion, the boundary conditions and the interface conditions.

### Equation of Motion

The EOM has the following form:

$$\begin{aligned}
 EI \frac{\partial^4 w(x, t)}{\partial x^4} + m(x) \frac{\partial^2 w(x, t)}{\partial t^2} + T(x) \frac{\partial^2 w(x, t)}{\partial x^2} + c_w(x) \frac{\partial w(x, t)}{\partial t} = & \quad (G.1) \\
 f(x, t) - m_{top} \frac{\partial^2 w(x, t)}{\partial t^2} \delta(x - L) + J \frac{\partial^3 w}{\partial t^2 \partial x} \delta'(x - L) \\
 - C_{top} \frac{\partial w(x, t)}{\partial t} \delta(x - L) - m_{con} \frac{\partial^2 w(x, t)}{\partial t^2} \delta(x - x_{wl}) + C_r \frac{\partial^2 w(x, t)}{\partial t \partial x} \delta'(x)
 \end{aligned}$$

where

$$w(x, t) = \begin{cases} w_1(x, t), & 0 < x < x_{wl} \\ w_2(x, t), & x_{wl} < x < L \end{cases} \quad (G.2)$$

$$m(x) = \begin{cases} m_1 = \rho A + Ma, & 0 < x < x_{wl} \\ m_2 = \rho A, & x_{wl} < x < L \end{cases} \quad (G.3)$$

$$T(x) = \begin{cases} T_1 & 0 < x < x_{wl} \\ T_2 & x_{wl} < x < L \end{cases} \quad (G.4)$$

$$c_w(x) = \begin{cases} c_{w,1} = C_w, & 0 < x < x_{wl} \\ c_{w,2} = 0, & x_{wl} < x < L \end{cases} \quad (G.5)$$

$$f(x, t) = P \delta(x - \xi) p(t) \quad (G.6)$$

As can be seen in G.2 to G.5 in the EOM, this model contains some conditions for the mass per meter length,  $m(x)$ , the compressional force,  $T(x)$  and the distributed hydrodynamic damping,  $c_w(x)$ , as these values change over the height of the structure. This requires us to consider two horizontal movements  $w_1(x, t)$  and  $w_2(x, t)$ .

The compressional force is split up in two values  $T_1$  and  $T_2$ .  $T_2$  is the compression force acting at the point half way between  $x_{wl}$  and  $x_{top}$  (see G.1, so it is caused by the dead weight of the RNA and of the tower part above this point. This  $T_2$  is taken to apply for the entire top part of the beam, from  $x_{wl}$  upwards.  $T_1$  then consists of  $T_2$  plus the dead weight of  $m_{con}$  and half of the beam from

mudline until  $x_{wl}$ .  $T_1$  is again considered to be the constant compressional force in the beam from  $x_{wl}$  downwards.

### The Boundary Conditions

The structure is constrained at its bottom by a horizontal translational spring which opposes horizontal movement. This is incorporated by introducing a shear force equilibrium at this location (eq. G.7). The moment at its bottom is in equilibrium with the rotational spring (and rotational dashpot, but that has already been included in the EOM). The top free end of the beam is conditioned by the fact that a shear force equilibrium exists with the compressional force caused by the RNA, and there can't be a moment. These four conditions result in the boundary conditions having the following form:

$$EI \frac{\partial^3 w(0, t)}{\partial x^3} + K_t w(0, t) + T_1 \frac{\partial w(0, t)}{\partial x} = 0 \quad (\text{G.7})$$

$$EI \frac{\partial^2 w(0, t)}{\partial x^2} - K_r \frac{\partial w(0, t)}{\partial x} = 0 \quad (\text{G.8})$$

$$\frac{\partial^2 w(L, t)}{\partial x^2} = 0 \quad (\text{G.9})$$

$$EI \frac{\partial^3 w(L, t)}{\partial x^3} + T_2 \frac{\partial w(L, t)}{\partial x} = 0 \quad (\text{G.10})$$

Note that the boundary conditions are kept free of time dependent items (no derivatives to time). This is necessary in order to be able to find the natural frequencies and normal modes in the same manner as was done with the first model. So it is chosen to 'shift' all the time dependent factors to the EOM in stead of placing them in the BC's.

### The Interface Conditions

Finally the conditions have to be stated to govern the interface between the upper and lower part at  $x_{wl} = 12.5$ , the Interface Conditions (IC):

$$w_1 - w_2 = 0 \quad (\text{G.11})$$

$$\frac{\partial w_1}{\partial x} - \frac{\partial w_2}{\partial x} = 0 \quad (\text{G.12})$$

$$\frac{\partial^2 w_1}{\partial x^2} - \frac{\partial^2 w_2}{\partial x^2} = 0 \quad (\text{G.13})$$

$$EI\left(\frac{\partial^3 w_1}{\partial x^3} - \frac{\partial^3 w_2}{\partial x^3}\right) + T_1 \frac{\partial w_1}{\partial x} - T_2 \frac{\partial w_2}{\partial x} = 0 \quad (\text{G.14})$$

In words they are respectively; the same horizontal movement between upper and lower part of the beam, the same slope, the same bending moment and the same shear force.

Now we shall look for the solution for  $w(x,t)$  in the form of a summation of the location-dependent part times a time dependent part:

$$w(x,t) = \sum_n^{\infty} q_n(t)W_n(x) \quad (\text{G.15})$$

These two parts will be found in the next sections. This form is also the basis of the 'separation of variables' technique, in which an expressions is solved by looking for the solutions of the individual variables and combining these solutions to find the total solution. But because of the extra time dependent elements in the EOM (the mass of the nacelle, the top damper and the rotational damper), we will see it is not possible to solve the time-dependent part of the solution with the separation of variables technique. The time dependent variable is coupled to the normal modes, so here separation of variables is not possible.

### The Location function

We will look for the normal modes  $W_n(x)$  making the same assumptions as was previously done; we have to presume to have a homogeneous EOM (equalling the right hand side of equation G.1 to zero) without damping. Then filling in the general solution of G.15 with  $q_n(t) = e^{i\omega t}$  to get

$$EIW_n'''' - m(x)\omega_n^2 W_n + T(x)W_n'' = 0 \quad (\text{G.16})$$

The dispersion equation gives us the relation between the wavenumber  $\beta_n$  and the natural frequencies of the normal modes  $\omega_n$ . To derive the dispersion equation we also presume a general form for the location dependent part:  $W(x) = e^{i\beta_n x}$  and insert it in the above expression to get the following expression:

$$EI\beta_n^4 - m(x)\omega_n^2 - T(x)\beta_n^2 = 0 \quad (\text{G.17})$$

As now the top part of the tower has a different mass than the bottom part, we get four different (usable)  $\beta_n$ 's:

$$\beta_{n,1,t} = +\sqrt{\frac{T_2 + \sqrt{T_2^2 + 4EI\rho A\omega_n^2}}{2EI}} \quad (\text{G.18})$$

$$\beta_{n,3,t} = +\sqrt{\frac{-T_2 + \sqrt{T_2^2 + 4EI\rho A\omega_n^2}}{2EI}} \quad (\text{G.19})$$

$$\beta_{n,1,b} = +\sqrt{\frac{T_1 + \sqrt{T_1^2 + 4EI(\rho A + M_a)\omega_n^2}}{2EI}} \quad (\text{G.20})$$

$$\beta_{n,3,b} = +\sqrt{\frac{-T_1 + \sqrt{T_1^2 + 4EI(\rho A + M_a)\omega_n^2}}{2EI}} \quad (\text{G.21})$$

The general solution of this dispersion equation distinguishes the top and the bottom part of the beam, yielding two equations with in total eight unknown constants:

$$\begin{aligned} W_1(x) &= A_2 \cosh(\beta_{n,3,b}x) + B_2 \sinh(\beta_{n,3,b}x) + C_2 \cos(\beta_{n,1,b}x) + D_2 \sin(\beta_{n,1,b}x) \\ W_2(x) &= A_1 \cosh(\beta_{n,3,t}x) + B_1 \sinh(\beta_{n,3,t}x) + C_1 \cos(\beta_{n,1,t}x) + D_1 \sin(\beta_{n,1,t}x) \end{aligned} \quad (\text{G.22})$$

We also have eight conditions (the BCs and the ICs) to find these constants. Filling these general solutions in in the BCs and ICs of equations G.7 to G.14, we can derive the following coefficient matrix:

$$\left[ \begin{array}{c}
 K_t \\
 \beta_{n,3,b}^2 \\
 0 \\
 0 \\
 \cosh(\beta_{n,3,b} x_{wl}) \\
 \sinh(\beta_{n,3,b} x_{wl}) \beta_{n,3,b} \\
 \cosh(\beta_{n,3,b} x_{wl}) \beta_{n,3,b}^2 \\
 EI \sinh(\beta_{n,3,b} x_{wl}) \beta_{n,3,b}^3 + \sinh(\beta_{n,3,b} x_{wl}) \beta_{n,3,b} T_1 - \sinh(\beta_{n,3,b} x_{wl}) \beta_{n,3,b} T_2
 \end{array} \right]$$

$$\begin{array}{c}
 EI \beta_{n,3,b}^3 + T_1 \beta_{n,3,b} \\
 - \frac{K_r \beta_{n,3,b}}{EI} \\
 0 \\
 0 \\
 \sinh(\beta_{n,3,b} x_{wl}) \\
 \cosh(\beta_{n,3,b} x_{wl}) \beta_{n,3,b} \\
 \sinh(\beta_{n,3,b} x_{wl}) \beta_{n,3,b}^2 \\
 EI \cosh(\beta_{n,3,b} x_{wl}) \beta_{n,3,b}^3 + \cosh(\beta_{n,3,b} x_{wl}) \beta_{n,3,b} T_1 - \cosh(\beta_{n,3,b} x_{wl}) \beta_{n,3,b} T_2
 \end{array}$$

$$\begin{array}{c}
 K_t \\
 -\beta_{n,1,b}^2 \\
 0 \\
 0 \\
 \cos(\beta_{n,1,b} x_{wl}) \\
 -\sin(\beta_{n,1,b} x_{wl}) \beta_{n,1,b} \\
 -\cos(\beta_{n,1,b} x_{wl}) \beta_{n,1,b}^2 \\
 EI \sin(\beta_{n,1,b} x_{wl}) \beta_{n,1,b}^3 - \sin(\beta_{n,1,b} x_{wl}) \beta_{n,1,b} T_1 + \sin(\beta_{n,1,b} x_{wl}) \beta_{n,1,b} T_2
 \end{array}$$

$$\begin{aligned}
& -EI\beta_{n,1,b}^3 + T_1\beta_{n,1,b} \\
& \quad - \frac{K_r\beta_{n,1,b}}{EI} \\
& \quad 0 \\
& \quad 0 \\
& \quad \sin(\beta_{n,1,b}x_{wl}) \\
& \quad \cos(\beta_{n,1,b}x_{wl})\beta_{n,1,b} \\
& \quad - \sin(\beta_{n,1,b}x_{wl})\beta_{n,1,b}^2 \\
& -EI\cos(\beta_{n,1,b}x_{wl})\beta_{n,3,b}^3 + \cos(\beta_{n,1,b}x_{wl})\beta_{n,1,b}T_1 - \cos(\beta_{n,1,b}x_{wl})\beta_{n,1,b}T_2
\end{aligned}$$

$$\begin{array}{cc}
0 & 0 \\
0 & 0 \\
\cosh(\beta_{n,3,t}L)\beta_{n,3,t}^2 & \sinh(\beta_{n,3,t}L)\beta_{n,3,t}^2 \\
EI\sinh(\beta_{n,3,t}L)\beta_{n,3,t}^3 + T_2\sinh(\beta_{n,3,t}L)\beta_{n,3,t} & EI\cosh(\beta_{n,3,t}L)\beta_{n,3,t}^3 + T_2\cosh(\beta_{n,3,t}L)\beta_{n,3,t} \\
\quad - \cosh(\beta_{n,3,t}x_{wl}) & \quad - \sinh(\beta_{n,3,t}x_{wl}) \\
- \sinh(\beta_{n,3,t}x_{wl})\beta_{n,3,t} & - \cosh(\beta_{n,3,t}x_{wl})\beta_{n,3,t} \\
- \cosh(\beta_{n,3,t}x_{wl})\beta_{n,3,t}^2 & - \sinh(\beta_{n,3,t}x_{wl})\beta_{n,3,t}^2 \\
\cosh(\beta_{n,3,b}x_{wl})\beta_{n,3,b}^2 & \sinh(\beta_{n,3,b}x_{wl})\beta_{n,3,b}^2 \\
-EI\sinh(\beta_{n,3,t}x_{wl})\beta_{n,3,t}^3 & -EI\cosh(\beta_{n,3,t}x_{wl})\beta_{n,3,t}^3
\end{array}$$

$$\begin{array}{cc}
 0 & 0 \\
 0 & 0 \\
 \cosh - \cos(\beta_{n,1,t} L) \beta_{n,1,t}^2 & -\sin(\beta_{n,1,t} L) \beta_{n,1,t}^2 \\
 EI \sin(\beta_{n,1,t} L) \beta_{n,1,t}^3 - T_2 \sin(\beta_{n,1,t} L) \beta_{n,1,t} & -EI \cos(\beta_{n,1,t} L) \beta_{n,1,t}^3 + T_2 \cos(\beta_{n,1,t} L) \beta_{n,1,t} \\
 -\cos(\beta_{n,1,t} x_{wl}) & -\sin(\beta_{n,1,t} x_{wl}) \\
 \sin(\beta_{n,1,t} x_{wl}) \beta_{n,1,t} & -\cos(\beta_{n,1,t} x_{wl}) \beta_{n,1,t} \\
 \cos(\beta_{n,1,t} x_{wl}) \beta_{n,1,t}^2 & \sin(\beta_{n,1,t} x_{wl}) \beta_{n,1,t}^2 \\
 -\cos(\beta_{n,1,b} x_{wl}) \beta_{n,1,b}^2 & -\sin(\beta_{n,1,b} x_{wl}) \beta_{n,1,b}^2 \\
 -EI \sin(\beta_{n,1,t} x_{wl}) \beta_{n,1,t}^3 & EI \cos(\beta_{n,1,t} x_{wl}) \beta_{n,3,t}^3
 \end{array}
 \left. \vphantom{\begin{array}{cc}} \right]$$

$$\left[ \begin{array}{c}
 A_1 \\
 B_1 \\
 C_1 \\
 D_1 \\
 A_2 \\
 B_2 \\
 C_2 \\
 D_2
 \end{array} \right]$$

Solving the determinant of this matrix yields the frequency equation. In this case this expression is too long and it has no added value being printed here. Solving it with the use of expressions G.18 to G.21 yields the values for  $\omega_n$ .

The expression for the normal modes,  $W_n(x)$  is found by expressing one of the unknowns in the other seven. Here again, this expression covers a couple of pages and doesn't add value being depicted here.

### The Time function

On our quest for an expression for the time dependent part, ( $q_n(t)$ ), we fill in the general solution (G.15) in the EOM to find

$$\begin{aligned}
& EI \sum_n^{\infty} q_n W_n'''' + m(x) \sum_n^{\infty} \ddot{q}_n W_n + c_w(x) \sum_n^{\infty} \dot{q}_n W_n + T(x) \sum_n^{\infty} q_n W_n'' = \\
& f(x, t) - m_{top} \sum_n^{\infty} \ddot{q}_n W_n \delta(x - L) + J \sum_n^{\infty} \ddot{q}_n W_n' \delta'(x - L) \quad (G.23) \\
& - C_{top} \sum_n^{\infty} \dot{q}_n W_n \delta(x - L) - m_{con} \sum_n^{\infty} \ddot{q}_n W_n \delta(x - x_{wl}) + C_r \sum_n^{\infty} \dot{q}_n W_n' \delta'(x)
\end{aligned}$$

The first and fourth term on the left hand side of this equation can be simplified by using the relation of G.16 to get

$$\begin{aligned}
& m(x) \sum_n^{\infty} \ddot{q}_n W_n + c_w(x) \sum_n^{\infty} \dot{q}_n W_n + m(x) \sum_n^{\infty} q_n \omega_n^2 W_n = \quad (G.24) \\
& f(x, t) - m_{top} \sum_n^{\infty} \ddot{q}_n W_n \delta(x - L) + J \sum_n^{\infty} \ddot{q}_n W_n' \delta'(x - L) \\
& - C_{top} \sum_n^{\infty} \dot{q}_n W_n \delta(x - L) - m_{con} \sum_n^{\infty} \ddot{q}_n W_n \delta(x - x_{wl}) + C_r \sum_n^{\infty} \dot{q}_n W_n' \delta'(x)
\end{aligned}$$

Now to fulfill the orthogonality property, we have to multiply the terms with another mode  $W_m$ , and integrate the products over the full length of the beam, to get

$$\begin{aligned}
& \ddot{q}_m \int_0^L m(x) W_m^2 dx + \sum_n^{\infty} \dot{q}_n \int_0^L c_w(x) W_n W_m dx + \omega_m^2 q_m \int_0^L m(x) W_m^2 dx \\
& = \int_0^L f(x, t) W_m dx - m_{top} \sum_n^{\infty} \ddot{q}_n \int_0^L W_n W_m \delta(x - L) dx \quad (G.25) \\
& + J \sum_n^{\infty} \ddot{q}_n \int_0^L W_n' W_m \delta'(x - L) dx - C_{top} \sum_n^{\infty} \dot{q}_n \int_0^L W_n W_m \delta(x - L) dx \\
& - m_{con} \sum_n^{\infty} \ddot{q}_n \int_0^L W_n W_m \delta(x - x_{wl}) + C_r \sum_n^{\infty} \dot{q}_n \int_0^L W_n' W_m \delta'(x) dx
\end{aligned}$$

Working out some of these integrals, we get

$$\begin{aligned}
& \ddot{q}_m \int_0^L m(x) W_m^2 dx + \sum_n \dot{q}_m \int_0^L c_w(x) W_n W_m dx + \omega_m^2 q_m \int_0^L m(x) W_m^2 dx \\
&= \int_0^L f(x, t) W_m dx - m_{top} \sum_n \ddot{q}_n (W_n W_m)_{x=L} \\
&- J \sum_n \ddot{q}_n (W_n' W_m)'_{x=L} - C_{top} \sum_n \dot{q}_n (W_n W_m)_{x=L} \\
&- m_{con} \sum_n \ddot{q}_n (W_n W_m)_{x=x_{wl}} - C_r \sum_n \dot{q}_n (W_n' W_m)'_{x=0}
\end{aligned} \tag{G.26}$$

Because the  $m(x)$  and  $c_w(x)$  terms in G.25 have different values for the lower and upper part of the tower, these integrals are split up in a part from 0 to  $x_{wl}$  and a part from  $x_{wl}$  to L. These terms will be indicated with a '\*' from now, and thus have the following value;

$$m_m^* = \int_0^L m(x) W_m^2 dx = m_1 \int_0^{x_{wl}} W_{1,m}^2 dx + m_2 \int_{x_{wl}}^L W_{2,m}^2 dx \tag{G.27}$$

$$\int_0^L c_w(x) W_n W_m dx = C_w \int_0^{x_{wl}} W_{1,n} W_{1,m} dx \tag{G.28}$$

and

$$f^* = \int_0^L f(x, t) W_m dx = \int_0^L P \delta(x - L) \delta(t) W_m dx = P W_{2,m} |_{x=L} \delta(t)$$

Further,  $m_2$  and  $m_1$  in the last four terms in G.26 represent the mass value at respectively  $x=L$  and  $x=0$  because of condition G.3.

The last two terms were simplified with the following rule for integrating the product of a function and the derivative of a Dirac Delta function:

$$\int_{-\infty}^{\infty} f(x) \delta^{(n)}(x - x_{wl}) dx = (-1)^n f^{(n)}(x_{wl}) \tag{G.29}$$

Now, once again, if all terms proportional to  $\ddot{q}$ ,  $\dot{q}$  and  $q$  are collected in equation G.25, this equation can be written in the following form:

$$\underline{\mathbf{M}}\ddot{\mathbf{q}} + \underline{\mathbf{C}}\dot{\mathbf{q}} + \underline{\mathbf{K}}\mathbf{q} = \underline{\mathbf{f}}(t) \quad (\text{G.30})$$

If we consider three modes, these matrices would look like

$$\underline{\mathbf{M}} = \begin{bmatrix} m_1^* + m_{top}W_1W_1|_{x=L} + JW_1'W_1|'_{x=L} + m_{con}W_1W_1|_{x=x_{wl}} \\ m_{top}W_1W_2|_{x=L} + JW_1'W_2|'_{x=L} + m_{con}W_1W_2|_{x=x_{wl}} \\ m_{top}W_1W_3|_{x=L} + JW_1'W_3|'_{x=L} + m_{con}W_1W_3|_{x=x_{wl}} \\ \\ m_{top}W_2W_1|_{x=L} + JW_2'W_1|'_{x=L} + m_{con}W_2W_1|_{x=x_{wl}} \\ m_2^* + m_{top}W_2W_2|_{x=L} + JW_2'W_2|'_{x=L} + m_{con}W_2W_2|_{x=x_{wl}} \\ m_{top}W_2W_3|_{x=L} + JW_2'W_3|'_{x=L} + m_{con}W_2W_3|_{x=x_{wl}} \\ \\ m_{top}W_3W_1|_{x=L} + JW_3'W_1|'_{x=L} + m_{con}W_3W_1|_{x=x_{wl}} \\ m_{top}W_3W_2|_{x=L} + JW_3'W_2|'_{x=L} + m_{con}W_3W_2|_{x=x_{wl}} \\ m_3^* + m_{top}W_3W_3|_{x=L} + JW_3'W_3|'_{x=L} + m_{con}W_3W_3|_{x=x_{wl}} \end{bmatrix}$$

or  $\underline{\mathbf{M}} = \underline{\mathbf{m}}_{top} \underline{\mathbf{W}}_i \underline{\mathbf{W}}_j |_{x=L} + \underline{\mathbf{J}}(\underline{\mathbf{W}}_i' \underline{\mathbf{W}}_j)' |_{x=L} + \underline{\mathbf{m}}^*$  with  $\mathbf{m}_{i,i}^* = \mathbf{m}_i^*$  &  $\mathbf{m}_{i,j}^* = 0$

$$\underline{\mathbf{C}} = \begin{bmatrix} C_w[W_1W_1]_0^{x_{wl}} + C_{top}W_1W_1|_{x=L} + C_rW_1'W_1|'_{x=0} \\ C_w[W_1W_2]_0^{x_{wl}} + C_{top}W_1W_2|_{x=L} + C_rW_1'W_2|'_{x=0} \\ C_w[W_1W_3]_0^{x_{wl}} + C_{top}W_1W_3|_{x=L} + C_rW_1'W_3|'_{x=0} \\ \\ C_w[W_2W_1]_0^{x_{wl}} + C_{top}W_2W_1|_{x=L} + C_r(W_2'W_1)'_{x=0} \\ C_w[W_2W_2]_0^{x_{wl}} + C_{top}W_2W_2|_{x=L} + C_r(W_2'W_2)'_{x=0} \\ C_w[W_2W_3]_0^{x_{wl}} + C_{top}W_2W_3|_{x=L} + C_r(W_2'W_3)'_{x=0} \end{bmatrix}$$

$$\begin{bmatrix} C_w[W_3W_1]_0^{x_{wl}} + C_{top}W_3W_1|_{x=L} + C_r(W_3'W_1)'_{x=0} \\ C_w[W_3W_2]_0^{x_{wl}} + C_{top}W_3W_2|_{x=L} + C_r(W_3'W_2)'_{x=0} \\ C_w[W_3W_3]_0^{x_{wl}} + C_{top}W_3W_3|_{x=L} + C_r(W_3'W_3)'_{x=0} \end{bmatrix}$$

or  $\underline{\mathbf{C}} = \underline{\mathbf{C}}_w[\underline{\mathbf{W}}_i \underline{\mathbf{W}}_j]_0^{x_0} + \underline{\mathbf{C}}_{top} \underline{\mathbf{W}}_i \underline{\mathbf{W}}_j|_{x=L} + \underline{\mathbf{C}}_r(\underline{\mathbf{W}}_i' \underline{\mathbf{W}}_j)'_{x=0}$

$$\underline{\mathbf{K}} = \begin{bmatrix} \omega_1^2 m_1^* & 0 & 0 \\ 0 & \omega_2^2 m_2^* & 0 \\ 0 & 0 & \omega_3^2 m_3^* \end{bmatrix}$$

and the forcing vector

$$\underline{\mathbf{f}}(t) = \begin{bmatrix} PW_1|_{x=L} \\ PW_2|_{x=L} \\ PW_3|_{x=L} \end{bmatrix} \cdot p(t) \quad \text{with} \quad p(t) = \frac{1}{\Delta t \sqrt{\pi}} e^{-\frac{(t-t_0)^2}{\Delta t^2}}$$

The Dirac Delta function of time ( $\delta(t)$ ) has been replaced by an exponential function in the forcing vector.

To find the natural frequencies of this system, we look at the homogeneous case of equation G.30 where the external forcing is put to zero, and we presume for  $\underline{\mathbf{q}} = \underline{\mathbf{Q}} e^{i\omega t}$ , to get

$$-\omega^2 \underline{\mathbf{M}} + i\omega \underline{\mathbf{C}} + \underline{\mathbf{K}} = 0 \quad (\text{G.31})$$

Solving the determinant of this summed up matrix yields the natural (eigen-)frequencies of this system. For simplicity, in a system with relatively low damping, the second term in the above summation can be put to zero since it has little influence on the values of the frequencies, so solving the following statement yields the natural frequencies of this system:

$$\det | -\underline{\mathbf{M}}\omega^2 + \underline{\mathbf{K}} | = 0 \quad (\text{G.32})$$

The coupled set of differential equations which is now defined by G.30 can be solved to find  $q_n(t)$ . Multiplying this value by the  $n^{th}$  normal mode  $W_n$  and doing so for more modes and summing up the products (as according to equation G.15), gives us the total horizontal movement response  $w(x,t)$  during a certain moment in time  $t$  and at a certain location  $x$  along the tower.

**H**

## Applied Values for Model Parameters

Symbol	Description	Value	SI unit
$A$	Weighted average cross-sectional surface area over entire vertical length of the structure	0.732	$m^2$
$C_d$	Hydrodynamic drag coefficient	1	-
$C_{a,w}$	Added mass coefficient for sea water	2	-
$C_{a,w+s}$	Added mass coefficient for sea water and pile plug	1	-
$D_i$	Weighted average inner diameter of MP, TP and Tower	4.253	$m$
$D_o$	Weighted average outer diameter of MP, TP (plus overlap) and Tower	4.359	$m$
$D_{o,mp,sub}$	Outer diameter MP water-submerged (for added mass of water calculation)	5.036	$m$
$D_{o,mp,emb}$	Outer diameter MP soil-embedded (for added mass of water and soil plug calculation)	4.7	$m$
$E$	Young's modulus of construction steel	$2.100 \cdot 10^{11}$	$\frac{N}{m^2}$
$E_s$	Young's modulus of soil	$1.300 \cdot 10^8$	$\frac{N}{m^2}$
$I_{zz}$	Second moment of area	1.926	$m^4$
$M_{a,s}$	Added mass of the sea water	$4.083 \cdot 10^4$	$kg$
$M_{a,s+w}$	Added mass of the sea water and soil plug in the monopile tip	$2.325 \cdot 10^4$	$kg$
$m_{bl}$	Mass of the 3 blades	$5.550 \cdot 10^4$	$kg$
$m_{con}$	Mass of the grouted connection	$8.510 \cdot 10^4$	$kg$
$m_{top}$	Mass of the nacelle	$1.745 \cdot 10^5$	$kg$

---

$q_s$	Shaft skin friction along the outer skin surface of the monopile	1.200	$\frac{N}{m^2}$
$\rho_s$	Unit weight of construction steel	7850	$\frac{kg}{m^3}$
$\rho_w$	Unit weight of sea water	1025	$\frac{kg}{m^3}$
$T_1$	Constant compressional force of lower part of the structure	$6.157 \cdot 10^6$	$N$
$T_2$	Constant compressional force of middle part of the structure	$7.380 \cdot 10^6$	$N$
$T_3$	Constant compressional force of top part of the structure	$3.960 \cdot 10^6$	$N$
$V_0$	Initial velocity of auxiliary rotor mass	3	$\frac{m}{s}$

---

#### Impedance coefficients

---

$c_{bl}$	Dashpot coefficient for damping of the blades	$1.087 \cdot 10^4$	$\frac{Ns}{m}$
$c_s$	Distributed dashpot coefficient for damping of the soil	$7.504 \cdot 10^7$	$\frac{Ns}{m^2}$
$c_{top}$	Dashpot coefficient for sloshing damper	$1.209 \cdot 10^4$	$\frac{Ns}{m}$
$c_w$	Distributed dashpot coefficient for hydrodynamic damping	$9.291 \cdot 10^4$	$\frac{Ns}{m^2}$
$k_{bl}$	Spring stiffness coefficient of the blades	$1.780 \cdot 10^6$	$\frac{N}{m}$
$k_s$	Distributed spring stiffness coefficient of the soil	$1.924 \cdot 10^8$	$\frac{N}{m^2}$
$k_t$	Spring stiffness coefficient at the pile tip	$2.216 \cdot 10^9$	$\frac{N}{m}$



## Finding the sign of terms in the Equation of Motion

Here we initially presume that the sign of the mass moment of inertia term ( $M = +J \frac{\partial^3 w}{\partial t^2 \partial x}$ ) of the top mass in the boundary condition of the model (eq. 4.12) on the right side of the equal sign is positive, then the following relation around  $x=L$  where the top mass is situated must hold:

$$EI \int_{L-\varepsilon}^{L+\varepsilon} W''''(x-L) dx = \int_{L-\varepsilon}^{L+\varepsilon} M \delta'(x-L)(x-L) dx = 0 \quad (I.0)$$

where  $\varepsilon \ll 1$ , and the EOM is multiplied by  $(x-L)$ .

First working out the integral on the left hand side with the use of integration by parts ( $\int u dv = uv - \int dv u$  and  $u = (x-L)$ ,  $du = dx$ ,  $dv = W'''' dx$  and  $v = W''''$ ):

$$\int_{L-\varepsilon}^{L+\varepsilon} W''''(x-L) dx = W''''(x-L)|_{L-\varepsilon}^{L+\varepsilon} - \int_{L-\varepsilon}^{L+\varepsilon} W'''' dx = \quad (I.1)$$

$$W''''(L+\varepsilon)(L+\varepsilon-L) - W''''(L-\varepsilon)(L-\varepsilon-L) - W''''|_{L-\varepsilon}^{L+\varepsilon} = \quad (I.2)$$
$$-W''''(L) \cdot -\varepsilon - W''''(L+\varepsilon) + W''''(L-\varepsilon) = +W''''(L)$$

---

where  $\varepsilon \rightarrow 0$  is used and the fact that  $L + \varepsilon$  does not exist so terms for this region are equaled to zero. And then the right hand side of the first equation becomes:

$$\int_{L-\varepsilon}^{L+\varepsilon} M\delta'(x-L)(x-L)dx = -M \quad (\text{I.1})$$

where the previously explained derivation rule of the Dirac Delta function is used. Now equaling the left hand side and the right hand side gives us:

$$+W''(L) = -J \frac{\partial^3 w}{\partial t^2 \partial x} \quad (\text{I.1})$$

So this means that the first assumption of the mass moment of inertia having a positive sign on the right hand side of the equal sign is correct: it should be positive if the left hand side term with  $EIW''''$  is also positive.

# Bibliography

- [1] Lecture notes on Sustainable Energy Technology - SET3011. TU-Delft, the Netherlands, 2008.
- [2] J. G. W. Alberts. Identification of a drive-train under aeroelastic loads performed on an offshore and onshore siemens wind turbine operating in closed-loop. Master's thesis, Delft University of Technology, 2010.
- [3] American Petroleum Institute (API). Recommended practice for planning, designing and constructing fixed offshore platforms.
- [4] Windenergie; elektriciteitsproductie capaciteit en windaanbod per maand <http://statline.cbs.nl/StatWeb/publication/> Centraal Bureau voor de Statistiek (CBS), 2011.
- [5] S. Foti C.G. Lai, G.J. Rix and V. Roma. Simultaneous measurement and inversion of surface wave dispersion and attenuation curves. Soil Dynamics and Earthquake Engineering, 22:923–930, 2002.
- [6] M.F. Cook. Damping estimation, response prediction and fatigue calculation of an operational single pile platform. Master's thesis, Massachusetts Institute of Technology and Woods Hole Oceanographic Institution, 1982.
- [7] Global Wind Energy Council. Global Wind Energy Outlook 2010. October 2010.
- [8] D. den Dekker. Efficient modeling of rotational effects for wind turbine structural dynamic analysis. Master's thesis, Delft University of Technology, 2010.
- [9] G. Gazetas & R. Dobry. Horizontal response of piles in layered soils. Journal of Geotechnical Engineering, 110:No. 1, 1984.

- [10] Al-Hundaidi et al. Shear moduli and damping in frozen and unfrozen clay by resonant column test. Canadian Geotechnical Journal, 33 (3):510–514, 1996.
- [11] N.J. Tarp-Johanson et al. Comparing sources of damping of cross-wind motion. DONG Energy.
- [12] Energy efficiency for the 2020 goal  
[http://europa.eu/legislation\\_summaries/energy/energy\\_efficiency](http://europa.eu/legislation_summaries/energy/energy_efficiency)  
EU Legislation, 2009.
- [13] European Wind Energy Association (EWEA). Wind Energy - The Facts. 2009.
- [14] J.A. Battjes G.L. Kuiper, A.V. Metrikine. A new time-domain drag description and its influence on the dynamic behaviour of a cantilever pipe conveying fluid. Journal of Fluids and Structures, 23:429445, 2007.
- [15] P. Godroy. Integrated design methodology for a monopile support structure for offshore wind turbines. Master's thesis, Offshore Engineering, Delft University of Technology, 2010.
- [16] K.F. Graff. Wave motion in elastic solids. Oxford University Press, 1975.
- [17] R. Haghi. Integrated design and optimization of an offshore wind turbine monopile support structure. Master's thesis, Technical University of Delft, April 2011.
- [18] M. Novak & L. EL. Hifnawy. Effect of soil-structure interaction on damping of structures. Earthquake Engineering and Structural Dynamics, 11:595–621, 1983.
- [19] J.S. Hoving. The relationship between continuous and lattice properties. Unpublished document.
- [20] Europe's Energy Portal  
<http://www.energy.eu>, 2010.
- [21] International Energy Association (IEA). World Energy Outlook. 2009.
- [22] L. Karl. Dynamic Soil Properties out of SCPT and Bender Element Tests with Emphasis on Material Damping. PhD thesis, Ghent University Faculty of Engineering, Department of Civil Engineering, Laboratory of Soil Mechanics, 2005.

- 
- [23] D.S. Kim and J.S. Lee. Source and attenuation characteristics of various ground vibrations. Geotechnical Special Publication, (2):1507–1517, 1998.
- [24] C. Kleipool. Optimization of the transport- & installation process of offshore wind farms. Master’s thesis, Delft University of Technology, 2008.
- [25] G. Degrande L. Karl, W. Haegeman. Determination of the material damping ratio and the shear wave velocity with the seismic cone penetration test. Soil Dynamics and Earthquake Engineering, 26:1111–1126, 2006.
- [26] D. Badoni & N. Makris. Nonlinear response of single piles under lateral inertial and seismic loads. Soil Dynamics and Earthquake Engineering, 15:29–43, 1996.
- [27] A.V. Metrikine. Lecture Notes on Structural Dynamics - CT4140. Delft University of Technology, Faculty of Civil Engineering, the Netherlands, 2008.
- [28] T.Nogami M.Novak and F. Aboul-Ella. Dynamic soil reactions for plane strain case. Journal of the Engineering Mechanics Division, 104:953–959, 1978.
- [29] D.-P. Molenaar. Cost-effective Design and Operation of Variable Speed Wind Turbines - Closing the gap between the control engineering and the wind engineering community. PhD thesis, Delft University of Technology, 2003.
- [30] B. J. Pedersen. Note on the determination of the aeroelastic damping in the 1st tower/pile mode of the swt 3.6 mw test turbine, bowf gb at standstill. LAC engineering, 2009.
- [31] L.M. Pires. Closed-loop system identification for model-based control design. Master’s thesis, Delft University of Technology, 2008.
- [32] W. Musial & B. Ram. Large-scale offshore wind power in the united states - assessment of oppertunities and barriers. Technical report, National Renewable Energy Laboratory, 2010.
- [33] C.B. Smith and N.M. Wereley. Transient analysis for damping identification in rotating composite beams with integral damping layers. Smart Materials and Structures, 5:540–550, 1996.

- 
- [34] C. Torres Stoeckl. Dynamic load reduction of a wind turbine drive-train through robust control. Master's thesis, System & Control, Delft University of Technology, 2011.
  - [35] C. M. van den Berg. Development of a resource optimization tool for operation and maintenance of offshore wind farms. Master's thesis, Delft University of Technology, 2011.
  - [36] P.L.C. van der Valk. Model reduction & interface modeling in dynamic substructuring. Master's thesis, Delft University of Technology, 2010.
  - [37] M.F. Cook & J.K. Vandiver. Measured and predicted dynamic response of a single pile platform to random wave excitation. pages 637–643. Offshore Technology Conference Houston, Texas, May 1982.
  - [38] S.N. Voormeeren. Coupling procedure improvement & uncertainty quantification in experimental dynamic substructuring. Master's thesis, Delft University of Technology, 2007.
  - [39] P. Wegener. A critical evaluation of the current design standard for offshore wind turbine monopile foundations. Master's thesis, Offshore Engineering, Delft University of Technology, 2010.



